ASTON UNIVERSITY

Brain Ictal State Characterisation through Multimodal Information Integration

THOMAS ANTOINE RAYMOND BERMUDEZ

A thesis submitted for the degree of Doctor Of Philosophy, 2009

Thesis Summary

This Thesis addresses the problem of automated false-positive free detection of epileptic events by the fusion of information extracted from simultaneously recorded electroencephalographic (EEG) and electrocardiographic (ECG) time-series. The approach relies on a biomedical case for the coupling of the Brain and Heart systems through the central autonomic network during temporal lobe epileptic events: neurovegetative manifestations associated with temporal lobe epileptic events consist of alterations to the cardiac rhythm. From a neurophysiological perspective, epileptic episodes are characterised by a loss of complexity of the state of the brain. The description of arrhythmias, from a probabilistic perspective, observed during temporal lobe epileptic events and the description of the complexity of the state of the brain, from an information theory perspective, are integrated in a fusion-of-information framework towards temporal lobe epileptic seizure detection.

The main contributions of the Thesis include the introduction of a biomedical case for the coupling of the Brain and Heart systems during temporal lobe epileptic seizures, partially reported in the clinical literature; the investigation of measures for the characterisation of ictal events from the EEG time series towards their integration in a fusion-of-knowledge framework; the probabilistic description of arrhythmias observed during temporal lobe epileptic events towards their integration in a fusion-of-knowledge framework; and the investigation of the different levels of the fusion-of-information architecture at which to perform the combination of information extracted from the EEG and ECG time-series.

The performance of the method designed in the Thesis for the false-positive free automated detection of epileptic events achieved a false-positives rate of zero on the dataset of long-term recordings used in the Thesis.

Keywords: Temporal lobe epilepsy, fusion-of-information.

Contents

List of Figures

List of Tables

Acknowledgements

I would like to express my gratitude to my supervisor Professor David Lowe for his guidance, encouragement and support. I would not have been able to complete the work in this Thesis if not for him. I feel short of words but I would like to thank you for your time and your patience; and for giving me an opportunity to work with you.

I would like to express my gratitude to Vicky Bond for her help and support and for succeeding in making everything run smoothly in the Neural Computing Research Group. Thank you for sharing your love for Art Nouveau during the Art Nouveau poster exhibition.

I would like to express my gratitude to Doctor Anne-Marie Arlaud-Lamborelle from Centre hospitalier Henri Duffaut, Avignon (France), for her guidance and support and for unlocking the idea at the core of the Thesis.

I would like to thank the staff at the Neural Computing Research Group, particularly Professors Ian Nabney and David Saad, Doctor Dan Conford, and Alex Brulo. I would like to take this opportunity to thank Biopattern for giving me the chance to share and to disseminate my work among Biopattern partners across Europe.

I would like to thank my research fellows, particularly: Mingmanas Sivaraska, Rajeswari Matam, Erik Casagrande, Jack Raymond, Michel Randrianandrasana, Rémi Barillec, Borémi Toch and Delfine Dussy, Stéphane and Chantal Bounkong.

I would finally like to thank my family and friends: my parents Joëlle and José and my grand-parents Incarnación and Antoine, Violette and Raymond, for their unconditional love and support; my friends Thomas Boniface, Manon Batiat, Claire "WW" Chavouet, Julien Michel and Joo Bee Yeow for their friendship, support and patience all these years, silently listening to my constant moaning; and the "guys". The past six years in Aston University have seen me change from late teen to not-quite-there-yet-adult and I would not have been able to successfully perform this transition if not for them.

1 Introduction

CONTENTS

According to the World Health Organization (WHO), the mean prevalence of active epilepsy is estimated to be approximately 8.2 per 1000 of the general population. At any one time it is estimated that around 50 million people in the world have epilepsy. The lifetime prevalence of epilepsy (i.e. the number of people in the world who have had epilepsy, have epilepsy or will have epilepsy) is double the latter estimate.

A variety of applications have been derived from electroencephalogram (EEG) analysis with different levels of success over the past decades: from the detection of epileptic events to their prediction. EEG analysis aims at supporting and extending the electroencephalographer's capabilities with objective data in numerical or graphical form to characterise EEG phenomena such as spikes, sharp waves and abnormal patterns. EEG analysis methods extract (feature extraction), measure (quantification) and classify EEG patterns to mimic the *modus operandi* of the electroencephalographer. By reproducing the *modus operandi* of electroencephalographers instead of reproducing the *modus operandi* of neurophysiologists (who might be able to interpret EEG recordings), engineers consider epilepsy as a condition limited to the Brain. However epilepsy is a condition primarily affecting the Brain but also affecting the systems afferent to the Brain via the central autonomic network such as the cardiac- and respiratory systems. The novelty of this Thesis is to consider epilepsy as a global condition affecting the central neural network and its afferent systems: a biomedical case for the coupling of the Brain- and Heart systems during temporal lobe epileptic seizures is the basis of the design of a fusion-of-information framework towards the automated false-positives free detection of temporal lobe epileptic events described in the Thesis. In this perspective, the epilepsy is not only observed through its clinical and EEG signs but also through the monitoring of autonomic cardiac functions affected by epileptic events.

1.1 EEG analysis

EEG analysis methods have been developed not only to emulate electroencephalographers' capabilities (quantification, extraction and classification of EEG phenomena inferred from the observation of the amplitude, frequency, morphology and spatial distribution of brain waves) but also to extend them by, for example, performing the quantitative analysis of long duration recordings, difficult to achieve by clinicians (Lopes da Silva, 1993). Since no biological or mathematical model has been able to fully explain the

diversity of EEG patterns, the interpretation of EEGs remains phenomenological. Hence EEG inspection has been the preferred method to interpret EEG recordings. EEG analysis methods have been introduced to support visual inspection (i.e. extend electroencephalographers capabilities) by extracting relevant information, with respect to the purpose of the analysis, encompassed in EEG recordings. The methods rely on the characteristics of EEG recordings such as their high temporal resolution, poor spatial resolution and quasi-stationary property on short time scales (usually ten to twenty seconds).

Classical basic categories for EEG analysis methods are time- and frequency-domain analysis, non-linear dynamics and embedding, intelligent systems. Time- and frequency-domain analysis methods are closely related as they describe the same phenomenon: they rely on the statistical analysis of EEG events of interest and the computation of characteristics of the data either in the time-domain or once the signal has been decomposed into different frequencies. This classical decomposition of EEG analysis approaches in time and frequency-domain methods is sometimes opposed to the decomposition into parametric and non-parametric methods (Lopes da Silva, 1993). The distinction into parametric and non-parametric methods relies on two different approaches to EEG analysis. Non-parametric methods consider the statistical properties of EEG signals as a realisation of random processes, without a specific generation model. The signal is hence characterised by its distribution and moments (e.g. test of the Gaussianity of the EEG amplitude distributions), by the autocorrelation function or the power spectrum (e.g. describing the EEG signal in terms of frequency, Fourier analysis), or by distributions of intervals between level crossings (e.g. distribution of zero-crossings of the original EEG). On the other hand parametric methods for EEG analysis are used when models of the biophysical processes underlying the generation of EEG phenomena (such as alpha rhythm, spike and wave complex...) are available. EEG signals are then described in terms of a mathematical model characterised by a set of parameters (e.g. the EEG signal is assumed to be generated by a statistical model with time-varying parameters). Non-linear dynamics and embedding approaches rely on Takens' theorem (Takens, 1981). They have been applied to biomedical time series to characterise the behaviour in the phase space of systems too complex to be modelled (Litt & Echauz, 2002). Intelligent systems, such as neural networks, are trained to discriminate between different epochs of the EEG signal (e.g. pathological versus non-pathological epochs) (Litt & Echauz, 2002).

The choice of an appropriate EEG analysis method is application-oriented. The au-

tomated seizure detection of epileptic events from long-term monitoring EEG recordings aims at the accurate detection of epileptic events without the supervision of an electroencephalographer. Highly-specific EEG analysis methods manage to attain high sensitivities to epileptic events (e.g. methods performing wavelet-decomposition, feature extraction and segmentation on 2s of data achieve a sensitivity of the order of 76%, (Saab & Gotman, 2005)) desired in biomedical applications but they usually induce false-positives. In the framework of the automated detection of epileptic events, false-positives might have undesirable consequences for the patient. The design of methods for the automated detection of epileptic events should take into consideration not only the sensitivity of the methods to epileptic events but also the number of false-positives induced by the achievement of a high sensitivity. Saab and Gotman (Saab & Gotman, 2005) accurately summarised other challenges to overcome in the design of a system to detect epileptic events from surface EEG recordings: the design of a method to detect epileptic events can be compared to the design of a pattern recognition algorithm for which no standard pre-defined pattern is available due to the multiplicity of manifestations taken by epileptic events in EEG recordings for a given patient and from patient to patient. Further requirements for seizure detections methods are (Gotman *et al.*, 1997b,a): two data sets (one for training the method and another one for testing the method), large sample sizes, no pre-selection of the data with respect to typicality or quality, data from a number of sources so that the methods are not tailored to features of a single population. A further requirement (Saab & Gotman, 2005) is for the sensitivity rate to be of the order of 70-90% and the false-positive rate to range from 0.3 to 3 detections per hour. One of the aims of the Thesis is to investigate methods to reduce the incidence of undesired false-positives on, e.g., the patient and the clinician, by reducing their rate to zero: the Thesis is the first attempt to the automated false positives-free detection of epileptic events by the fusion of information extracted from simultaneously recorded electroencephalographic- and electrocardiographic time-series.

The next Section of the Thesis introduces a biomedical case for the coupling of the Brain- and Heart systems during temporal lobe epileptic seizures. The clinical-, EEG- and neurovegetative manifestations of temporal lobe epileptic seizures allow for the design of a method for the automated detection of epileptic events by the fusion of multivariate information in a fusion-of-knowledge framework. Such a method allows for the use of a generic EEG analysis method (as opposed to a highly specific one) whose diagnosis is

complemented by another physiological source of information.

1.2 Biomedical case for the coupling of the Brain- and Heart systems during temporal lobe epilepsy

"Temporal lobe epilepsy" (TLE) was a term introduced in 1951 by Jasper et al. (Jasper *et al.*, 1951) to characterise seizures arising from the temporal lobe. Temporal lobe epileptic seizures are closely related to psychomotor (also called "complex partial") seizures. Nevertheless not all seizures originating from the temporal lobe are complex partial seizures; psychomotor seizures may originate from the vicinity of the temporal lobe. Complex partial seizure manifestations comprise clinical ictal manifestations such as automatisms, autonomic and sensory symptoms. Vasomotor, cardiovascular, respiratory, urogenital and other autonomic ictal dysfunctions during psychomotor seizures have been documented. Autonomic (or "vegetative") visceral ictal symptoms are frequently observed. Broglin et al. (Broglin & Bancaud, 1991) produced an extensive report on ictal neurovegetative manifestations induced by temporal lobe epileptic seizures, and described their visceromotor and viscerosensitive manifestations.

Baumgartner et al. (Baumgartner *et al.*, 2001) compiled a short review on autonomic symptoms during epileptic seizures, listed into cardiovascular changes, respiratory manifestations, gastrointestinal symptoms, cutaneous manifestations, pupillary symptoms and genital and sexual manifestations. The manifestations of the activation of the central autonomic network provide clinical information on the localisation and lateralisation of the seizure onset zone. Reeves (Reeves, 1997) focuses the analysis of the disruption of the autonomic activity during epileptic seizures on the cardiovascular and respiratory perturbations (heart arrhythmias and irregular breathing patterns). Due to their severity the latter could overshadow the diagnosis of epilepsy. In a similar fashion Devinsky et al. (Devinsky *et al.*, 1986) stress through six case reports the misdiagnosed, treatable cardiovascular perturbations induced by complex partial seizures. In a latter paper Devinsky (Devinsky, 2004) lists the modifications induced by seizures on autonomic and cardiovascular functions and describes the effects of epilepsy therapy on autonomic function: antiepileptic drugs and temporal lobe epilepsy surgery may help stabilise cardiovascular control in epilepsy patients. Galimberti et al. (Galimberti *et al.*, 1996) concluded from

a study of 100 partial epileptic seizures recorded by ambulatory EEG-ECG in fifty out-patients that an early heart rate decrease (assessed from the first ten-seconds period of ictal EEG discharge) is more probable in temporal lobe seizures than in seizures of other origin.

The cardiovascular autonomic symptoms induced by temporal lobe epilepsy seizures mainly consist of tachycardia often with an increase of the blood pressure; occasionally they consist of bradycardia, dramatic decrease of the blood pressure; and irregular pulse. Blumhardt et al. (Blumhardt *et al.*, 1986) referenced the electrocardiographic accompaniments of seventy-four spontaneous temporal lobe epileptic seizures from twenty-six patients. In 92% of the patients the seizures were associated with an increased heart rate (tachycardia). Constantin et al. (Constantin *et al.*, 1990) report five cases of patients with temporal lobe epilepsy in whom sinus bradyarrhythmias and syncope were prominent manifestations of seizure activity. Reeves et al. (Reeves *et al.*, 1996) review twenty-three cases of the ictal bradycardia syndrome. Twenty of the twenty-three patients (87%) whose site of ictal onset could be localised had temporal lobe epilepsy.

Figures 1.1 and 1.2 show the ECG recording during an interictal- and an ictal (temporal lobe epilepsy) event, respectively. During the interictal epoch the cardiac rhythm is about 90 beats per minute while during the ictal event the cardiac rhythm is about 130 beats per minute, corresponding to tachycardia.

The biomedical case for the coupling of the Brain- and Heart systems during temporal lobe epileptic seizures is not the only coupling of this nature: changes in the heart- and respiration rates in neonates during epileptic seizures have been documented (Greene *et al.*, 2006). The observation of a decrease of the order of 5.70% in the mean R-R interval (time interval between consecutively detected R-peaks) during epileptic seizures led to the design of an electrocardiogram-based method for neonatal seizure detection (Greene *et al.*, 2007b). The method classifies one minute-epochs as either "seizure" or "non-seizure" by performing the linear discrimination of 41 heartbeat timing interval features. Greene et al. report a sensitivity of the patient-independent classifier of the order of 78.4% and a specificity (percentage of non-seizure epochs correctly classified) of the order of 51.6% (which gives a false detection rate of 48.4%). In clinical practice the false detection rate (percentage of non-seizure epochs classified as seizure epochs) reported is highly unacceptable.

Kerem et al. (Kerem & Geva, 2005) designed a method for the prediction of epileptic

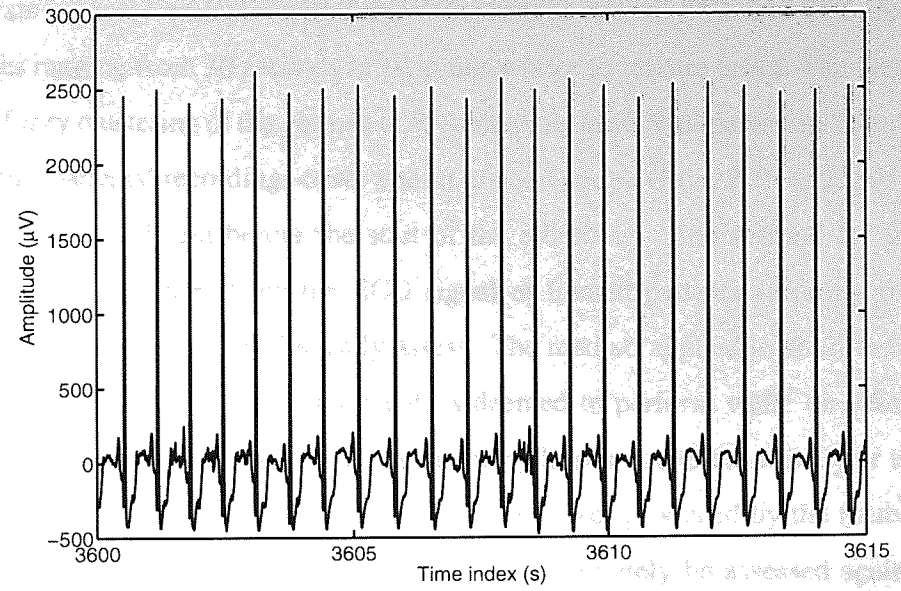

Figure 1.1: ECG recording during an interictal epoch: no epileptic event is recorded on the simultaneously recorded EEG (shown in Figure 2.1). The cardiac rhythm is about 90 beats per minute.

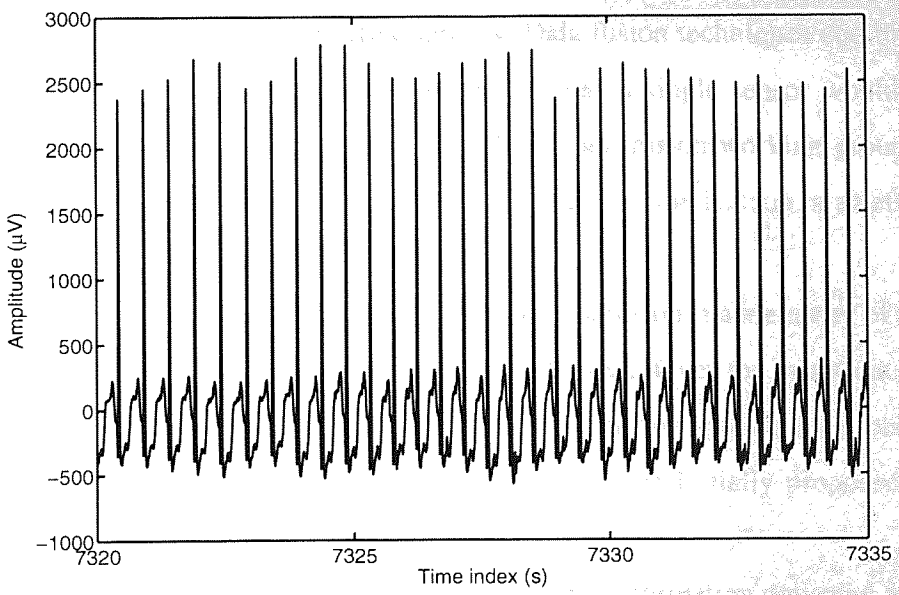

Figure 1.2: ECG recording during an ictal event (temporal lobe epilepsy): the epileptic event starts on the simultaneously recorded EEG (shown in Figure 2.2) at $t = 7330$s. The cardiac rhythm is about 130 beats per minute, corresponding to tachycardia.

seizures from the ECG signal of human patients suffering from temporal lobe epilepsy and of rats rendered epileptic with forecasting sensitivities of 86% and 81%, respectively, at times ranging from 30 seconds to 10 minutes prior to seizure onset. The method relies on the fuzzy clustering of the periods of R-R intervals in an N-dimensional feature space. The human patients' recordings cover a short preictal period (from 590s to 2330s): the preictal activity could begin before the start of the recording. The method for the prediction of epileptic seizures from the ECG signal of human patients suffering from temporal epilepsy is difficult to realistically assess. The method applied to short-term recordings, centered around a unique ictal event, is deemed to perform well: on short time scales the ECG signal is not corrupted by heart arrhythmias due to the activity or to a condition of the patient reducing the number of false-positives produced by the method to zero in all but one case. The method would more appropriately be assessed against long-term recordings.

1.3 Biomedical data fusion

In the 1980s the motivation behind the investigation of multisensor data fusion techniques was the development of military applications such as target tracking, automated identification of targets by non-cooperative sensors. Data fusion techniques combine data from multiple sensors to achieve "better" inferences than a single sensor would achieve. In 1986 the Joint Directors of Laboratories (JDL) data fusion working group proposed a process model for data fusion (Figure 1.3) and a data fusion lexicon in an effort to codify data fusion terminology (Hall & Llinas, 2001).

The backbone of the JDL process model for data fusion is a hierarchy of subprocesses during which the information fusion can be achieved. Over the years the JDL process model for data fusion has been revised and new process models have been proposed, usually built around the intuitive hierarchical backbone initially proposed by the JDL process model (Steinberg & Bowman, 2001).

In a medical environment practitioners combine information collected from different sources to form a diagnosis. Likewise biomedical data fusion combines data originating from multiple sources to improve a decision task such as classification (e.g. "healthy patient"/"non-healthy patient"), prediction (e.g "patient likely to be affected by Alzheimer disease") or estimation (e.g. "stage of the disease"). Despite the various levels of the fu-

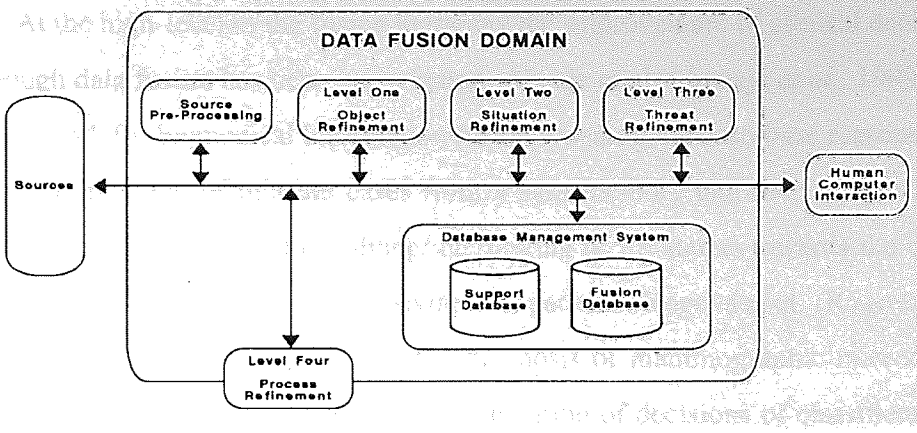

Figure 1.3: Joint Directors of Laboratories (JDL) process model for data fusion (from (Hall & Llinas, 2001)).

sion hierarchy at which to perform biomedical data fusion, it has mainly been performed at the low-level of sensors/observations (in order to exploit the superresolution capability of fused observations in a multisensor environment: the finer resolution of a sensor is used to complete the properties of another one) or at the high-level of decisions (in order to obtain a binary decision). The biomedical data fusion of non-EEG data is mainly concerned with image or sensor registration (low-level of the fusion hierarchy); or decision making (high-level of the decision hierarchy); whereas the biomedical data fusion of EEG data emphasis is on the EEG inverse problem and on the detection of epileptic seizure events.

1.3.1 Biomedical data fusion for image registration

Image registration has been performed in different ways depending on the decision task considered and on the sources of information available. For example a sequence of MRI medical images, treated as though multiple sensors had generated the sequence, have been combined to improve the performance of the detection of 3-D deformations of the scoliosis (Taleb-Ahmed & Gautier, 2002). Solaiman et al. (Solaiman *et al.*, 1999) augmented the information provided by a monosensor echo-endoscopic system with multisources of knowledge (i.e. a new set of information data obtained by application of a priori knowledge) towards oesophagus inner-wall detection. Sensor registration motivates the data fusion at the low-level of the fusion hierarchy: Hernandez et al. (Hernández *et al.*, 1999) investigated multisensor and multisource data fusion schemes to improve atrial and ven-

tricular activity detection in critical care environments.

At the high-level of the fusion hierarchy the improvement of clinical decision support through data fusion has been investigated. Azuaje et al. (Azuaje *et al.*, 1999) proposed a framework for biomedical information fusion based on the case-base reasoning paradigm (i.e. the retrieval of relevant cases from a case memory and their adaptation to a new problem or situation for the solving/interpreting of the latter) towards the estimation of the coronary heart disease risk of asymptotic patients. Rogova et al. (Rogova & Stomper, 2002) proposed a decision aid for the diagnosis of mammographic microcalcifications as benign or malignant based on the combination of decisions of classifiers working on different sources of information (image- and knowledge-based).

1.3.2 Biomedical data fusion and the inverse problem

The inverse problem in electroencephalography/magnetoencephalography (MEG) consists in finding the locations and strengths of the neuronal currents from discrete samples of the potentials recorded at the surface of the volume conductor (the head) from twenty to one hundred and twenty-eight locations. The bioelectric sources (EEG inverse problem) are modelled as current dipoles (Nunez & Srinivasan, 2006) described by three spatial parameters, two angular parameters and one moment parameter. The inverse problem, due to the small number of data samples available with respect to the large number of parameters to be estimated, is ill-defined: the scalp electric field does not allow for an unequivocal estimation of the associated current generators. However the spatial accuracy of the EEG/MEG inverse problem can be improved by the introduction of spatial priors to constrain the solution space assuming the bioelectric and metabolic activities are coupled. Part of the brain metabolic activity can be inferred from functional magnetic resonance imaging (fMRI) through the blood oxygenation level dependent (BOLD) response. EEG-EMG/fMRI fusion approaches have been based on this assumption. Babiloni et al. (Babiloni *et al.*, 2004) modelled the human cortical activity by combining high-resolution EEG, MEG and fMRI. The relevance of this work to the Thesis is that there is a strong biophysical reason which motivates the use of data fusion. Specifically, neural activity generating EEG potentials and MEG fields increases glucose and oxygen demands, leading to an increase of the hemodynamic response that can be measured by the fMRI. The correlation between electrical and hemodynamic concomitants provides

the basis for a spatial correspondance between fMRI responses and EEG/MEG source activity. Hence the determination of the priors in the resolution of the linear inverse problem was performed with the use of information from the hemodynamic responses of the cortical areas as revealed by block-designed fMRI.

Sharon et al. (Sharon *et al.*, 2007) assessed the localising ability of neuronal dynamics within well-defined brain regions using separate and combined MEG and EEG modalities compared to the functional MRI localisation during early visual responses to focal Gabor patches flashed during subject fixation experiments. Using three different source estimation approaches, the authors found that the localisation accuracy of the combined MEG and EEG solution outperformed that of either modality alone.

Gotman et al. (Gotman *et al.*, 2006) reviewed the methodology involved in combining EEG and functional MRI time series to uncover the regions of the brain showing changes in the BOLD signal in response to epileptic spikes observed from the EEG. These regions are presumably involved in the abnormal neuronal activity at the origin of epileptic discharges. The integration of these data is not straightforward: the high temporal resolution of EEG is balanced by its poor spatial resolution (i.e. uncertainty in source localisation) due to errors in head models and the ill-defined nature of the inverse problem; the high spatial resolution of fMRI is balanced by its poor temporal resolution and the partial understanding of its link to neural activity. Integration of EEG and fMRI data can be achieved by considering the spatial and temporal links between the two modalities.

Considering event-related (ER) EEG and fMRI as different measures of the neuronal activity Daunizeau et al. (Daunizeau *et al.*, 2007) proposed a symmetrical multimodal EEG/fMRI information fusion approach designed to identify event-related bioelectric and hemodynamic responses. The decomposition of the neuronal activity into the common substrate that contributes to EEG and fMRI measurements and into subspaces of neuronal activity detected only by one type of measurement that do not contribute to the other type of measurement formalises the apparent coupling/uncoupling process occuring between bioelectric and hemodynamic ER responses. The common substrate of bioelectric and hemodynamic activities is defined as the spatial support of the EEG/fMRI common signal generators. Hence the hierarchical EEG/fMRI generative model proposed accounts for the separation of spatial and temporal characteristics of the brain. The common EEG/fMRI sources were inferred from a joint EEG/fMRI dataset using a devoted variational Bayesian learning scheme.

In a previous paper (Daunizeau *et al.*, 2005), Daunizeau et al. had raised some concern about the use of a priori spatial information derived from functional modalities such as fMRI in the EEG/MEG inverse problem due to the partial knowledge of the bioelectric/metabolic coupling. They proposed an approach to quantify the adequacy of the fMRI-derived prior to the data compared to the one obtained from using a noninformative prior in a Bayesian framework.

The works detailed above are examples of electromagnetic field integration towards enhanced spatial localisation of the generators of the brain. The aim of the Thesis is to propose a biomedical data fusion framework towards enhanced epileptic seizure detection from ECG and EEG time series.

1.3.3 Biomedical data fusion for epileptic seizures detection

To the author's best knowledge, the only previous attempt to biomedical data fusion towards epileptic seizure detection is the very recent data fusion of EEG and ECG time series proposed by Greene et al. (Greene *et al.*, 2007a) for neonatal seizure detection. Following the initial constatation that heart- and respiration rates were altered in neonates during epileptic seizures and a first attempt to the neonatal seizure detection from electrocardiogram recordings, Greene et al. proposed a novel algorithm for neonatal seizure detection from the combination of an ECG-based classifier with a multi-channel EEG-based classifier (Greene *et al.*, 2007a). For a patient-independent system Greene et al. achieved a sensitivity of the order of 81.44% for a false detection rate of 28.57%. The features extracted from the ECG time series were based on R-R intervals for 60 second-epochs of ECG: mean R-R interval, standard deviation of R-R intervals, spectral properties of R-R intervals. Features (spectral features such as power ratio, dominant spectral peak) were extracted for each channel of EEG, sorted and concatenated before being combined with the features extracted from the ECG time series by simple aggregation or weighting and being fed into a pattern classifier. This is the most similar published work that exists, to this Thesis.

1.4 Biopattern and bioprofiles

The Biopattern[1] Network of Excellence (NoE) was a project (running from January 2004 to December 2007) that integrated key elements of European research to enable Europe to become a world leader in eHealth. The Grand Vision was to develop a pan-European, coherent and intelligent analysis of a citizen's bioprofile (i.e. the personal "fingerprint" that fuses together a person's past and current medical history, biopatterns and prognoses; and combines data, analysis and predications of susceptibility to diseases); to make the analysis of this bioprofile remotely accessible to patients and clinicians; and to exploit bioprofile to combat major diseases such as cancer and brain diseases.

A biopattern is the basic information (or pattern) that provides clues about underlying clinical evidence for diagnosis and treatment of diseases. It is derived from specific data types: genomics information or biosignals such as the EEG. Examples of biopatterns and of their integration in a bioprofile include features extracted from the EEG time series of patients towards the characterisation of Alzheimer's disease (Zhao *et al.*, 2007; Goh *et al.*, 2005) or microarrays for brain cancer classification (Kounelakis *et al.*, 2005). Features extracted from the EEG time series towards the detection, characterisation and prediction of epileptic events have been investigated, by Biopattern NoE partners gathered in the Brain Task Force, as possible biopatterns to be included in a patient's bioprofile.

The dataset of Medial Temporal Lobe Epilepsy patients used in the Thesis (described in Appendix A.1) was disseminated to Biopattern partners by collaborators from the BIOMED team and from the department of Clinical and Experimental Neurology, both at Katholieke Universiteit Leuven (KUL).

1.5 Thesis aims and objectives

As detailed above, the main aim of the Thesis is to perform a characterisation of the Brain ictal state through multimodal information integration. To attain this aim the main objectives of the Thesis are:

1. **To present a biomedical case for the coupling of Brain and Heart systems during temporal lobe epileptic seizures:** The principles of generation of heart arrhythmias during temporal lobe epileptic seizures are investigated. The clinical literature

[1] www.biopattern.org

reports the coupling of the Brain- and Heart systems during temporal lobe epileptic seizures as heart arrhythmias (bradycardia and tachycardia) developing during ictal events. The biomedical case motivates the design of a method for the false positives-free automated detection of temporal lobe epileptic events.

2. **To investigate measures for the characterisation of ictal events from the EEG time series:** Ictal events are characterised by a loss of complexity of the state of the brain, reported to be successfully monitored by nonlinear measures (such as the correlation sum) or measures of information (such as the Shannon entropy). However such measures are either impractical in a clinical context or subject to caution: the computation of the correlation sum is intensive and its interpretation is highly subjective. The suitability of the Kullback-Leibler divergence for the characterisation of ictal events and its practical implementation in the context of a fusion-of-knowledge framework are demonstrated in this Thesis in Chapter 4.

3. **To propose a method for the description of arrhythmias observed during temporal lobe epileptic events from a probabilistic analysis perspective:** A method for the description of heart rate variability is introduced and tested on real patient data towards its integration in a fusion-of-information framework.

4. **To propose an architecture for the fusion of information extracted from the EEG and ECG time series towards the automated detection of temporal lobe epileptic events in a probabilistic framework:** The description of arrhythmias, from a probabilistic perspective, observed during temporal lobe epileptic events and the description of the complexity of the state of the brain, from an information theory perspective, are integrated in a fusion-of-information framework towards temporal lobe epileptic seizure detection. Different fusion architectures (from low- to high levels of fusion) are proposed, considering the trade-off between optimal data conservation and practical implementation. The architectures are tested on real patient data towards the automated false positives-free detection of epileptic events by the fusion of information extracted from simultaneously recorded electroencephalographic- and electrocardiographic time-series.

1.6 Outline of the Thesis

The Thesis is divided into five Chapters. A summary of each Chapter is presented below.

Chapter 2: Complexity characterisation of human EEG time series. The focus of the Chapter is on the extraction of information from the EEG time series for the detection of epileptic events, in a fusion of information framework. The basic mechanisms involved in human epilepsy are described and motivate the measures extracted from the EEG time series to estimate the changes observed in the complexity of the state of the brain during epileptic events, their suitability to the novel approach of this Thesis is assessed against their practical integration in a fusion of knowledge framework.

Chapter 3: Characterisation of cardiac arrhythmias during temporal lobe epileptic seizures. The extraction of information from the ECG time series is the object of the Chapter. The brain structures and the mechanisms at the origin of the observation of heart arrhythmias during temporal lobe epileptic events are described and a method for the description of heart rate variability is introduced and tested on real patient data. The data interpretation of the arrhythmias observed during temporal lobe epileptic events is performed from a probabilistic analysis perspective towards its integration in a fusion-of-information framework.

Chapter 4: Information fusion for epileptic event detection. A case for biomedical data fusion motivated the fusion of EEG and ECG time series towards temporal lobe epileptic seizure detection. The levels at which the data fusion can be performed are detailed in the Chapter. The performance of the data fusion approaches are compared to the performance of the unimodal approaches on long-records of patient data.

Chapter 5: Conclusions and directions for future research. A summary of the results obtained concludes the Thesis and directions for future research are discussed.

The Thesis is the work of the author but parts of it have appeared in the public domain including:

- Thomas Bermudez, David Lowe, Anneleen Vergult, Maarten De Vos, Bart Vanrumste, Sabine Van Huffel, Wim Van Paesschen and Anne-Marie Arlaud-Lamborelle.

Preliminary Results on Feature Extraction for Fusion of ECG R-R intervals and EEG Complexity for Epileptic Seizure Detection. *Proceedings of The BIOPATTERN Brain S.I.G Workshop 2006, Gotteborg.*

- Thomas Bermudez, David Lowe and Anne-Marie Arlaud-Lamborelle. Multimodal Model Fusion of EEG/ECG for Epileptic Seizure Detection. *Proceedings of CIMED 2007.*

- Thomas Bermudez, David Lowe and Anne-Marie Arlaud-Lamborelle. Schemes for Fusion of EEG and ECG Towards Temporal Lobe Epilepsy Diagnostics. *Proceedings of the 29th Annual International Conference of the IEEE Engineering in Medicine and Biology Society 2007, Lyon*, pages 5132-5135.

- Thomas Bermudez, David Lowe, Anne-Marie Arlaud-Lamborelle. Improved Temporal Lobe Epileptic Event Detection through Inclusion of Cardiac Fluctuations. *3rd International Workshop on Seizure prediction in Epilepsy 2007, Freiburg.*

- Thomas Bermudez, David Lowe and Anne-Marie Arlaud-Lamborelle. Detecting Brain Malfunction from EEG and ECG. *Natural Computing Applications Forum 2008, Birmingham.*

2 Complexity characterisation of human EEG time series

CONTENTS

A biomedical case for the coupling of the Brain and Heart systems during temporal lobe epileptic seizures, through the central autonomic network, was presented in Chapter 1. The novel approach described in this Thesis relies on the integration of information extracted from multimodal biomedical time series: ECG and EEG. The focus of the Chapter is on the extraction of information from the EEG time series for the detection of epileptic events, in a fusion of information framework. The basic mechanisms involved in human epilepsy (hyperexcitability of regions of the brain, propagation, synchrony and loss of complexity), with a focus at ictal onset, are described in Section 2.1. In this Thesis, the measures extracted from the EEG time series estimate the changes observed in the complexity of the state of the brain, defined from a neurophysiological- and an information theoretical points of view, during epileptic events; their sensitivity to changes caused by epileptic events is demonstrated on artificial and real patient data in Section 2.2. The suitability of the measures of complexity of the state of the brain to the novel approach of this Thesis is assessed against their practical integration in a fusion of knowledge framework (Chapter 4).

2.1 Basic mechanisms of human epilepsy

The characterisation of the ictal state, which is the focus of this Thesis, relies on the identification of the transition from the interictal state to the ictal state: the ictal onset. The interictal state is a period between ictal events during which the factors predisposing the recurrence of spontaneous epileptic seizures (such as congenital malformation or brain injury leading to the reorganisation of brain pathways) are silenced but interictal paroxysmal patterns (such as spikes, sharp waves or the classical spike wave complex (Niedermeyer, 1993)) are observable on the EEG. The ictal onset, whose basic mechanisms are detailed in the next Section, is a transition from the interictal- to the ictal state during which the factors predisposing the recurrence of spontaneous epileptic seizures engage. The seizure occurs and evolves during the ictal state. Readers interested in the basic mechanisms of human epilepsy in the different components of the central nervous system are referred to (Heinemann & Eder, 1997; Ditcher & Wilcox, 1997; Macdonald, 1997; Wasterlain & Mazarati, 1997; Connors, 1997; Schwartzkroin & McIntyre, 1997; Coulter, 1997; Proctor & Gale, 1997; Engel Jr *et al.*, 1997).

2.1.1 Basic mechanisms at the onset of human epilepsy

The ictal onset is the transition state from the interictal- to the ictal state; it comprises the processes leading to the occurrence of spontaneous seizures which vary with the form of epilepsy. Most forms of partial epilepsy, such as temporal lobe epilepsy, involve areas of hyperexcitability of the brain within which neurons undergo synchronous and paroxysmal depolarizations (Dichter, 1997). Under favourable conditions such as the weakening of seizure-blocking mechanisms, the hypersynchronous activity is propagated to both local areas via synaptic pathways, and to distant areas via subcortical and contralateral pathways. When a critical mass of neurons involved in the hypersynchronous activity is reached, seizures result. The link between synchrony and complexity will be established in the next Section.

2.1.2 Complexity as a measure of characterisation of the state of the brain

The brain is organised in neural components functionally segregated at multiple spatial scales (brain areas, neural networks or cortical columns). The sensory systems such as the visual system are segregated in such a manner: neural groups are specialised by visual attributes of perceived objects (shape, colour...). The segregated functionally specialised neural components are activated when presented with a stimulus or when a cognitive task is performed. The information triggered by a stimulus or action is integrated among cooperative neural components according to two mechanisms: convergent connectivity among functionally segregated neural components and reciprocal and parallel connectivity among functionally segregated neural components. The latter mechanism consists of interactions among neural groups generating their short-term synchrony of firing, leading to coherent perception and action.

The concept of complexity is defined with regards to the system whose complexity is measured (i.e. the brain) and with regards to other concepts such as connectivity, information and synchrony: complexity captures functional segregation and integration of information. Connected functionally segregated neural groups showing a synchronous activity (e.g. synchronous firing pattern of neurons) do not exchange statistically novel information: the complexity of the subsystem gets lower as its synchrony gets higher (Elger *et al.*, 2000a,b; Lehnertz & Elger, 1995). The loss of complexity of epileptogenic

areas of the brain is indirectly characterised from the observation of the hypersynchronous activity of such areas, recorded by the EEG time series. The activity of functionally segregated neurons exhibiting a synchronous firing pattern is spatially and timely averaged: the spatially disseminated epileptogenic areas of the brain are successively recruited via the propagation of the recruiting rhythm and the summation of their activities is altered by their propagation to the interface of the electrode.

The relationships between the concepts of complexity of the state of the brain, connectivity, information and synchrony have been described in the paragraph above. The complexity of the brain is a potential tool for the segregation between nominal states of the brain and states of the brain affected by the performance of a cognitive task or altered (on short- and long time scales) by a condition. The next Section is focused on the complexity of the state of the brain during ictal events; it introduces measures to estimate the complexity of the sate of the brain.

Complexity during the ictal state

Epileptic seizures are temporary manifestations of dramatically increased neuronal synchrony (i.e. hypersynchronous activity of the neurons participating in the seizure discharge). The synchronised rhythmic firing pattern of neurons requisitioned in the seizure discharge generates a more ordered ictal EEG signal: the onset of a seizure represents a transition from an interictal epoch to an ictal epoch of increased synchronous activity (Iasemidis & Sackellares, 1996). In the previous Section it was established that neurons showing a hypersynchronous activity did not exchange statistically novel information, leading to a decrease in the complexity of the state of the brain. This observation points to a decreased level of complexity in the neuronal groups involved in the ictal process, observable from the ictal EEG signal.

The seizure termination can be accurately described by a transition from synchronised neuronal activity of low complexity behaviour to an increasingly complex network behaviour reflecting the progressive desynchronisation prior to the seizure termination (Bergey & Franaszczuk, 2001).

Figures 2.1, 2.2 and 2.3 show the electrical activity of the brain as recorded from 21 electrodes disposed on the surface of the skull according to the 10-20 international system during an interictal epoch, at the start of the seizure and further during the seizure. The hypersynchronous activity across all channels of EEG can be observed in Figure 2.3 at

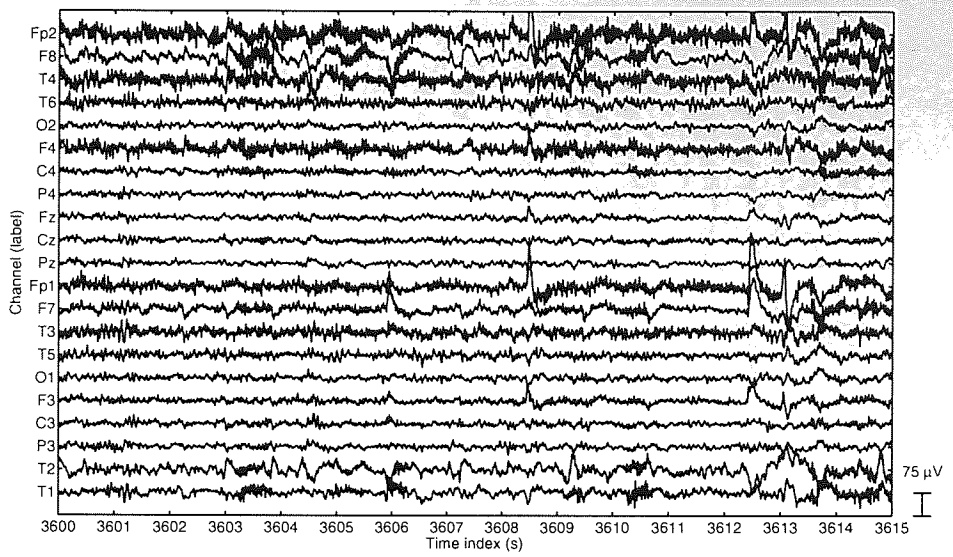

Figure 2.1: EEG recording during an interictal epoch. The electrical activity of the brain recorded at 21 electrodes disposed according to the 10-20 international system at the surface of the skull is weakly correlated. The vertical scale unit is 75μV. No epileptic events are present.

$t = 7342$s.

The observations above confirm the changes in the complexity of the state of the brain during ictal events. The analysis of the changes in the complexity of the states of the brain heavily rely on the definition given to complexity. In this Thesis two definitions of the complexity of the state of the brain are given. In the next Section measures to estimate the transitions between states of the brain towards ictal events and measures to estimate the changes in the complexity of the state of the brain towards ictal events are investigated.

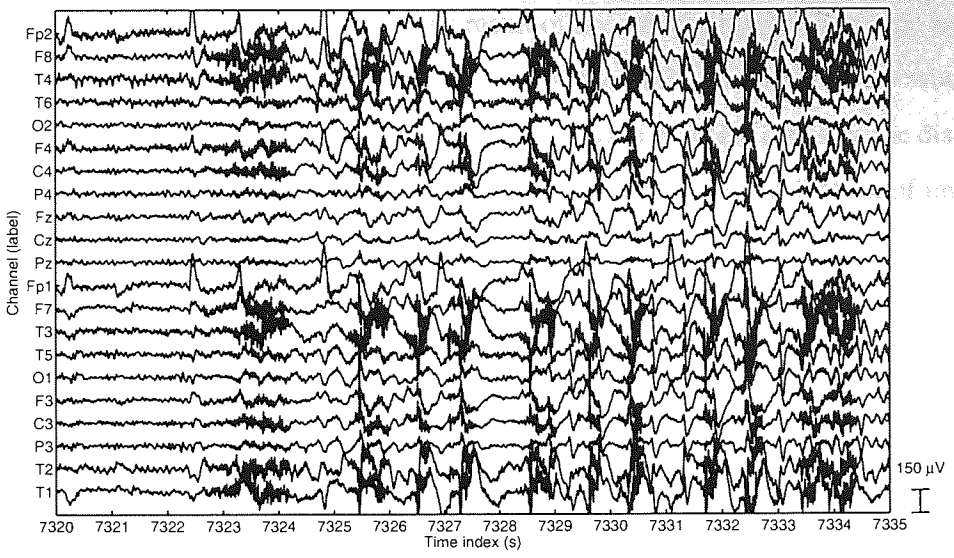

Figure 2.2: EEG recording at the start of an epileptic event. The amplitude of the electrical activity of the brain recorded is dramatically increased (the vertical scale unit is 150μV) when compared to the electrical activity of Figure 2.1.

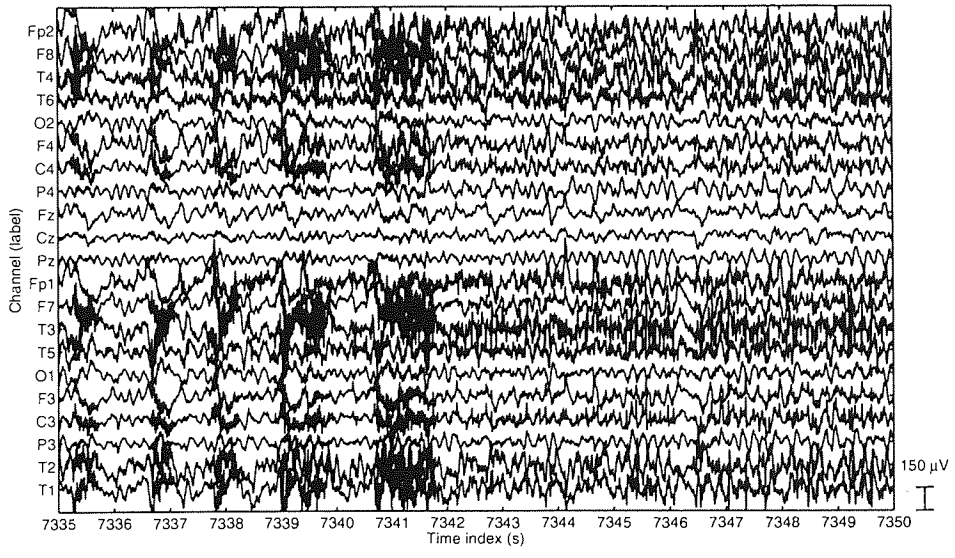

Figure 2.3: EEG recording during an epileptic event (epoch following the start of the seizure depicted in Figure 2.2). Note the hypersynchronous activity of the brain across all channels starting at $t = 7342$s. The vertical scale unit is 150μV.

2.1.3 Generators of the EEG

The surface electroencephalogram is the result of the summation, both in time and space, of potentials generated by underlying sources of the brain, recorded at electrodes positioned at the surface of the scalp. The aim of the forward problem is to find the distribution of electrode potentials at the surface of the scalp from a given distribution of underlying electrical sources (Hallez *et al.*, 2007):

$$\mathbf{V} = \mathbf{GD} + \varepsilon, \tag{2.1}$$

where $\mathbf{V}$ is the matrix of data measurements (i.e. distribution of electrode potentials), $\mathbf{G}$ is the gain matrix and $\mathbf{D}$ is the matrix of dipoles (underlying sources) at different time instants; ε is a noise perturbation.

Independent component analysis (ICA) is a blind source separation (BSS) technique commonly used in biomedical signal processing to extract and separate statistically independent sources underlying biomedical signals. In the framework of EEG analysis, ICA is used to extract the noise perturbation ε in Equation 2.1 as one or multiples statistically independent sources from multi- or single channel (by the means of embedding techniques such as time-delay embedding, Section 2.2.1) recordings. The statistically independent noise sources consist of ECG- or ballistocardiographic-contamination (James & Gibson, 2003; Nakamura *et al.*, 2006), time-frequency constrained signals such as the 50-60Hz contamination of EEG signals, patterns with particular spatial projections such as eye blinks or bursts of muscle activity.

The observed data matrix $\mathbf{x}(t) = [x_1(t), x_2(t), \ldots, x_n(t)]^{\mathrm{T}}$ with n mixtures and T samples is assumed to be a combination of m unknown underlying sources $\mathbf{s}(t) = [s_1(t), s_2(t), \ldots, s_m(t)]^{\mathrm{T}}$:

$$\mathbf{x}(t) = \mathbf{A}\mathbf{s}(t), \tag{2.2}$$

where $\mathbf{A}$ is the $n \times m$ mixing matrix describing the mixing of the sources, generally assumed to be linear; and the number of underlying sources is assumed to be less than or equal to the number of measurement channels ($m \leq n$).

The goal of ICA is to estimate the original sources $\mathbf{s}(t)$ and a de-mixing matrix $\mathbf{W}$ from the observations $\mathbf{x}(t)$ only:

$$\mathbf{s}(t) = \mathbf{W}\mathbf{x}(t). \tag{2.3}$$

The model in Equation 2.3 assumes a linear, noiseless mixing. The linear mixing of

sources assumed in this model is reasonable in a biomedical framework (e.g. the potential recorded at the interface of the electrode and the skull is assumed to result from the linear summation of potentials generated by underlying sources in the brain). The linear mixing assumption also implies an instantaneous mixing which does not necessarily stand: the potential recorded at the interface electrode-skull results from the summation of potentials generated by underlying generators spatially disseminated in the brain and transmitted in a non-homogenous medium inducing lags between distant sources.

In order to make the de-mixing problem (Equation 2.3) more tractable, ICA assumes the stationarity of the mixing and the statistical independence of sources. The stationarity of the mixing is ensured by the assumption of the stationarity of the mixing matrix: the statistical properties of the mixing matrix $\mathbf{A}$ do not change with time. In the framework of brain signals, such an assumption comes down to considering the biophysical properties of the brain fixed whereas the intensities of the sources distributed within this structure vary. The fundamental property which allows for the estimation of the underlying sources $\mathbf{s}(t)$ and of the de-mixing matrix $\mathbf{W}$ is the statistical independence of sources. A class of ICA algorithms impose the assumption of statistical independence through high-order statistics: statistical independence can be obtained by making the estimates of the underlying sources as non-Gaussian as possible (e.g. non-Gaussianity through kurtosis). The search for statistically independent estimates of sources comes down to the search for non-Gaussian sources.

When no information about the nature of the artifactual sources to be removed from the original EEG measurement is available, signal processing of the original observations, including artifact removal, can be performed by ICA methods and removal of sources of corruption of the observations. Such sources are not restricted to artifactual sources but also to noise sources. These components need to be identified either by manual inspection or by automated inspection using methods such as Fourier transform (in order to estimate their spectral content; e.g. components of frequency greater than 30Hz are not expected to originate from brain processes) before being removed by setting the columns of the mixing matrix to zero:

$$\hat{\mathbf{x}} = \hat{\mathbf{A}}\mathbf{s}(t)\,, \tag{2.4}$$

with $\hat{\mathbf{A}}$ the mixing matrix whose columns corresponding to corrupting components have been set to zero.

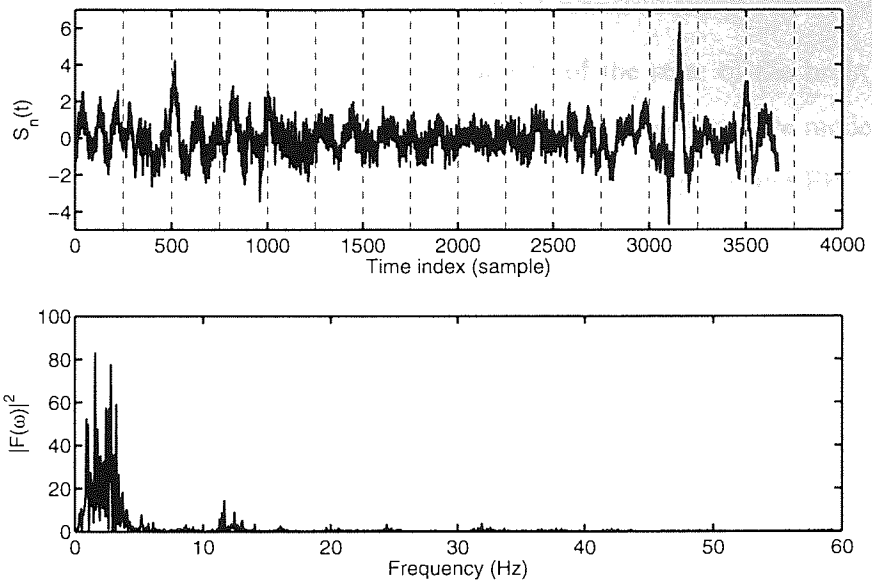

Figure 2.4: Periodogram (left-hand plot) of an independent component (right-hand plot) obtained from the ICA decomposition of an embedded single channel of 15s-EEG with: $\tau = 1$, the time delay; $m = 83$, the embedding dimension. The vertical lines denote one second.

The lower plot in Figure 2.4 is a plot of the periodogram of the independent component (IC) shown in the upper plot. The independent component was obtained from the ICA decomposition of an embedded single channel of 15 seconds-EEG. The embedding dimension m was chosen to be at least as large as the longest observable feature of interest in the EEG time series, the 3Hz spike-wave complex, accounting for 83 samples (the original signal was sampled at 250Hz). The FastICA algorithm (Hyvärinen & Oja, 2000) is applied to the embedded single channel and the IC shown in the upper plot in Figure 2.4 is kept due to its biological relevance to the EEG signal.

The biological relevance of independent components to the EEG signal is difficult to assess due to the ICA decomposition obtained from an embedded single channel of EEG heavily relying on the choice of the embedding dimension m. In the framework of the Thesis the artifact- and noise reductions by means of ICA decomposition are not achievable: the stationarity of the mixing is violated for non-stationary signals such as long-term EEG recordings.

2.2 Measures of complexity

In this Thesis two definitions of the complexity of the state of the brain are given out of the definitions possible (such as, e.g., the order of autoregressive models fitted to the EEG signal on fixed-length windows or the spectral entropy of the EEG signal (Rezek & Roberts, 1998)). The first definition refers to the complexity of the state of the brain as the dimension of the object in the phase space on which the dynamics of the system are embedded. The EEG signal is considered as the output of a deterministic system of relatively low complexity, but containing highly non-linear elements (Lehnertz & Elger, 1995). The dynamics of such systems evolve in a region of the phase space: the attractor. Changes in the dynamics of the system (due to the performance of a cognitive task or due to a condition) lead to modifications in the shape of the attractor: its dimension. In this Thesis the changes in the dimension of the attractor, due to the occurrence of ictal events, will be estimated using the correlation dimension (Section 2.2.1).

The second definition refers to the complexity of the state of the brain as the information content of the electroencephalographic signal. The estimation of the changes in the complexity of the state of the brain relies on the estimation of the amount of novel information conveyed by the electroencephalographic signal. The measures chosen to estimate this quantity are measures of information (Section 2.2.2).

2.2.1 Nonlinear measures

The electromagnetic processes recorded at the surface of the skull (such as the EEG or the magnetoencephalogram (MEG)) are considered to be timely and spatially smoothed mixtures of underlying unknown source generators (or cortical processes) combined with noise. The dynamics of such systems are embedded within an unobservable phase space on an attractor whose properties can be estimated by nonlinear measures. The correlation dimension D_2 (Grassberger & Procaccia, 1983b,a; Kantz & Schreiber, 2002) has been applied to EEG time series to measure the number of degrees of freedom of the object in the phase space on which the dynamics of the brain (as described by noisy observations) evolve (Elger *et al.*, 2000a,b; Lehnertz & Elger, 1995). The measure has been applied to the detection of epileptic seizures which are highly nonlinear events as opposed to background activity. The correlation dimension is an indirect measure of the loss of complexity of the state of the brain during ictal events through the characterisation of the

timely and spatially summated hypersynchronous activities of epileptogenic areas of the brain.

The nonlinear analysis of EEG time series relies on two steps: the reconstruction of the system dynamics in the phase space and the characterisation of the reconstructed attractor. In this Thesis the dynamics of the system are reconstructed from observations by the method of delays (time-delay embedding) and the reconstructed attractor is characterised by the correlation dimension. In nonlinear time series analysis a third step is usually undertaken to check the validity of the analysis: surrogate data testing. The method consists in performing the nonlinear analysis of a time series of interest and of a control time series with similar linear properties but no nonlinear structure. If the estimates differ, the nonlinear analysis of the original time series is valid (Stam, 2005). In this Thesis surrogate data testing is not performed as the correlation dimension is used as an estimate of different brain states.

Method of delays

The first step in the nonlinear analysis of EEG time series is the reconstruction of the attractor in the phase space on which the dynamics of the system are embedded. Whitney (Whitney, 1936) demonstrated that if the system from which the observations x_i, $i = 1,\ldots,N$, are taken has an attractor Γ and if the embedding dimension m is greater than twice the dimension of the system attractor (i.e. $m \geq 2D_\Gamma + 1$), the time series converted to a series of vectors X_i, $X_i = \{x(i), x(i+\tau), x(i+2\tau), \ldots, x(i+(m-1)\tau)\}^T \in \Re^m$, where τ is a time delay, in an m-dimensional embedding space constitute an equivalent attractor Γ'. Takens (Takens, 1981) proved that the equivalent attractor Γ' had the same dynamical properties (such as the dimension) as the true attractor Γ.

The delay vectors form an embedding matrix M that traces a trajectory on the attractor Γ' generated by the Euclidean embedding:

$$
\begin{aligned}
M &= \left[X_i, X_{i+\tau}, \ldots, X_{i+(N-m+1)\tau}\right] \\
&= \begin{bmatrix}
x_i & x_{i+\tau} & \cdots & x_{i+(N-m+1)\tau} \\
x_{i+\tau} & x_{i+2\tau} & \cdots & x_{i+(N-m)\tau} \\
\vdots & \vdots & & \vdots \\
x_{i+(m-1)\tau} & x_{i+m\tau} & \cdots & x_{i+N\tau}
\end{bmatrix}
\end{aligned}
$$

The left-hand subplots in Figures 2.5 and 2.6 are plots of sixteen seconds of EEG dur-

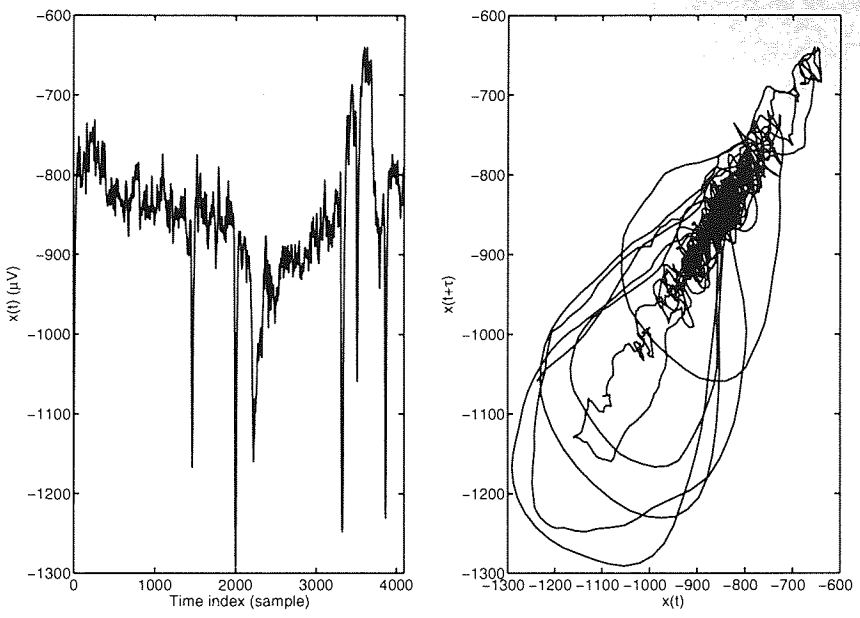

Figure 2.5: Left plot: EEG time series during an interictal state; Right plot: Attractor corresponding to the EEG time series shown in the right plot. The attractor is high dimensional and reflects a low level of synchronisation of the underlying neural networks.

ing interictal- and ictal events, respectively. The right-hand subplots are two-dimensional phase portraits of the corresponding attractors. For visualisation purposes the embedding dimension m was set to 2 and the time-delay τ was set to 10. The recognisable structure in Figure 2.6, right-hand subplot, denotes the high level of synchronisation in the underlying neural networks during ictal events.

The next step in the nonlinear analysis of EEG time series is the characterisation of the reconstructed attractor on which brain dynamics evolve in the phase space by the correlation dimension D_2.

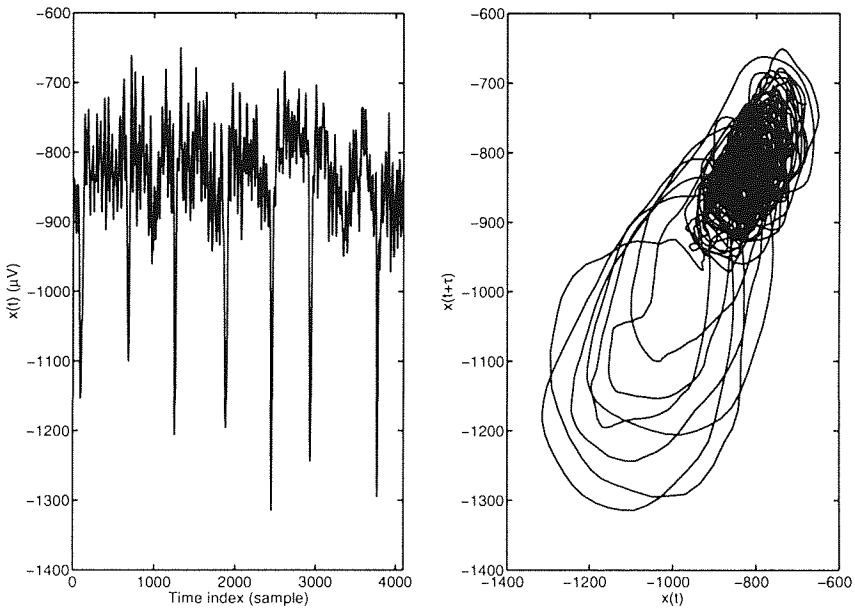

Figure 2.6: Left plot: EEG time series during an ictal state; Right plot: Attractor corresponding to the EEG time series shown in the right plot. The attractor is low dimensional and reflects a high level of synchronisation of the underlying neural networks, to be compared to the attractor corresponding to an interictal state in Figure 2.5.

Correlation dimension

One way to characterise the reconstructed attractor Γ' in a quantitative way is to compute its correlation dimension D_2 (Grassberger & Procaccia, 1983b,a; Hegger *et al.*, 1999). The correlation integral C_ε from which the correlation dimension is derived counts the number of pairs of randomly chosen points on the attractor that are closer than a given hypersphere radius ε:

$$C_\varepsilon = \frac{2}{(N-m+1-W)(N-m-W)} \sum_{i=1}^{N-m+1} \sum_{j=i+W}^{N-m+1} \Theta(\varepsilon - \|X_i - X_j\|) \qquad (2.5)$$

where $\|\cdot\|$ is an m-dimensionsal norm and Θ is the Heaviside step function. The Theiler window of length W ensures that pairs close in time are not compared to reduce the influence of temporal correlations. D_2 is defined as $D_2 = \lim_{N\to\infty} \lim_{\varepsilon\to\infty} d(\varepsilon)$ with $d(\varepsilon) = d\ln C_\varepsilon / d\ln\varepsilon$: for a sufficiently high embedding dimension m, the correlation dimension is approximated by the slope of a linear scaling region of $\ln C_\varepsilon / \ln\varepsilon$ (Grassberger & Procaccia, 1983b,a).

The correlation sum D_2 is estimated from a deteriorating sinusoidal signal (Figure 2.11, upper plot) in Figures 2.7 and 2.8 for a purely sinusoidal- and a deteriorated sinusoidal signal, respectively:

$$x_t = \begin{cases} \sin(\omega t) & \text{for } t \leq 3000 \\ (1 - t/T)\sin(\omega t) + (t/T)\eta_t & \text{for } t > 3000\,, \end{cases} \qquad (2.6)$$

with $T = 6000$, η_t is a zero-mean unit-variance Gaussian noise and the sampling frequency is 100 Hz. The reconstructed attractor from a sinusoidal signal is a limit cycle, a closed loop corresponding to a periodic system, whose correlation dimension is known (Stam, 2005): $D_2 = 1$. The first plateau is difficult to observe and is subject to interpretation. The correlation dimension of the deteriorating sinusoidal signal is impossible to estimate since no plateau is observed. The estimation of the correlation dimension has been reported as a difficult and delicate problem.

Figures 2.9 and 2.10 are plots of the local slopes of the logarithm of the correlation sum during the interictal- and ictal events whose EEG recordings and attractors are plotted in Figures 2.5 and 2.6, respectively. The loss of complexity of the state of the brain during the ictal event is impossible to observe from the estimated values of the correlation sum for interictal- and ictal events: since no plateau is observable, the correlation dimension of the interictal- and ictal time-series is impossible to estimate.

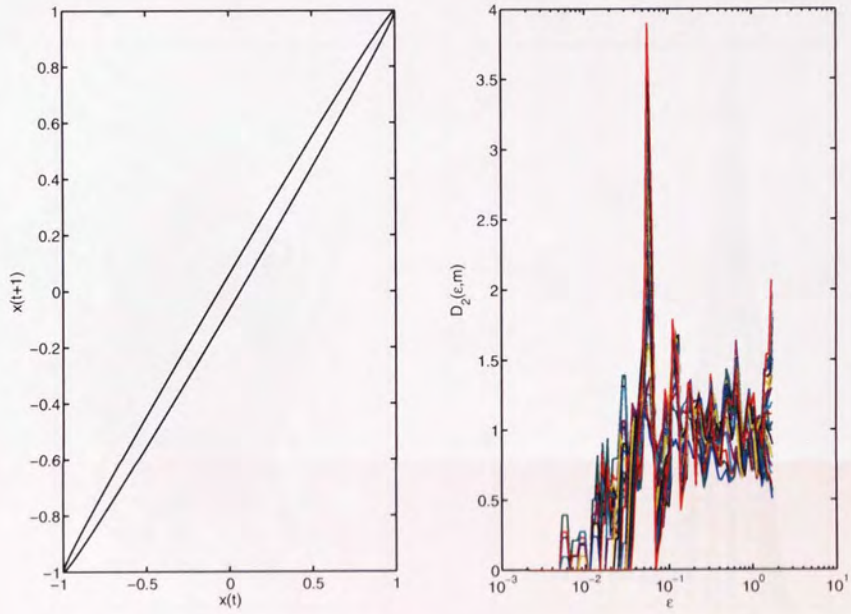

Figure 2.7: The left-hand figure is a plot of the two-dimensional phase portrait of the reconstructed attractor Γ' of a sinusoidal signal. The right-hand figure is the plot of the estimates of the slopes of the correlation sum C_ε for a range of values ε and for a range of embedding dimensions m (2 to 24). Note the reconstructed attractor of the sinusoidal signal is limit cycle, a closed loop corresponding to a periodic system, whose known correlation dimension ($D_2 = 1$) is difficult to estimate from the plot of correlation sums slopes.

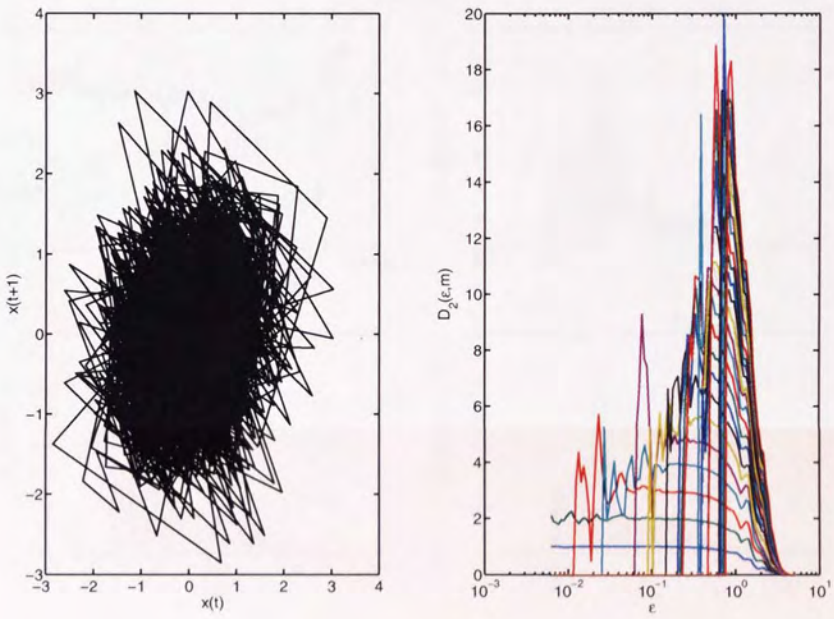

Figure 2.8: The left-hand figure is a plot of the two-dimensional phase portrait of the reconstructed attractor Γ' of a deteriorating sinusoidal signal. The right-hand figure is the plot of the estimates of the slopes of the correlation sum C_ε for a range of values ε and for a range of embedding dimensions m (2 to 24). The correlation dimension of the system is difficult to estimate from the plot of correlation sums slopes.

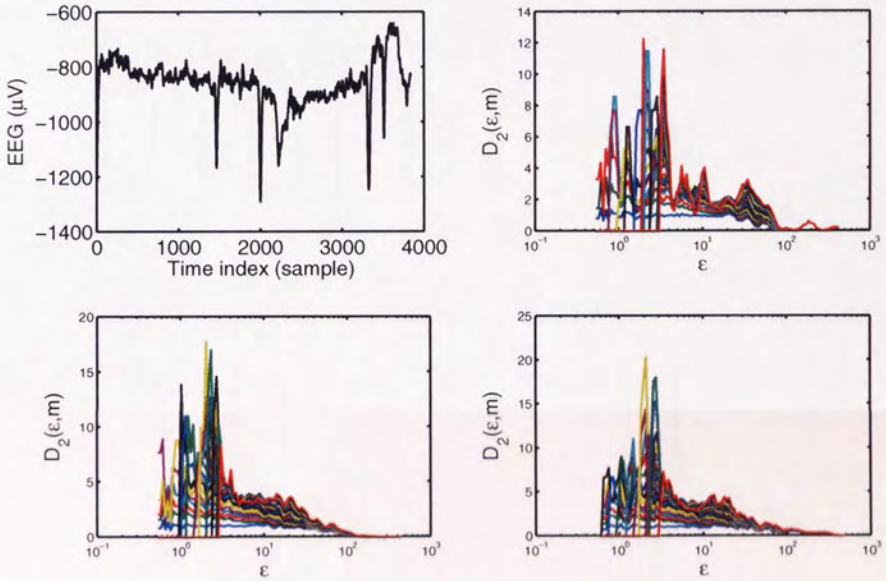

Figure 2.9: Local slopes of the logarithm of the correlation sum C_ε, for a range of values ε and for a range of embedding dimensions m (2 to 24), during an interictal event, computed from one (top-right), five (bottom-left) and ten seconds (bottom-right) of the original signal (top-left). Note that no plateau is observable making the estimation of the correlation dimension impossible.

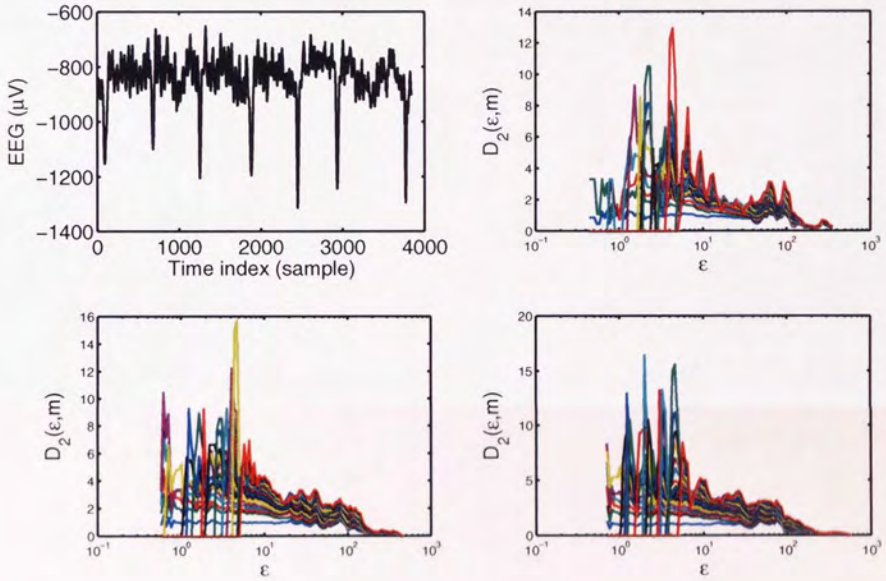

Figure 2.10: Local slopes of the logarithm of the correlation sum C_ε for a range of values ε and for a range of embedding dimensions m (2 to 24), during an ictal event, computed from one (top-right), five (bottom-left) and ten seconds (bottom-right) of the original signal (top-left). Note that no plateau is observable making the estimation of the correlation dimension impossible.

The correlation dimension is an indirect measure of the loss of complexity of the state of the brain during ictal events through the characterisation of the hypersynchronous activity of epileptogenic areas of the brain via noisy observations. The correlation dimension, estimated from the local slopes of the logarithm of the correlation sum for a range of embedding dimensions, is prone to misinterpretation making its integration in a fusion-of-information framework delicate. In this Thesis, the correlation dimension is discarded due to its limitations and alternative measures of information are investigated.

2.2.2 Information measures

The brain conveys information at different scales: at the microscopic scale, the information is conveyed via action potentials or trains of spikes along the axone of neurons; at the macroscopic scale, the information is conveyed within the brain (and the skull) via electrical currents: the EEG waveform. The information to be conveyed is encoded by a sender and is delivered via a communication channel to a receiver. The concepts of receiver, sender, encoded information and communication channel are reminiscent of Shannon's theory of communication (Shannon, 1948).

At the microscopic scale, the understanding of the neural code is aimed at getting an insight at the stimulus in the sensory world that generated the observed train of spikes. The encoding of the original phenomenon into the observed pattern is rarely a one-to-one representation: the same stimulus trigger responses (spikes trains) which vary from trial to trial. The neural coding introduces an element of randomness: the neural responses are not completely reproducible. Since no one-to-one mapping is achievable, gaining insight in the stimulus at the origin of an observed pattern comes down to quantifying the degree of randomness of the neural response. The degree of randomness is assessed from a time series of discrete values (either 0 for the absence of spike or 1 for the presence of a spike).

At the macroscopic scale, the understanding of the neural code is aimed at getting an insight at the phenomenon at the origin of the observed EEG pattern. The neural coding takes continuous values: a one-to-one mapping of the observed pattern onto the original stimulus is impossible to achieve.

For the second definition of the complexity of the state of the brain and with regards to its estimation towards ictal events detection, the information content of the electroencephalographic signal (which has been discussed to decrease during ictal events, in Section 2.1.2) needs to be estimated. In a previous paragraph, a parallel was drawn between the exchange of information in the brain and the concepts of receiver, sender, encoded information and communication channel reminiscent of Shannon's theory of communication (Shannon, 1948). The Shannon entropy is naturally motivated as one of the information measures used in this Thesis to estimate the changes in the information content of the electroencephalographic signal.

Shannon entropy

Entropy measures have been given multiple interpretations. In this Thesis, we are interested in two related interpretations of the entropy: the entropy as a measure of disorder and the entropy as a measure of information content (Bishop, 1995). In the context of ictal events detection the two interpretations are closely related since the hypersynchronous activity of the brain (which is an ordered state) does not convey novel information (the information content is poor).

For the first interpretation of the entropy consider a random variable x of probability density function $p(x)$, represented as a histogram: bins are labelled by an integer i and they contain N_i objects out of N identical discrete objects. The entropy gives a measure of the number of arrangements of objects in the bins which can give rise to a given histogram (or set of probabilities p_i):

$$H = -\sum_i p_i \ln p_i \,, \tag{2.7}$$

where $p_i = N_i/N$ as $N \to \infty$ is the probability of the ith bin.

The second interpretation of entropy in this Thesis is as a measure of information content or as a measure of the degree of novelty when a particular event has occurred. If the event is certain to occur, $p = 1$ and the occurrence of the event is expected (no surprise). Conversely, if the probability of the event to occur is low, the degree of surprise is large when the event occurs. The entropy of a random variable x which takes values x_i with probabilities $p(x_i)$ is the average amount of information transmitted when the value of x is observed:

$$H(x) = -\sum_i p(x_i) \ln p(x_i) \,, \tag{2.8}$$

where the amount of information required to transmit the value of x is $-\ln p(x_i)$ (bits or nats depending on the base of the logarithm: 2 or e, respectively) if the variable takes the value x_i.

The suitability of the Shannon entropy to the estimation of the complexity of a system (such as the brain), is demonstrated on a deteriorating sinusoid (Figure 2.11, upper plot; Equation 2.6). The Shannon entropy of the signal is computed on one-second windows with no overlap. The distribution of the random variable X is estimated from histograms with 101 bins linearly distributed on the interval $[-2, 2]$. The deteriorating sinusoid and the Shannon entropy estimated from the distribution of the signal are plotted in Figure 2.11 (upper and lower plots, respectively). The Shannon entropy of the signal increases

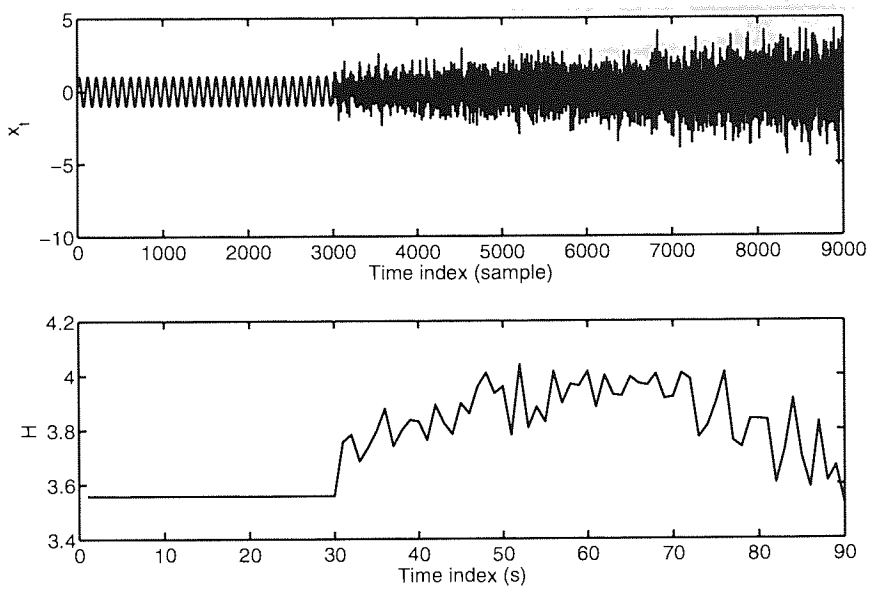

Figure 2.11: Shannon entropy (lower plot) of a deteriorating sinusoid (upper plot). Note the increase in H around $t = 30$s coinciding with the deterioration of the sinusoid.

as the sinusoid deteriorates up to the point when the Gaussian term in Equation 2.6 progressively dominates the sinusoid and the Shannon entropy decreases.

The extracellular potential fields recorded at the surface of the scalp as measurements of potential differences (i.e. the scalp EEG $\mathbf{V}$) are generated by dipole sources of the brain as solved by the forward problem:

$$\mathbf{V} = \mathbf{GD} + \varepsilon, \tag{2.9}$$

with $\mathbf{V}$ is the matrix of data measurements, $\mathbf{G}$ is the gain matrix, $\mathbf{D}$ is the matrix of dipole magnitudes at different time instants and ε is a noise matrix (Hallez *et al.*, 2007). The forward problem is uniquely solved by finding the potentials at the electrodes from a given dipole source configuration. The inverse problem (i.e. the estimation of the distribution of sources within the brain from EEG scalp measurements) is not uniquely defined and requires the solving of the forward problem. Ideally the estimation of the changes in the complexity of the state of the brain would have been performed by estimating the distribution of the generators of the EEG waveform and then by estimating their information content using information measures such as the Shannon entropy proposed in this Thesis. However the complexity of the inverse problem makes the estimation of the distribution of the dipole sources impractical and the changes in the complexity of the states of the

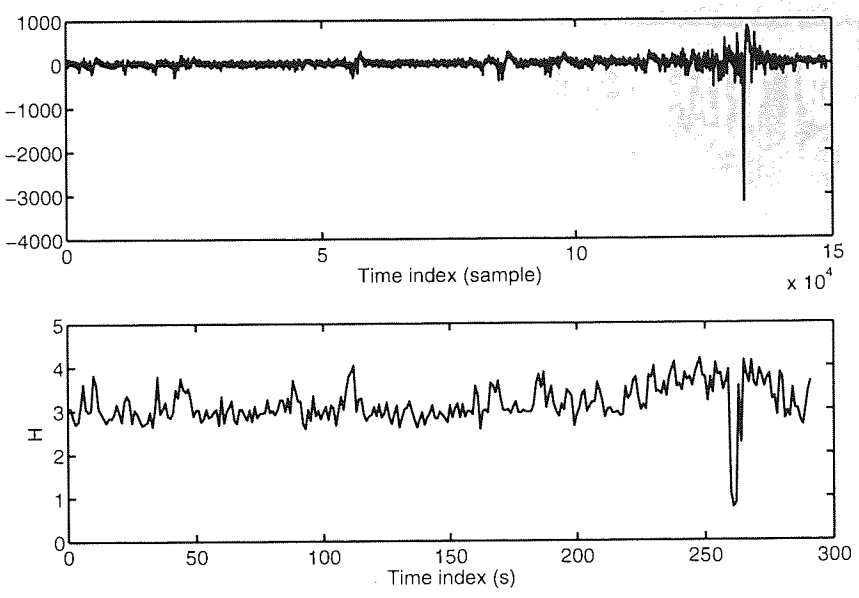

Figure 2.12: Shannon entropy (lower plot) of a single channel of intracranial EEG (upper plot). The entropy was computed from the distribution of the EEG data estimated with histograms on one-second windows with no overlap. Note the drop in H around $t = 262$s after the initial increase of the baseline at the start of the ictal event.

brain are rather estimated from the distribution of the electroencephalographic signal. The changes in the complexity of the state of the brain estimated by the Shannon entropy are computed in this Thesis on one-second windows with no overlap:

$$H(X) = -\sum_{x \in X} p(x) \log p(x), \tag{2.10}$$

where the distribution of the EEG waveform is estimated from histograms with 101 bins linearly distributed on the interval $[-2, 2]$.

In this Thesis the changes of the complexity of the state of the brain during ictal events are estimated by the computation of the Shannon entropy on two datasets of real patient data: intracranial EEG and scalp EEG. The advantage of intracranial EEG over scalp EEG is that the former are not contaminated by artifacts (such as muscle artifacts and eye blinks). An ictal event occurring at time $t = 271$s recorded by the 291 seconds-intracranial EEG plotted in Figure 2.12 (upper plot) provokes the sudden drop of the Shannon entropy (lower plot) at its climax. At the start of the event the baseline of the Shannon entropy increases slightly whereas at the end of the event the information measure slowly decreases back to its nominal level.

The Shannon entropy as computed from a single channel of scalp EEG, T3, of length

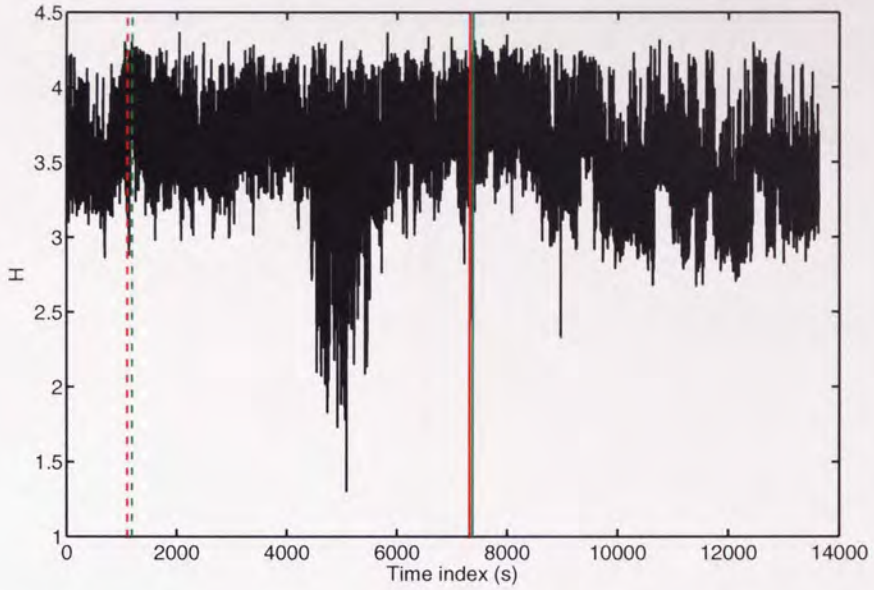

Figure 2.13: Shannon entropy of a single channel of EEG (T3) estimated from the distribution of the EEG signal. The plain vertical red and green lines denote the start and end of an a priori labelled temporal lobe epileptic seizure. The draft vertical red and green lines denote the start and end of an a posteriori labelled temporal lobe epileptic seizure. Note the values of the Shannon entropy during ictal events are not discernable from the ones during interictal states.

13630 seconds (3,407,500 samples) is plotted in Figures 2.13 (for the whole recording), 2.14 (for an epoch centered around the a priori labelled ictal event) and 2.15 (for an epoch centered around the a posteriori labelled ictal event). The plain vertical red and green lines denote the start and end of an a priori labelled temporal lobe epileptic seizure. The dotted vertical red and green lines denote the start and end of an a posteriori labelled temporal lobe epileptic seizure.

At the local scale (Figures 2.14 and 2.15), during ictal events, the following pattern of the Shannon entropy estimated from the distribution of the EEG signal is observed: slow decrease of the measure at the start of the ictal event towards a minimum, followed by the increase of the measure towards the end of the ictal event to a level higher than the baseline before the event and finally slight decrease of the measure towards the baseline level before the event.

The Shannon entropy estimated from the distribution of intracranial and scalp EEG recordings exhibit similar patterns during ictal events. However, while the discrimination between ictal- and interictal epochs from the estimation of the information measure from

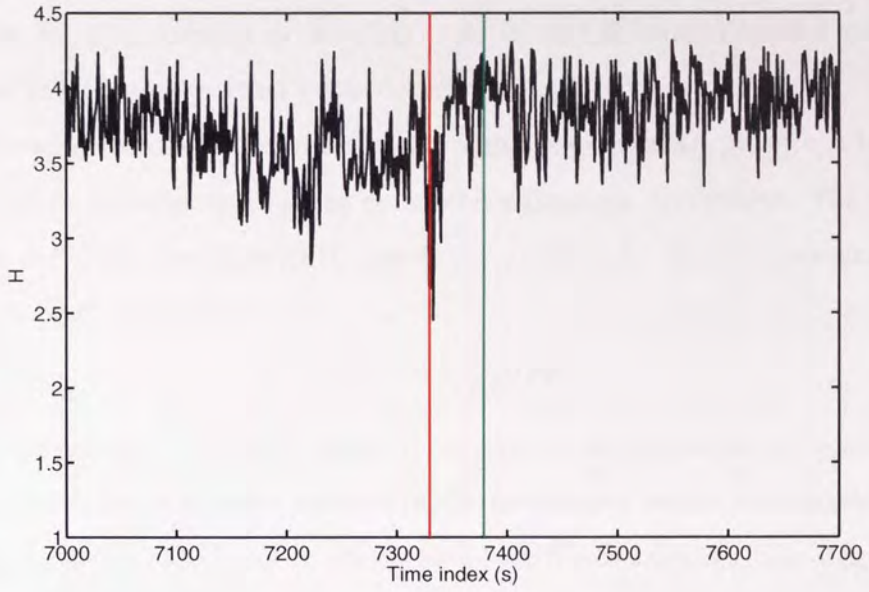

Figure 2.14: Detail of the Shannon entropy of a single channel of EEG (T3) estimated from the distribution of the EEG signal for the a priori labelled temporal lobe epileptic seizure. Note the Shannon entropy decreases at the start of the ictal event before increasing back to its interictal level.

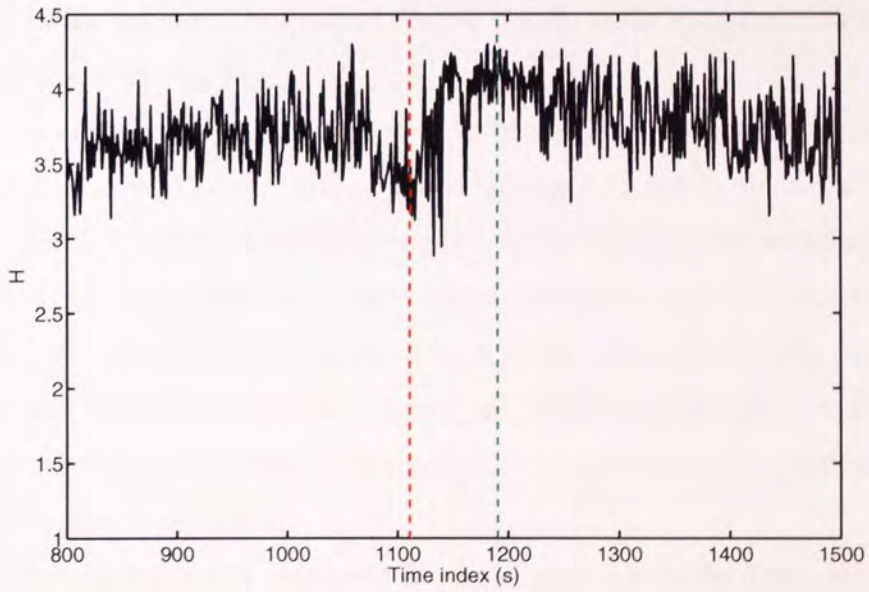

Figure 2.15: Detail of the Shannon entropy of a single channel of EEG (T3) estimated from the distribution of the EEG signal for the a posteriori labelled temporal lobe epileptic seizure. Note the Shannon entropy decreases at the start of the ictal event before increasing back to its interictal level as in Figure 2.14.

intracranial EEG recordings is unambiguous, it seems impossible to achieve from the estimation of the information measure from noisy scalp EEG recordings due to the dramatic number of false positives that would occur.

Assuming the electroencephalographic signal is a stationary process, it is possible to approximate the latter as a filtered noise with a Gaussian distribution. The operation of inverse autoregression filtering (Lopes da Silva, 1993) produces a zero-mean Gaussian noise, e_k, with variance σ^2:

$$e_k = x_k - \sum_{j=1}^{p} a_j x_{k-j}\,, \tag{2.11}$$

with e the residual; x the EEG signal; p the order of the autoregressive model estimated using the Akaike information criterion (AIC) (the range of orders investigated is $[2-12]$).

In this Thesis autoregressive models have been fitted to the EEG signal on one-second windows with no overlap (Figure 2.16) on which the EEG signal is deemed to be stationary (Lopes da Silva *et al.*, 1975). As the changes in the complexity of the electroencephalographic signal were estimated from the computation of the Shannon entropy, the changes in the complexity of the residual time series are estimated from the computation of the Shannon entropy of its distribution estimated from histograms with 101 bins linearly distributed on the interval $[-2,2]$. The Shannon entropy of the residual was estimated on the deteriorating sinusoid (Equation 2.6), on the intracranial EEG and on the scalp EEG recordings.

The lower plot in Figure 2.17 is the plot of the Shannon entropy of the residual of the inverse autoregressive filtering. When the signal is purely sinusoidal (upper plot, epoch from 0 to 3,000 samples), the perfect fit of autoregressive models to sinusoidal signals causes the residual and its Shannon entropy to be null. The Shannon entropy of the residual increases (lower plot, epoch from 30 to 90 seconds) with the deterioration of the sinusoid. Theses observations are compatible with the interpretation of entropy as a measure of information content: non-informative signals have lower entropy than signals containing novel information.

Similarly to the results obtained from the computation of the Shannon entropy from the distribution of the EEG signal, the Shannon entropy computed from the distribution of the residual of an inverse autoregressive filter exhibits a specific pattern during ictal events (Figure 2.18 for the intracranial EEG and Figures 2.19, 2.20 and 2.21 for the whole scalp EEG and around the a priori- and a posteriori labelled ictal events): increase at the start

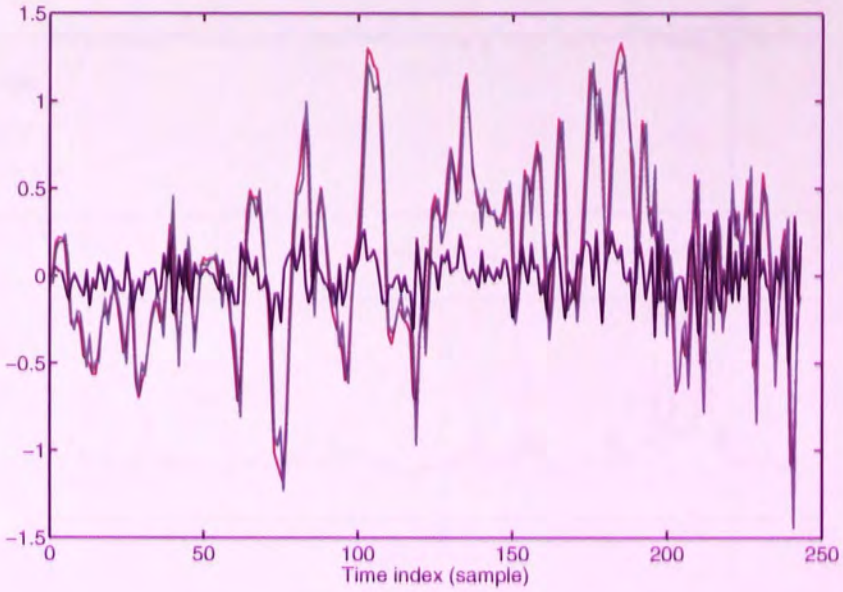

Figure 2.16: Autoregressive modelling of one second of EEG time series (sampling rate: 250Hz). The observed data is plotted in red, the autoregressive model fitted to the data is plotted in green and the residual is plotted in black.

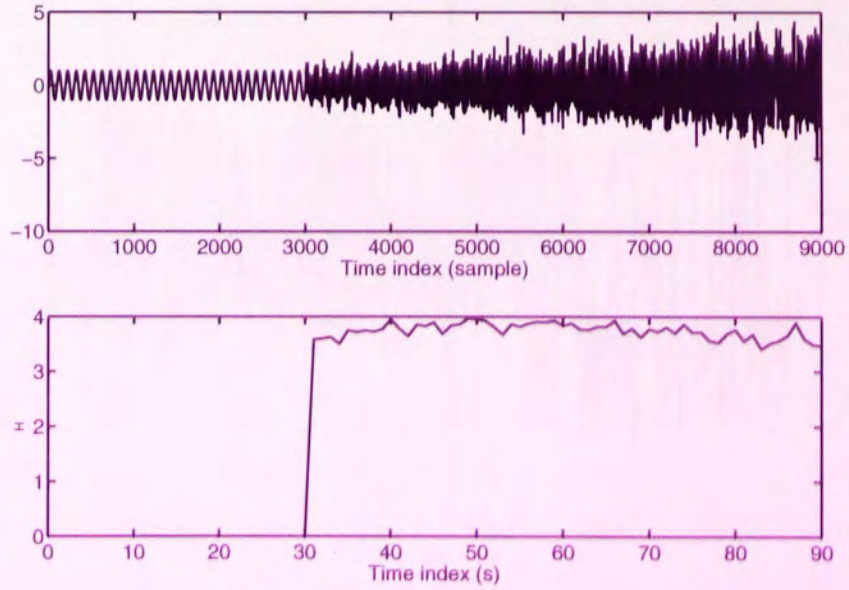

Figure 2.17: Shannon entropy (lower plot) of a deteriorating sinusoid (upper plot) computed from the distribution of the residual on an inverse autoregressive filter. Note the null value of the Shannon entropy of the residual when the signal is sinusoidal and the increase in H around $t = 30$s coinciding with the deterioration of the sinusoid.

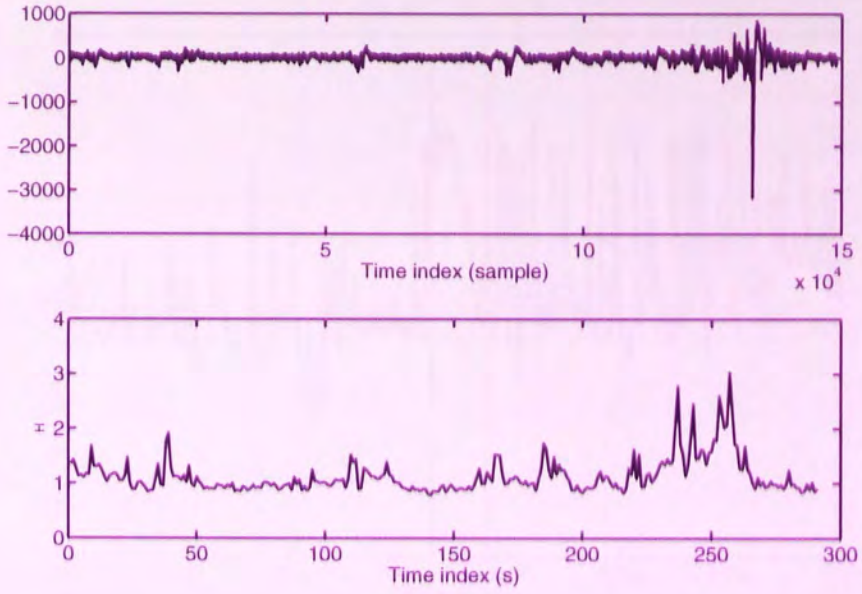

Figure 2.18: Shannon entropy (lower plot) of a single channel of intracranial EEG (upper plot). The entropy was computed from the distribution of the residual on an inverse autoregressive filter estimated with histograms on one-second windows with no overlap. Note the increase in H during the ictal event.

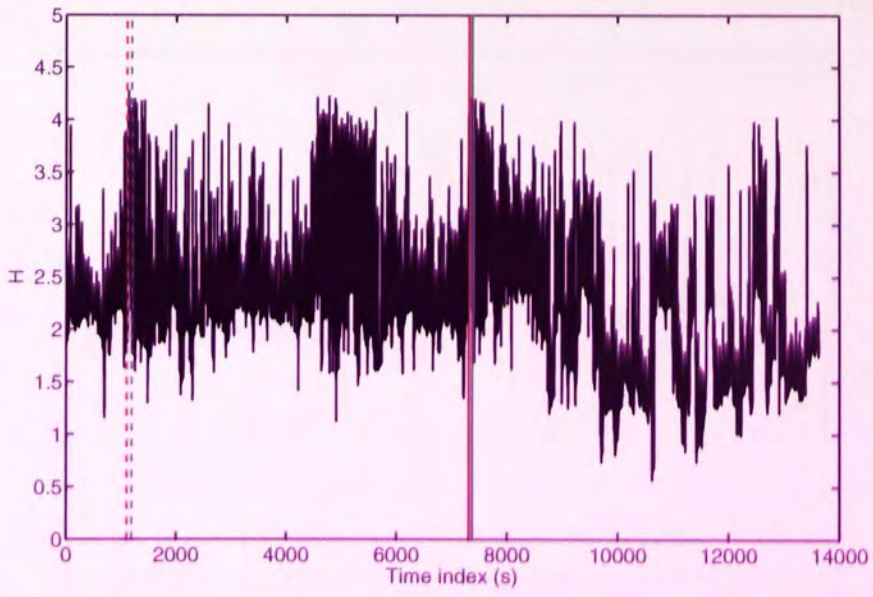

Figure 2.19: Shannon entropy of a single channel of EEG (T3) computed from the distribution of the residual on an inverse autoregressive filter. The plain vertical red and green lines denote the start and end of an a priori labelled temporal lobe epileptic seizure. The draft vertical red and green lines denote the start and end of an a posteriori labelled temporal lobe epileptic seizure. Note the increase in H during the ictal event.

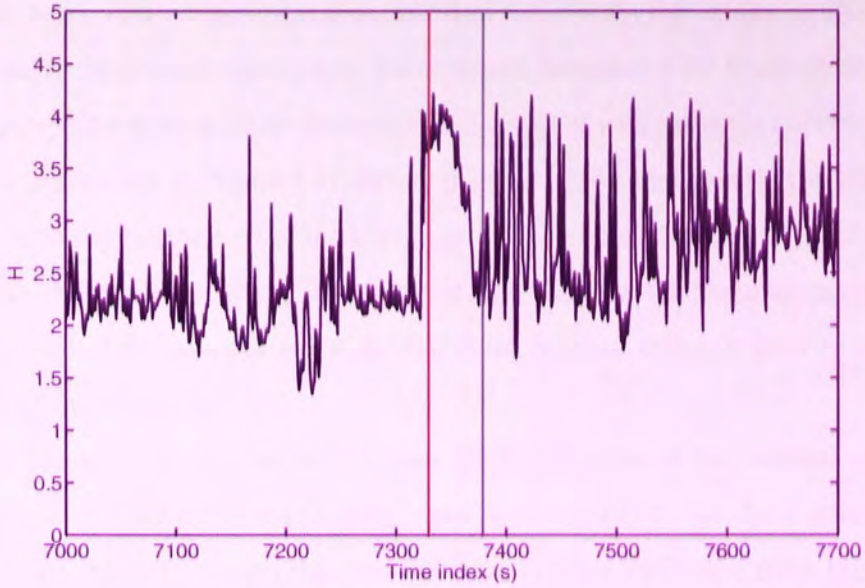

Figure 2.20: Detail of the Shannon entropy of a single channel of EEG (T3) computed from the distribution of the residual on an inverse autoregressive filter for the a priori labelled temporal lobe epileptic seizure. Note the increase in H during the ictal event.

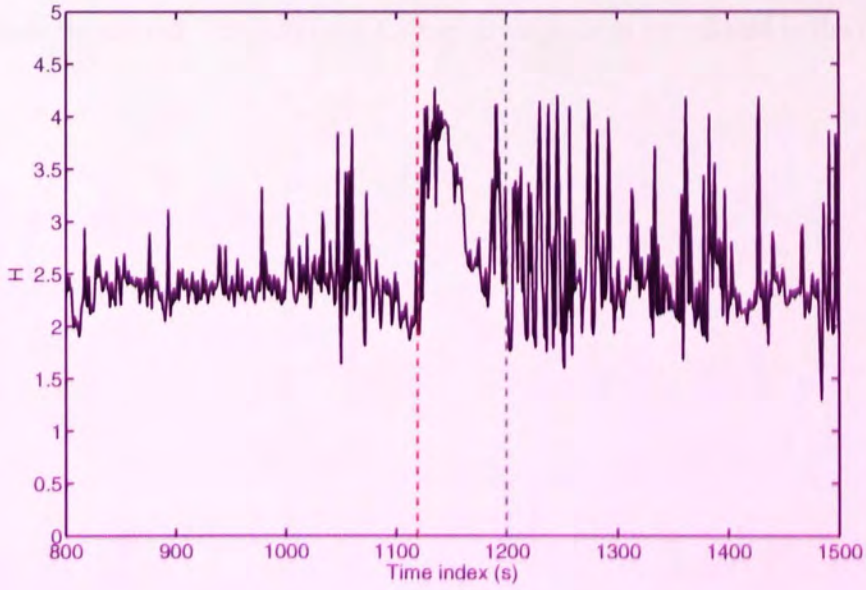

Figure 2.21: Detail of the Shannon entropy of a single channel of EEG (T3) computed from the distribution of the residual on an inverse autoregressive filter for the a posteriori labelled temporal lobe epileptic seizure. Note the increase in H during the ictal event.

of the epileptic event, drop, return to the value before drop and slow decrease back to a nominal level. The results on real patient data differ from the results on theoretical data described in the previous paragraph: the expected decrease of the Shannon entropy due to the hypersynchronous activity observable at the start of ictal events is not observed on real patient data (except in Figure 2.21, before the start of the ictal event). The increase of the Shannon entropy at the start of the ictal event is due to the noisy activity of the brain after the onset of the epileptic event. The episodic high values of the Shannon entropy observed after the end of the epileptic event are due to the residual epileptic activity observable at the end of the ictal event.

The Shannon entropy estimated from the distribution of the residual of an inverse autoregressive filter performs slightly better with regards to the discrimination of ictal events from interictal events than the Shannon entropy estimated from the distribution of the electroencephalographic signal. However the measure is not only sensitive to the change of complexity of the residual during ictal events but also to the ones due to chewing artifacts (Figure 2.19, epoch from 4000 to 6000 seconds).

One problem with the entropy measure discussed in this Section is that it is not referenced with respect to any state of normality. To perform the unambiguous estimation of the complexity of the state of the brain with regards to ictal events a relative measure of complexity is needed. The Kullback-Leibler divergence is introduced in the next Section.

Kullback-Leibler divergence

In the previous Section the sensitivity of the distribution of the residual of inverse autoregressive filters to the changes of the state of the brain, with regards to ictal events, was established by the results provided by the computation of the Shannon entropy. However the information measure is not referenced with respect to any state of normality, making it sensitive to ictal events but also to artifacts (Figure 2.19, epoch from 4000 to 6000 seconds: the pattern of the Shannon entropy coincide with the observation of chewing artifacts on the corresponding EEG signal).

During ictal events the assumption that the EEG signal is stationary on windows of length up to 30 seconds is violated. Consequently the null hypothesis (i.e. the EEG signal follows the assumption of stationarity and can be expressed in terms of the properties of the estimated noise resulting from the inverse autoregressive filtering (Lopes da Silva, 1993)) is violated. The null hypothesis is rejected if the noise resulting from the inverse autoregressive filtering deviates at a certain probability level from a noise with a Gaussian distribution (Lopes da Silva, 1993). In these conditions the state of normality referred to in the previous paragraph is chosen to be a Gaussian distribution to be compared to the distribution of the residual of the inverse autoregressive filter estimated on one-second windows with no overlap from histograms with 101 bins linearly distributed on the interval $[-2,2]$. The Kullback-Leibler divergence is the measure chosen to compare the distribution of the residual with the distribution of the normal state.

The Kullback-Leibler (KL) divergence or relative entropy $D(p||q)$ is a measure of the inefficiency of assuming that the distribution is q when the true distribution is p (Cover & Thomas, 2005):

$$D(p||q) = \sum_{x \in \mathcal{X}} p(x) \log \frac{p(x)}{q(x)}. \tag{2.12}$$

The measure was successfully applied for the detection of epileptic events: the distribution p of the data on a fixed-length window was estimated and compared to a reference distribution of interictal EEG, q, identified before the analysis of the full-length EEG recording (Quian Quiroga *et al.*, 2000). This method requires a partial scrolling of the EEG record before its analysis in order to identify nominal epochs not contaminated by artifacts or by interictal patterns (spikes, spike-and-wave complexes).

In this Thesis the Kullback-Leibler divergence was applied to estimate the changes in the distribution of the residual of inverse autoregressive filters (Equation 2.11 and Figure

2.16), p_e, with respect to a reference Gaussian distribution q:

$$D(p_e||q) = \sum_{x \in X} p_e(x) \log \frac{p_e(x)}{q(x)}, \tag{2.13}$$

where p_e was estimated on one-second windows with no overlap from histograms with 101 bins linearly distributed on the interval $[-2,2]$; q is a zero-mean Gaussian with variance in the range $[0.01,2.01]$. Multiple variances for the reference distribution q were investigated due to the variability of the variances of the distributions of the residual p_e on one-second windows.

Figure 2.22 shows the influence of the variance of the reference Gaussian distribution q for a fixed Gaussian distribution p_e, when the variance of q is less than, equal to, and greater than the variance of the fixed Gaussian distribution p_e. The Kullback-Leibler divergence, which is not a distance measure due to its asymmetry, dramatically decreases when $\sigma_q^2 < \sigma_{p_e}^2$ and σ_q^2 tends to $\sigma_{p_e}^2$; equals zero when $p_e = q$; steadily increases with $\sigma_q^2 > \sigma_{p_e}^2$.

The influence of the variance of the reference Gaussian distribution q on the values of the Kullback-Leibler divergence computed on a one second-window for an interictal epoch are shown in Figure 2.23. The top, left subfigure shows a steady increase of the value of the Kullback-Leibler divergence with the increase of the variance σ_q^2 of the reference Gaussian distribution q. The pattern observed in Figure 2.22 is not observed for interictal epochs due to the fact that the distribution of the residuals is narrower than the reference Gaussian distributions.

The influence of the variance of the reference Gaussian distribution q on the values of the Kullback-Leibler divergence computed on a one second-window for an ictal epoch are shown in Figure 2.24. The top, left subfigure shows that for ictal episodes the values of the Kullback-Leibler divergence follow the same pattern as in Figure 2.22: the Kullback-Leibler divergence dramatically decreases when $\sigma_q^2 < \sigma_{p_e}^2$ and σ_q^2 tends to $\sigma_{p_e}^2$; reaches a minimum when $\sigma_q^2 \approx \sigma_{p_e}^2$; steadily increases with $\sigma_q^2 > \sigma_{p_e}^2$.

Following the observations made in Figures 2.22, 2.23 and 2.24, the variance of the reference Gaussian distribution is chosen such that the Kullback-Leibler divergence for ictal episodes is maximised when compared to the Kullback-Leibler divergence for interictal episodes. Such a contrast in the measure is obtained for $\sigma_q^2 < \sigma_{p_e}^2$. The Kullback-Leibler divergence will be computed on real patient data with $\sigma_q^2 = 0.0616$.

The KL-divergence as computed from channel T3 for a continuous 13,630 seconds

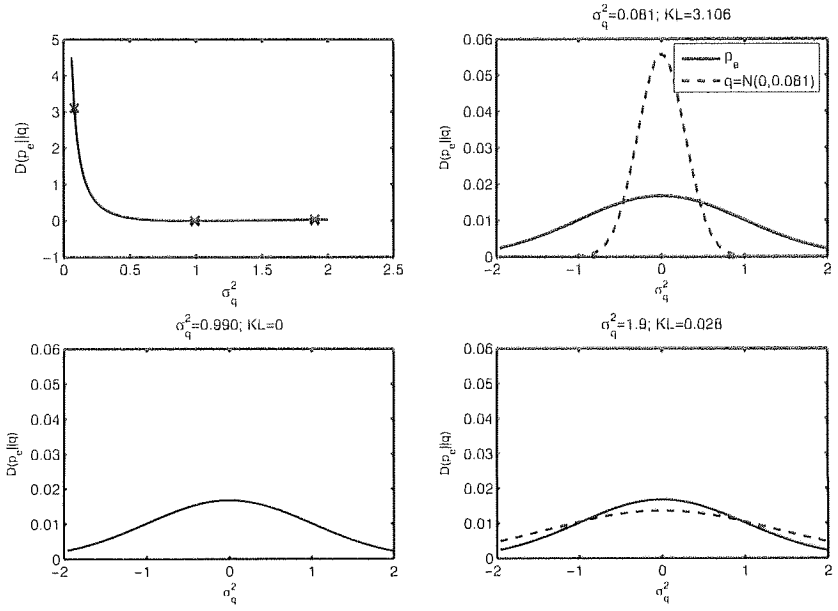

Figure 2.22: Computation of the Kullback-Leibler divergence between a Normal distribution (referred to as p_e) and a reference Normal distribution (q). The influence of the variance of q, σ_q^2, in the computation of the Kullback-Leibler divergence is investigated: when σ_q^2 is less than the variance $\sigma_{p_e}^2$ of the fixed distribution (top, right); when $\sigma_q^2 = \sigma_{p_e}^2$ (bottom, left); when $\sigma_q^2 > \sigma_{p_e}^2$ (bottom, right). Top, left: value of the Kullback-Leibler divergence as a function of σ_q^2. The crosses denote the values of the Kullback-Leibler divergence for the variances σ_q^2 investigated in the subfigures.

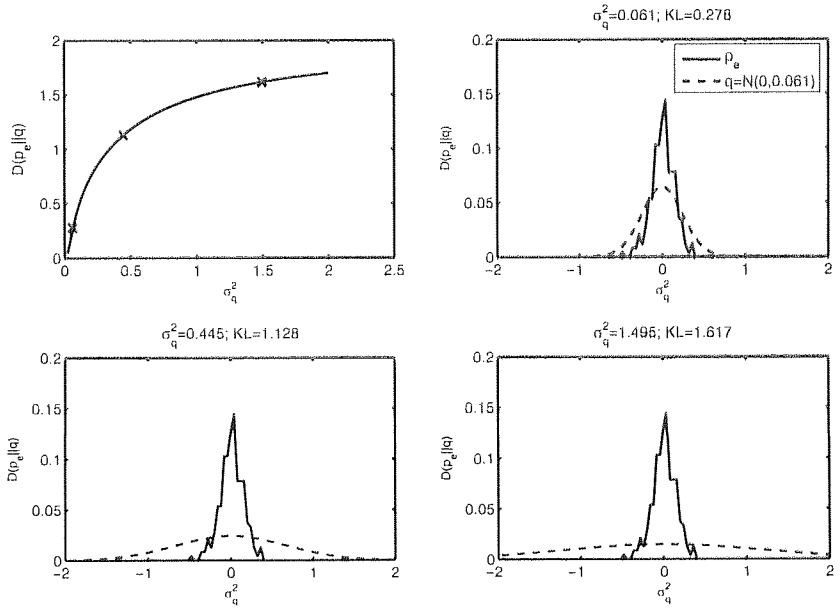

Figure 2.23: Computation of the Kullback-Leibler divergence between the distribution of the residual (referred to as p_e) on a one second-window during an non-epileptic event and a reference Normal distribution (q). The influence of the variance of q, σ_q^2, in the computation of the Kullback-Leibler divergence is investigated (top, left) for a small, intermediate and large values of σ_q^2 (top, right; bottom, left; and bottom, right respectively).

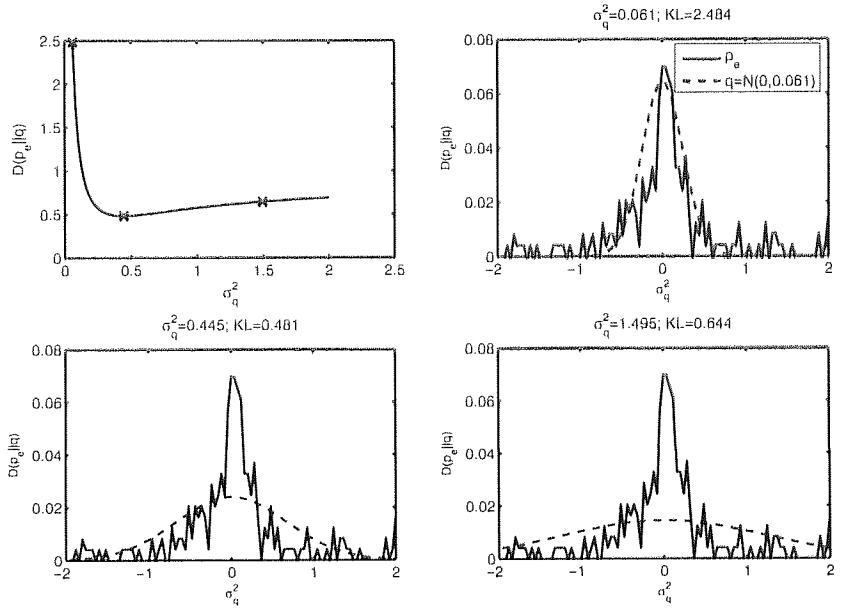

Figure 2.24: Computation of the Kullback-Leibler divergence between the distribution of the residual (referred to as p_e) on a one second-window during an epileptic event and a reference Normal distribution (q). The influence of the variance of q, σ_q^2, in the computation of the Kullback-Leibler divergence is investigated (top, left): when q is above p_e (small σ_q^2; top, right); when the distributions of q and p_e are close to each other ($\sigma_q^2 \approx \sigma_{p_e}^2$; bottom, left); when q is below p_e (large σ_q^2; bottom, right).

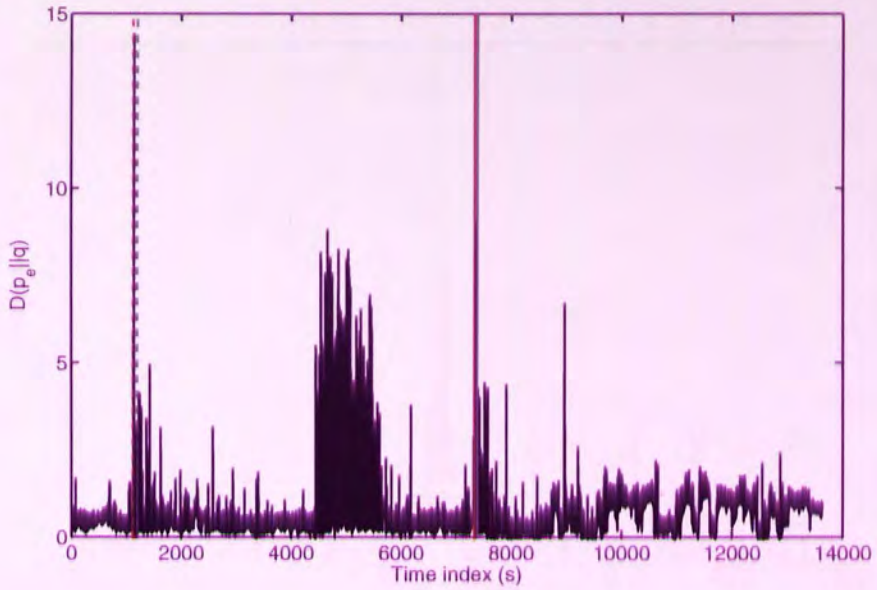

Figure 2.25: Kullback-Leibler divergence of a single channel of EEG (T3). The plain vertical red and green lines denote the start and end of an a priori labelled temporal lobe epileptic seizure. The draft vertical red and green lines denote the start and end of an a posteriori labelled temporal lobe epileptic seizure.

recording (3,407,500 samples) is plotted in Figure 2.25 (same recording as for the computation of the Shannon entropy and same legend). As can be observed from the behaviour of the Kullback-Leibler divergence on global and local scales (Figures 2.26 and 2.27), the measure, contrarily to the Shannon entropy, allows for the discrimination between ictal and interical epochs: if the KL-divergence were to be thresholded in order to be used as a binary decision support for ictal events detection, to achieve a sensitivity of 100% (desirable in biomedical applications), the threshold would have to be set at 4. Such a threshold would raise an alarm for genuine epileptic events but would also label the epoch starting at $t = 4450$s and finishing at $t = 5500$ as an ictal event. The same epoch, for which the EEG record is contaminated with chewing artifacts, was labelled as an ictal event by the Shannon entropy measure (2.2.2).

Despite its sensitivity to artifacts associated with partial epileptic events (such as the chewing artifacts in Figure 2.25), the Kullback-Leibler divergence allows for the discrimination between interictal and ictal epochs in an unambiguous way. If properly supported by a measure not sensitive to partial epileptic events,the Kullback-Leibler measure would successfully discriminate temporal lobe epileptic events.

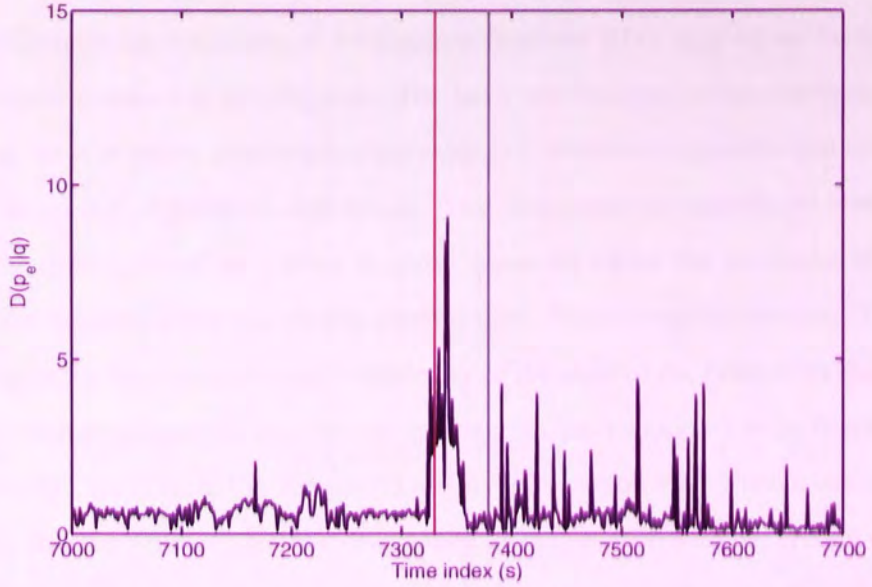

Figure 2.26: Detail of the Kullback-Leibler divergence of a single channel of EEG (T3) for the a priori labelled temporal lobe epileptic seizure. Note the dramatic increase in the value of the KL-divergence at the start of the ictal event.

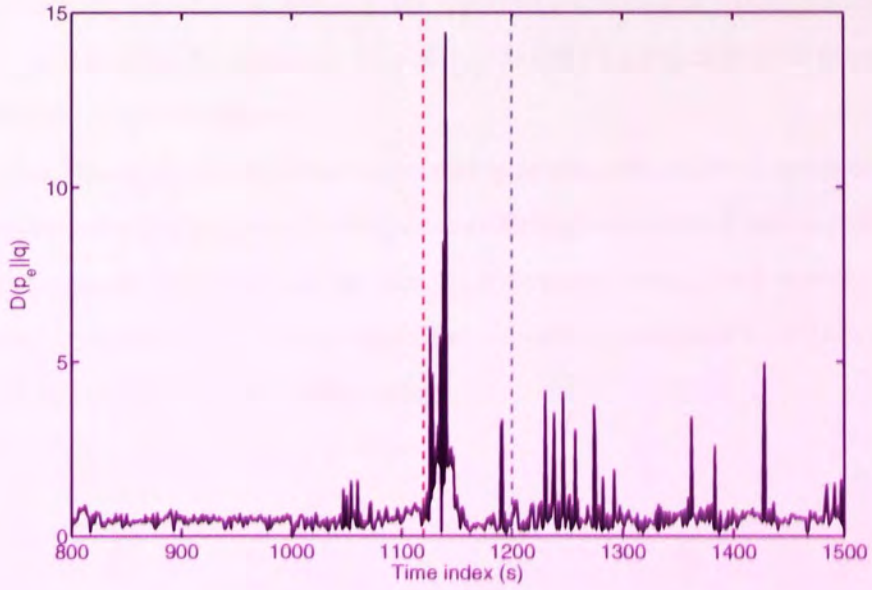

Figure 2.27: Detail of the Kullback-Leibler divergence of a single channel of EEG (T3) for the a posteriori labelled temporal lobe epileptic seizure. Note the dramatic increase in the value of the KL-divergence at the start of the ictal event.

2.3 Conclusions

In this Chapter the extraction of information from the EEG time series for the detection of epileptic events was investigated. The basic mechanisms of human epilepsy, with a focus at the ictal onset, motivated complexity as a measure of characterisation of the state of the brain with regards to ictal events. Two definitions of complexity were proposed: first, the dimension of the object in phase space on which the dynamics of the highly nonlinear system of low complexity evolve; then, the information content of the system. Consequently, the changes in the complexity of the state of the brain with regards to ictal events were monitored by a nonlinear measure (in accordance with the first definition of complexity), the correlation dimension, and by information theory measures, the Shannon entropy and the Kullback-Leibler divergence (in accordance with the second definition of complexity). The correlation dimension allows for the discrimination of ictal events from non-ictal events but fails as a measure for the estimation of the changes in the state of the brain integrated in an information fusion framework due to its time-intensive computation and its need for interpretation. The information measures are sensitive to the subtle changes in the complexity of the state of the brain estimated from the electroencephalographic signal, are not computing-intensive and are easy to interpret. However they are equally sensitive to artifacts: the information measures cannot be used as a decision support tool for the detection of ictal events since undesirable false positives corrupt the epileptic seizure diagnosis.

In this Thesis, due to the observation that temporal lobe epileptic seizures are coupled with heart arrhythmias (namely tachycardia) through the central autonomic network, it is next proposed to investigate the electrocardiogram during ictal events. In the next Chapter the characterisation of the heart function during temporal lobe epileptic events is investigated through the ECG time series.

3 Characterisation of cardiac arrhythmias during temporal lobe epileptic seizures

CONTENTS

A biomedical case for the coupling of the Brain and Heart systems during temporal lobe epileptic seizures, through the central autonomic network, was presented in Chapter 1. The novel approach described in this Thesis relies on the integration of information extracted from multimodal biomedical time series: ECG and EEG. The extraction of information from the EEG time series for the detection of epileptic events in a fusion-of-information framework was investigated in Chapter 2. The extraction of information from the ECG time series is the focus of the Chapter. The alterations of the cardiac rhythm during temporal lobe epileptic events has been documented in the clinical literature though no exploitation of this phenomenon on adults has been pursued until this Thesis. The brain structures and the mechanisms at the origin of the observation of heart arrhythmias during temporal lobe epileptic events are described in Section 3.1. A method for the description of heart rate variability is introduced and tested on real patient data in Section 3.2. The focus of the Chapter is the data interpretation of the arrhythmias observed during temporal lobe epileptic events from a probabilistic analysis perspective (Section 3.3) towards its integration in a fusion-of-information framework.

3.1 Principles of generation of heart arrhythmias during temporal lobe epileptic events

The biomedical case for the coupling of the Brain and Heart systems during temporal lobe epileptic seizures, through the central autonomic network, was presented in Chapter 1. The cardiovascular neurovegetative symptoms induced by temporal lobe epileptic events primarily consist of alterations of the cardiac rhythm: tachycardia (increase of the cardiac rhythm) and bradycardia (decrease of the cardiac rhythm). The principles of generation of heart arrhythmias during temporal lobe epileptic events are investigated in the next paragraph.

The role of epileptiform discharges localised to temporal lobe structures such as the amygdala or parts of the hippocampus in the induction of neurovegetative heart arrhythmias has been demonstrated on animal models. Applegate et al. (Applegate *et al.*, 1983) demonstrated that short latency bradycardia responses could be elicited by electrical stimulation of the amygdala central nucleus in awake rabbits: stimulation at eighteen of the twenty-five central nucleus sites elicited bradycardia responses, stimulation at one site

elicited a tachycardia response and stimulation at the the six remaining sites elicited no significant arrhythmia. Gelsema et al. (Gelsema *et al.*, 1993), relying on the experimental evidence of the role of the amygdala in the coordination of behavioural and autonomic responses to environmental stimuli, investigated the involvement of the bed nucleus of the stria terminalis (BST) and the sublenticular innominata (SI) in cardiovascular control in rats. The results of their investigations suggested the existence of a depressor area in regions of the BST and SI. Heart arrhytmias were observed from the stimulation of human insular cortex with evidence of the lateralisation of responses to stimulation site: Oppenheimer et al. (Oppenheimer *et al.*, 1992) concluded from seventy stimulations (thirty-nine right insular and thirty-one left insular; five patients) that on stimulation of the left insular cortex bradycardia and depressor responses were more frequently obtained than tachycardia and pressor effects whereas the converse applied for the right insular cortex. Kirchner et al. (Kirchner *et al.*, 2002) confirmed the right hemispheric lateralisation of sympathetic cardiac control in male patients (six male patients with unilateral-right temporal lobe epilepsy). Male and female patients with left temporal epileptic focus (five and four respectively) showed no significant changes in heart rate during epileptic seizures. Locatelli et al. (Locatelli *et al.*, 1999) conclude from a three case study and a literature review on fourteen patients that cardiac asystole or bradycardia is associated with left temporal lobe epileptic activity.

The clinical literature describes the principles generating heart arrhythmias during temporal lobe epileptic events. However the mechanisms responsible for the generation of opposed heart arrhythmias (tachycardia and bradycardia) are unknown: the systematic description of the nature of the heart arrhythmia induced by temporal lobe epileptic events cannot be achieved. The lateralisation of ictal events has been evoked as a potential explanation for the observation of opposed heart responses but the assumption is not supported by clinical studies. In this Thesis the data interpretation of the cardiac arrhythmias (tachycardia or bradycardia) observed during temporal lobe epileptic events is made from a probabilistic analysis perspective towards its integration in a fusion-of-information framework.

3.2 Characterisation of cardiac arrhythmias

The novel approach described in this Thesis relies on the integration of information extracted from multimodal biomedical time series towards epileptic events detection. The biomedical case for the coupling of the Brain and Heart systems during temporal lobe epileptic seizures, presented in Chapter 1, establishes that the cardiovascular neurovegetative symptoms induced by temporal lobe epileptic events primarily consist of alterations of the cardiac rhythm: tachycardia and bradycardia. Heart rate features and a method for their extraction from the ECG time series are presented in Section 3.2.1. An approach for the probabilistic analysis of cardiac arrhythmias from heart rate features is introduced and tested on real patient data in Section 3.3.

3.2.1 Heart rate feature extraction

The focus of the Chapter is on the extraction of information from the ECG times series for its integration in a fusion-of-information framework towards epileptic events detection. In this Thesis, following the assumption that temporal lobe epileptic events elicit cardiac fluctuations, the information extracted from the ECG time series is the evolution of the cardiac rhythm over time: the heart rate variability (HRV). The electrical activity within

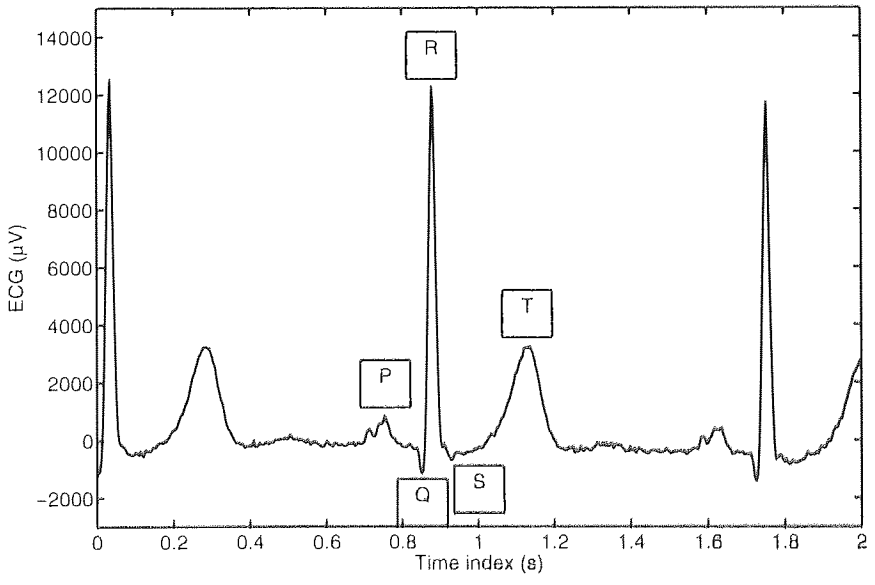

Figure 3.1: PQRST complex on a normal ECG.

the heart during the ventricular contraction appears as a characteristic waveform, the QRS complex, on the ECG (Figure 3.1). The R peak in particular is used for the automated determination of the heart rate due to its relatively easy extraction from the ECG time series.

Methods of automatic detection of peaks or complexes from the ECG waveform rely on a two-steps analysis: a preprocessing or feature extraction stage; and a detection and decision stage. In the next paragraphs we present a method for the extraction of R peaks from the ECG time series by density estimation of the R peaks.

Feature extraction from the ECG time series

Derivative-based algorithms, such as the one used in this Thesis, use the characteristic steep slope of the QRS complex to lifter the ECG waveform:

$$\mathbf{y}_1(t) = \mathbf{x}(t) - \mathbf{x}(t-1) \tag{3.1}$$

$$\mathbf{y}_2(t) = \mathbf{y}_1^2(t), \tag{3.2}$$

with $\mathbf{x}(t)$ the ECG time series and $t = 1, \ldots, T$. R peaks locations are estimated from the index of the maximum of the signal $\mathbf{y}_2$ for each epoch where the signal $\mathbf{y}_2$ is greater than an amplitude threshold Θ (Figure 3.2). At this stage of the feature extraction of the ECG time series two misdetected R peaks surrounding a genuine R peak (represented as red lozenges $\Diamond$ in Figure 3.2) are extracted as R peak candidates.

At the preprocessing stage the validity of the detected R peak candidates is not assessed. It is assessed in a probabilistic framework at the next stage of the analysis: the decision stage.

Decision logic

The probability $p(\mathbf{x})$ of a feature vector $\mathbf{x} = \mathbf{x}(t)$ extracted from the ECG waveform at time t is estimated by a mixture model $\hat{p}(\mathbf{x}) = \sum_{j=1}^{4} P(j)p(\mathbf{x}|j)$. In this Thesis $\mathbf{x}$ is chosen to be a PCA-reduced version (Figure 3.5) of the 95 sample points of the QRS complex centered around the R peak candidates detected in the preprocessing stage of the analysis (Figure 3.3); the basis functions of the mixture model, $p(\mathbf{x}|j)$, are Gaussian components with diagonal covariance matrix $\Sigma_j = \mathrm{diag}(\sigma_{j,1}^2, \ldots, \sigma_{j,d}^2)$, $d = 3$:

$$p(\mathbf{x}|j) = \frac{1}{(2\pi \prod_{i=1}^{d} \sigma_{j,i}^2)^{d/2}} \exp\left\{ -\sum_{i=1}^{d} \frac{(x_i - \mu_{j,i})^2}{2\sigma_{j,i}^2} \right\}. \tag{3.3}$$

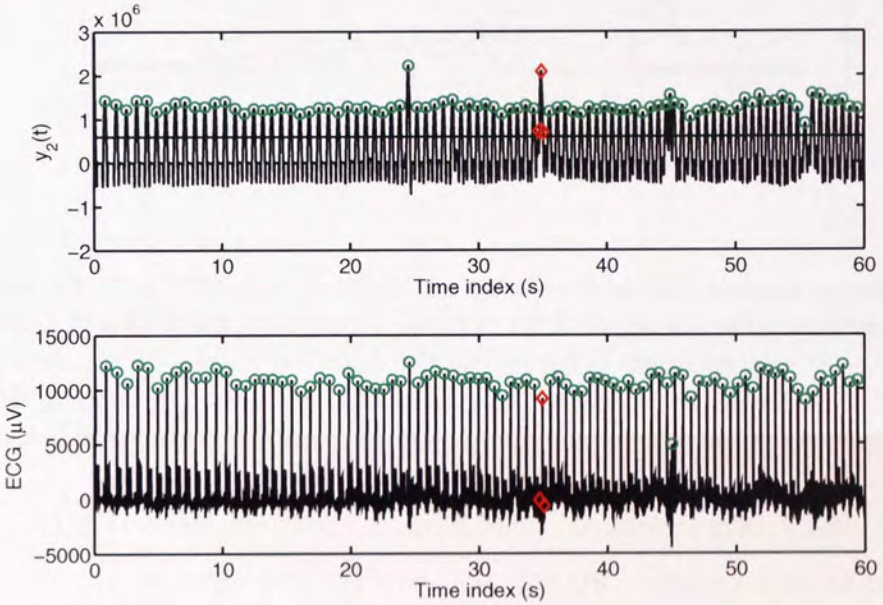

Figure 3.2: Feature extraction from the ECG time series on a 60 seconds epoch. Upper plot: The potential R peaks locations are estimated from the index of the maximum of the signal $\mathbf{y}_2$ (Equation 3.2) for each epoch where the signal $\mathbf{y}_2$ is greater than an amplitude threshold Θ (horizontal line). Lower plot: The potential R peaks locations are superimposed to original ECG time series. Note the two misdetected R peaks surrounding a genuine R peak (◊).

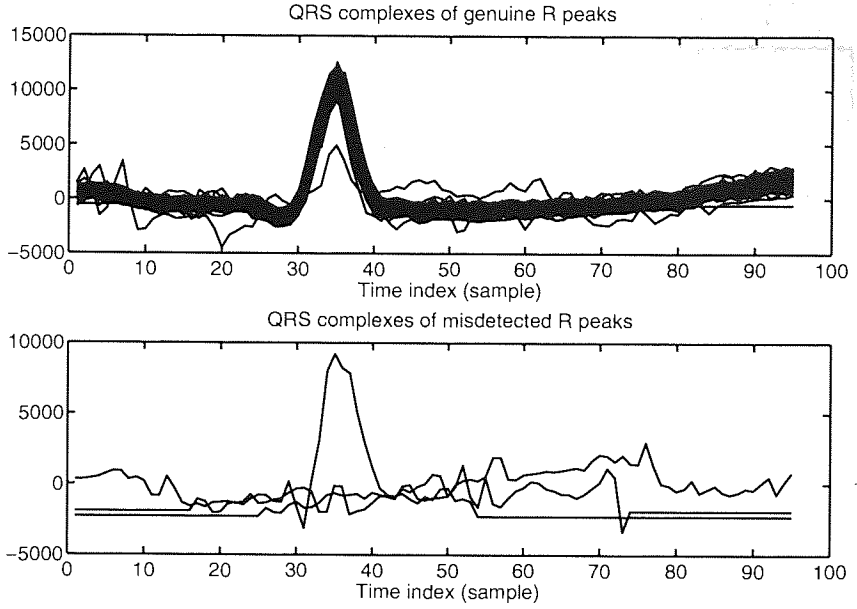

Figure 3.3: The QRS complexes of the genuine R peaks (denoted as green circles in Figure 3.2) are plotted in the upper plot. The QRS complexes of the misdetected R peaks (denoted as red lozenges in Figure 3.2) are plotted in the lower plot. The QRS complex of the genuine R peak whose QRS complex is overlapped by misdetected R peaks is truncated in the lower plot.

The QRS complexes of the genuine R peaks (denoted as green circles in Figure 3.2) are plotted in the upper plot of Figure 3.3. The QRS complexes of the misdetected R peaks (denoted as red lozenges in Figure 3.2) are plotted in the lower plot. Since two misdetected R peaks overlap the QRS complex of the genuine R peak, the QRS complex of the latter is truncated in the lower plot.

Three principal components (Figure 3.4) with three eigenvalues accounting for 84.32% of the data are retained to reduce the dimensionality of the QRS complex candidates extracted from the ECG waveform. The projection of the 95 sample points of the QRS complex candidates are plotted in Figure 3.5. The misdetected R peaks overlapping a genuine R peak, represented as red lozenges ($\Diamond$), are outliers of the cluster of genuine R peaks.

The Gaussian mixture model (Equation 3.3) is initially trained on a 60 seconds subset of the ECG waveform. The feature extraction of R peaks from the ECG time series and the estimation of the probability $\hat{p}(\mathbf{x})$ of the PCA-reduced version of the QRS complex candidates is then performed on the whole ECG recording. A non-patient dependent a priori

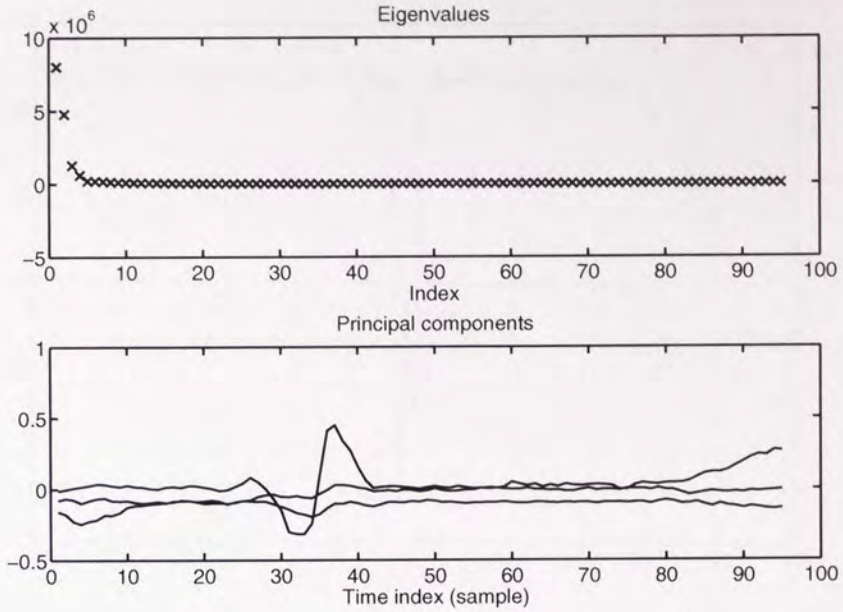

Figure 3.4: The eigenvalues of the mixing matrix are plotted in the upper plot. Three eigenvalues, accounting for 84.32% of the data, are retained. The three corresponding principal components are shown in the lower plot.

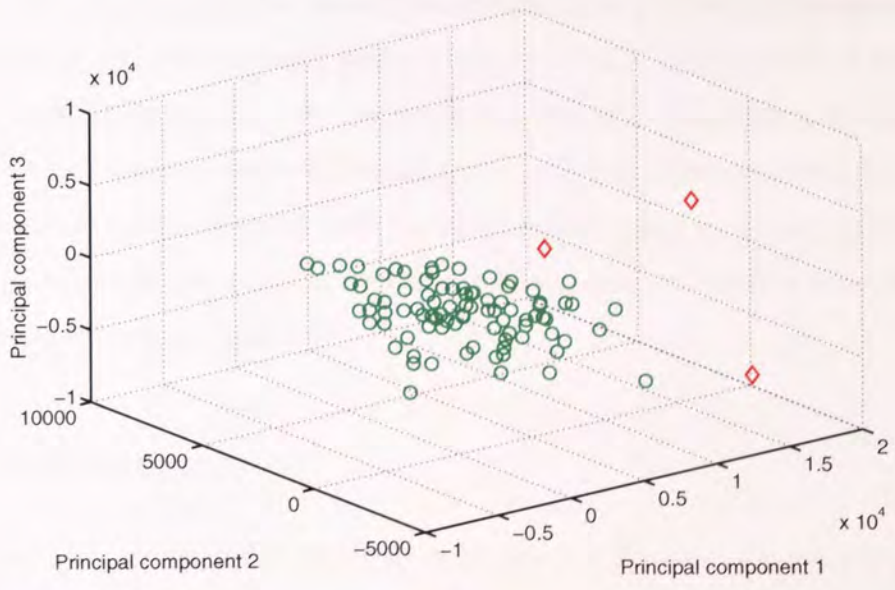

Figure 3.5: PCA-reduced version of QRS complexes centered around R peak candidates. The 95 sample points of the QRS complexes centered around the R peak candidates are projected on the three first principal components (Figure 3.4, lower plot). Note that the two misdetected R peaks surrounding a genuine R peak, represented as red lozenges (◊), are outliers of the cluster of genuine R peaks.

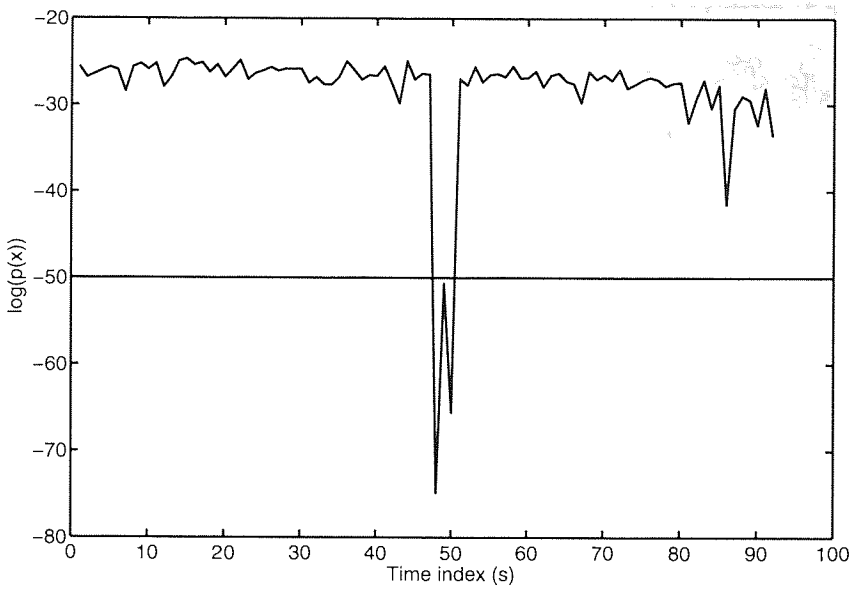

Figure 3.6: Logarithm of the estimated probability $\hat{p}(\mathbf{x})$ of a feature vector $\mathbf{x} = \mathbf{x}(t)$ extracted from the ECG waveform at time t. A threshold set at -50 (horizontal line) discriminates the misdetected R peaks (and the genuine R peak overlapped) from the genuine R peaks.

threshold is finally applied to the estimated probabilities $\hat{p}(\mathbf{x})$ to discriminate the genuine R peaks from the misdetected R peaks (Figures 3.6 and 3.7). The choice of the threshold is not sensitive. In Figure 3.7 the genuine R peak and the overlapping misdetected R peaks have been discarded from the initial extraction of R peaks: the automated detection of R peaks misses genuine R peaks when the latter are overlapped by misdetected R peaks.

The heart rate variability is estimated from the series of the time intervals between consecutive detected R peaks.

3.3 R-R intervals

R-R intervals are derived from the series of detected R peaks. Figures 3.8 and 3.9 are plots of the duration between detected consecutive R peaks (or R-R intervals) around the a priori- and a posteriori-labelled epileptic seizures: the duration of R-R intervals dramatically decreases towards and during the epileptic events.

The start and end of the a priori-labelled epileptic event have been derived from the observation of the EEG recording by two clinicians who agreed on the start and end of

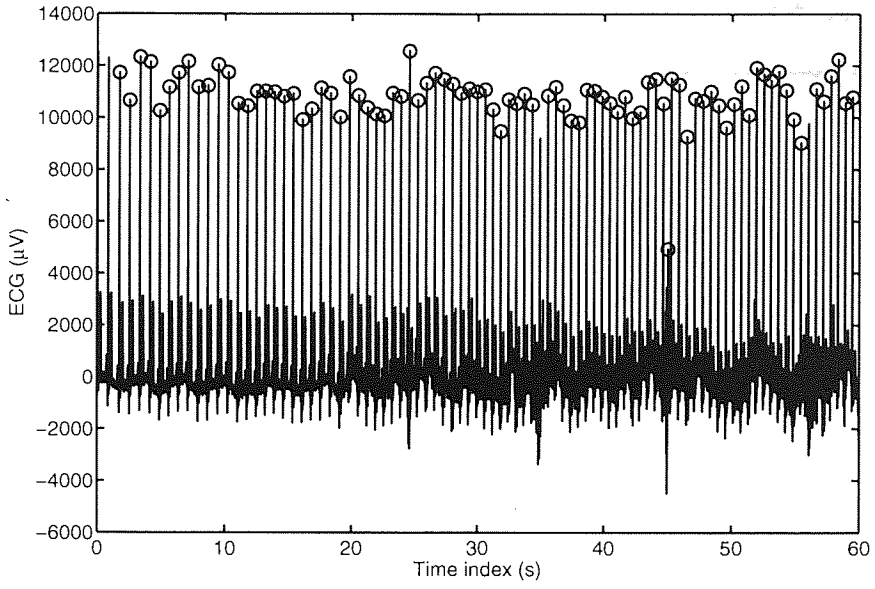

Figure 3.7: R peaks extracted from the ECG waveform. The genuine R peak and the overlapping misdetected R peaks have been discarded from the initial extraction of R peaks.

the event. In Figure 3.8 the increase of the heart rhythm is observed before the start of the temporal lobe epileptic seizure. The a posteriori-labelled epileptic seizure was confirmed and annotated by a clinician from the observation of the EEG recording. The heart arrhythmia (namely tachycardia) starts at the same time as the temporal lobe epileptic event (Figure 3.9). The observation of the increase of the heart rhythm prior to the ictal event in Figure 3.8 allows the possibility of the heart rhythm being used as a prediction (on the scale of a few seconds) of temporal lobe epileptic events. However the hypothesis is negated by the observation of the increase of the heart rhythm simultaneously to the start of the a posteriori labelled ictal event (Figure 3.9).

The focus of the Chapter is the data interpretation of the arrhythmias observed during temporal lobe epileptic events from a probabilistic analysis perspective towards its integration in a fusion-of-information framework. The estimation of the distribution of R-R intervals is introduced in Section 3.3.1; the density modelling of heart arrhythmias is introduced in Section 3.3.2.

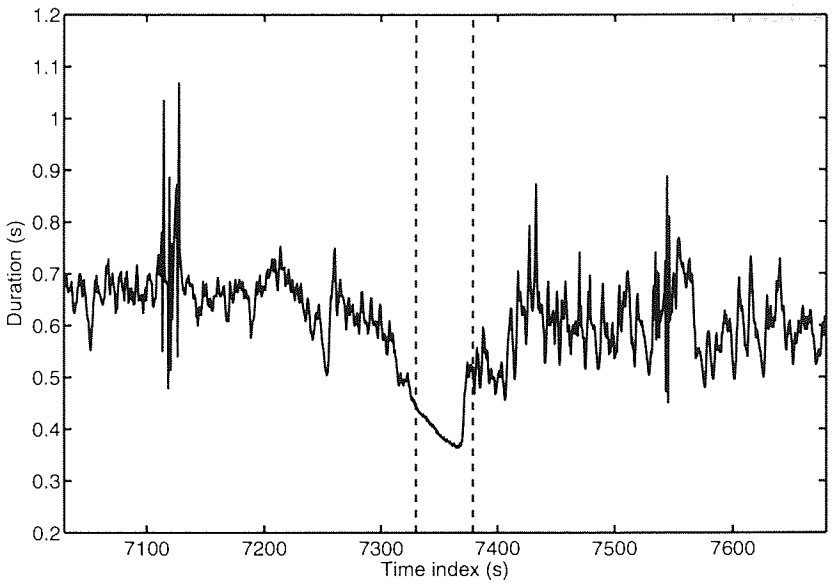

Figure 3.8: Heart arrhythmia during the a priori labelled ictal event. The heart rhythm increases before the start of the ictal event.

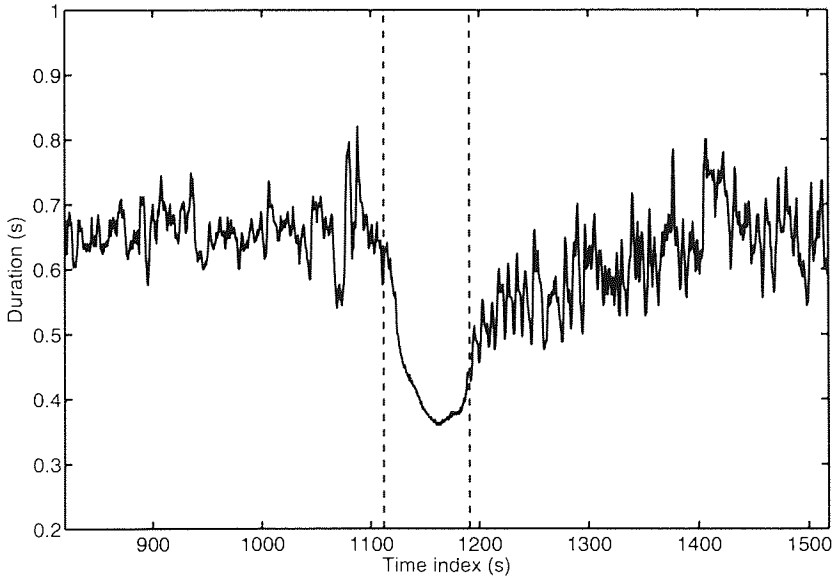

Figure 3.9: Heart arrhythmia during the a posteriori labelled ictal event. The heart rhythm increases simultaneously to the start of the ictal event.

3.3.1 Distribution of R-R intervals

In order to obtain a probabilistic description of the heart rhythm during interictal and ictal epochs, we assume that the difference between the time occurrence of the R peaks is a stationary random process which needs to be estimated. The stationarity assumption is reasonable from a physiological perspective since typical heart rates fluctuate around a mean for uniform periods of activity. In this Thesis, for simplicity, the difference between the time occurrence of the R peaks on successive five second windows with no overlap is assumed to be a Gaussian random variable whose (stationary) parameters (μ,σ^2) are estimated by a maximum likelihood approach:

$$\begin{aligned} \hat{\mu} &= \frac{1}{N}\sum_{n=1}^{N} x^n \\ \hat{\Sigma} &= \frac{1}{N}\sum_{n=1}^{N} (x_n - \hat{\mu})(x_n - \hat{\mu})^{\mathrm{T}}, \end{aligned}$$

with x^n the interval between two consecutive R peaks. In this manner the temporally complex data stream is reduced to a simple pattern of activity of two random variables. If this pattern departs from the stationary assumption we assume the state-changing driver is the temporal lobe epileptic seizure feedback.

Figures 3.10 and 3.11 are plots of the maximum likelihood-estimated parameters of the Gaussian distributions of R-R intervals on five second windows with no overlap extracted from the ECG of the reference patient suffering from temporal lobe epileptic seizure, recorded at the same time as the electroencephalogram. As previously mentioned, the reference patient suffered a priori- and a posteriori-labelled temporal lobe epileptic seizures. In both Figures:

- the parameters of the distributions of R-R intervals on five second windows with no overlap during the nominal activity of the brain are plotted as green circles (○),
- the succession of values taken by the parameters during the a priori- and a posteriori-labelled temporal lobe epileptic events are traced as trajectories of red lozenges (◊) or squares (□), respectively,
- the start and end of the epileptic events are marked by black triangles pointing towards the left (◁) and the right (▷), respectively,
- the blue lozenges (◊) or squares (□) denote the values taken by the parameters

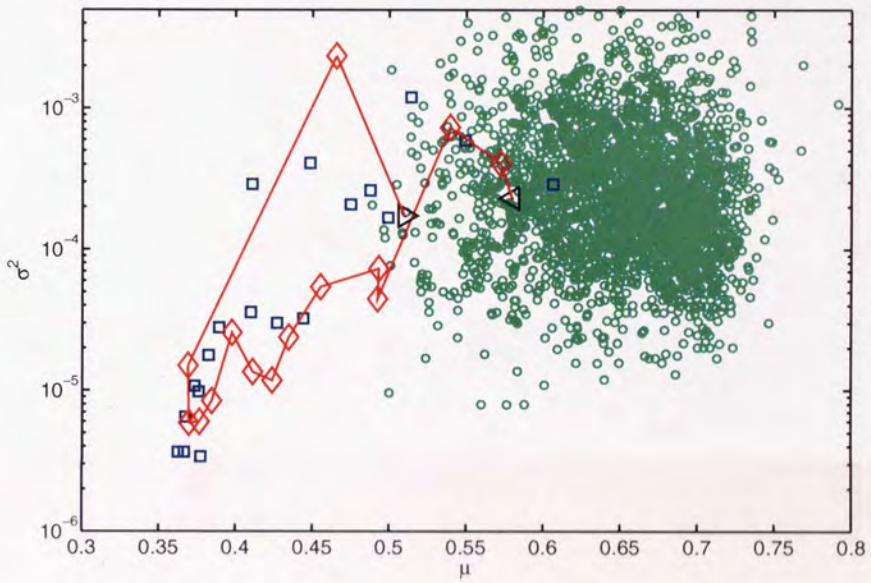

Figure 3.10: Plot of the parameters of the distributions of R-R intervals on five seconds windows with no overlap. The green circles (○) denote the values of the parameters during the nominal activity of the brain. The trajectory of red lozenges (◊) denotes the succession of values taken during the a priori-labelled temporal lobe epileptic seizure (start: ◁; end: ▷). The blue squares (□) denote the values taken during the a posteriori-labelled temporal lobe epileptic event. We observe a decrease of the mean and variance of the distribution of R-R intervals from the start of the temporal lobe epileptic event before the values of the parameters get back to the cluster of nominal activity towards the end of the epileptic event.

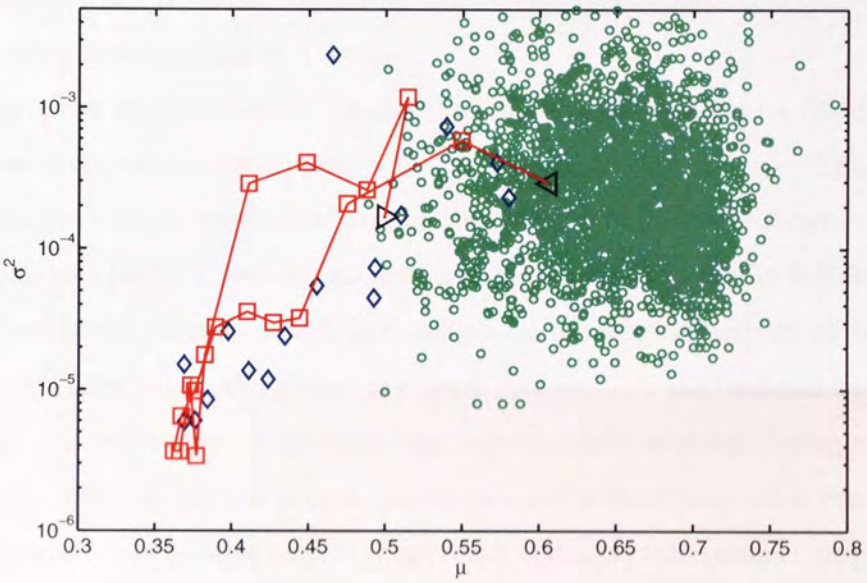

Figure 3.11: Plot of the parameters of the distributions of R-R intervals on five seconds windows with no overlap. The trajectory of red squares (□) denotes the succession of values taken during the a posteriori-labelled temporal lobe epileptic seizure (start: ◁; end: ▷). The blue lozenges (◊) denote the values taken during the a priori-labelled temporal lobe epileptic event.

during the a priori- and a posteriori-labelled temporal lobe epileptic events, respectively, plotted for record.

The a posteriori-labelled epileptic seizure was discovered from the observation of the values of the parameters of the distributions of the R-R intervals on five second windows with no overlap: the second trajectory of lower mean and variance when compared to the nominal activity was identified and a clinician was asked to interpret the corresponding EEG epoch. The latter was identified as a fully-developed temporal lobe epileptic seizure. This successful use of the process to allow prospective analysis leading to the identification of a previously unlabelled seizure supports the basic approach to ECG characterisation introduced in the Thesis.

The mean and variance of the distributions of R-R intervals on five seconds windows with no overlap during temporal lobe epileptic events decrease. This observation is consistent with the biomedical case for the coupling of the Brain-Heart systems during temporal lobe epileptic events: tachycardia is characterised by shorter R-R intervals when compared to the duration of R-R intervals during the nominal activity of the heart. The two tachycardia trajectories plotted in Figures 3.10 and 3.11 start and end with the temporal lobe epileptic events. Tachycardia was systematically observed during temporal lobe epileptic events on the real patient recordings used in the Thesis while bradycardia was never observed. In the next Section an approach to density estimation of heart arrhythmias is introduced. The approach is demonstrated for the density estimation of tachycardia.

3.3.2 Density estimation of heart arrhythmias

In order to perform the automatic detection of temporal lobe epileptic events using the heart rhythm, a Gaussian mixture model (GMM) was employed to model the probability of tachycardia given the features extracted from the ECG time series (i.e. mean and variance of the distribution of R-R intervals on five seconds windows).

The dataset of parameters of the distributions of the R-R intervals was partitioned into three classes: the tachycardia class, the class of nominal activity and the class of outliers. In a classification problem we are interested in the estimation of the posterior probabilities of class-membership given a measurement: $P(C_k|\mathrm{x})$. In the application considered, the measurement is the vector of the parameters of the distributions of R-R intervals: $\mathbf{x} = \mathrm{F}_{\mathrm{ECG}} = (\mu, \sigma^2)$. By fitting and training (on data of each class only) a mixture of Gaussians

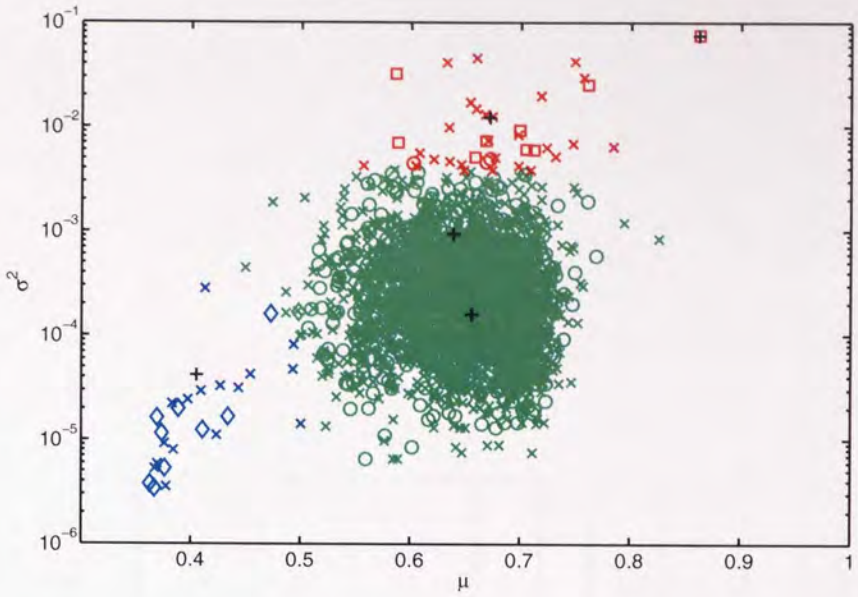

Figure 3.12: Classification of the features extracted from the ECG time series $\mathbf{F}_{\mathrm{ECG}}$ in one of the three following classes: tachycardia (blue), nominal activity (green) or outliers (red), using Gaussian mixture models for density estimation. The training set is represented as follows: lozenges ($\Diamond$), circles ($\circ$) or squares ($\Box$) for the tachycardia-, nominal activity- and outlier classes, respectively. The rest of the data, excluding the training dataset, is represented as crosses ($\times$). We observe that the tachycardia trajectories presented in Figures 3.10 and 3.11 are correctly classified.

to each class, the densities $p(\mathbf{x}|C_k)$ can be estimated. Using Bayes' theorem we can recover the required conditional probabilities:

$$P(C_k|\mathrm{x}) = \frac{p(\mathrm{x}|C_k)P(C_k)}{p(\mathrm{x})}, \tag{3.4}$$

with $p(\mathrm{x}) = \sum_{k=1}^{c} p(\mathrm{x}|C_k)P(C_k)$ and the prior probabilities $P(C_k)$ estimated from a subset of the dataset. We estimate the posterior probabilities of class-membership given a measurement. The posterior probability of interest is the posterior probability of tachycardia given the features extracted from the ECG time series: $P(C_T|\mathbf{F}_{\mathrm{ECG}})$.

Figure 3.12 is the plot of the decisions based on the classification of the features extracted from the ECG time series into one of the three classes: tachycardia, nominal activity, outliers. Each mixture was trained on a third of the data available. The training data is represented on the Figure as lozenges ($\Diamond$), circles ($\circ$) or squares ($\Box$) for the tachycardia-, nominal activity- and outlier classes, respectively. The rest of the data, excluding the training dataset, is represented as crosses ($\times$). A measurement $\mathbf{F}_{\mathrm{ECG}}$ was attributed to class C_k provided $P(C_k|\mathbf{F}_{\mathrm{ECG}})$ was greater than the posterior probabilities of

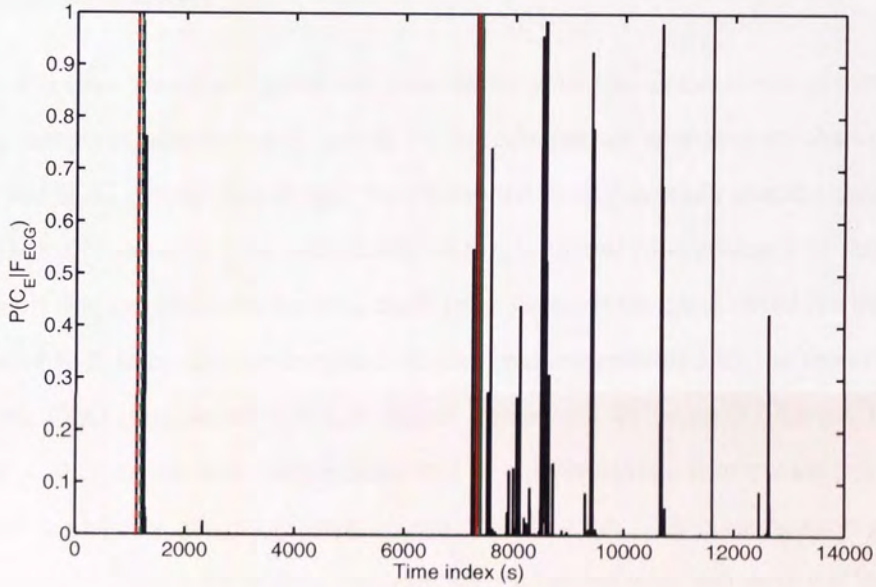

Figure 3.13: Posterior probability of tachycardia given the features extracted from the ECG time series: $P(C_T|\mathbf{F}_{\mathrm{ECG}})$. We observe that the tachycardia trajectories presented in Figures 3.10 and 3.11 are correctly classified: the tachycardia events coincide with the temporal lobe epileptic events (plotted as vertical lines). Times when $P(C_T|\mathbf{F}_{\mathrm{ECG}})$ is close to 1 coincide with non-epileptic tachycardia events.

class-membership of $\mathbf{F}_{ECG}$ to the remaining two classes. The classification of the features extracted from the ECG time series is represented in Figure 3.12 by the following color scheme: blue for the tachycardia class, green for the nominal activity class and red for the outliers class. The posterior probability of class-membership to the tachycardia class given the features extracted from the ECG time series is plotted in Figure 3.13.

Figure 3.12 shows that the decisions based on classifying by the suggested approach is consistent with the known ground truth.

3.4 Conclusion

In this Chapter we investigated the manifestation of the Brain-Heart systems coupling during temporal lobe epileptic events by introducing an approach to characterise ECG using real ECG patient recordings. We concluded from this study that the patients studied systematically suffered from tachycardia during temporal lobe epileptic seizures. In order to exploit this information, we used an R peak detector which allowed for the characterisation of R-R intervals. To integrate the information provided by the features extracted from the ECG time series in a data fusion framework in the next Chapter, the distribution of R-R intervals was further described in a probabilistic framework using Gaussian mixture models for density estimation and classification. The classification performance of the tachycardia events proved accurate and coincided with the temporal lobe epileptic events observed from the simultaneously recorded EEG.

Considerations on the suitability of the information extracted from the ECG time series towards temporal lobe epileptic seizure detection will be given in Chapter 4. Schemes for the combination of information provided by the heterogenous modalities of data, ECG and EEG, will also be introduced and investigated in the next Chapter.

4 Information fusion for epileptic event detection

CONTENTS

NOTATION

$$C \; - \; \text{condition status} = \begin{cases} 0 & \text{not affected by the condition} \\ 1 & \text{affected by the condition} \end{cases}$$

$C, \overline{C}$ – subscripts for presence and absence of the condition

ρ – prevalence of the condition : $P(C = 1)$

$\oplus$ – combination operator

In the previous Chapters the EEG and ECG time series have been used to construct independent models towards unsupervised epileptic seizure detection. The limitations of the unimodal measurement approaches have been demonstrated: in the case of the EEG time series, the unequivocal detection of epileptic events is difficult to achieve due to the sensitivity of the measure of complexity of the state of the brain not only to epileptic events but also to artifacts leading to undesirable false positives; in the case of the ECG time series, the unequivocal detection of epileptic events is unreliable since the ECG time series is not the primary tool for monitoring the state of the brain with regards to epileptic events detection. Nevertheless a case for biomedical data fusion has been introduced in Chapter 1 motivating the fusion of EEG and ECG time series towards temporal lobe epileptic seizure detection. The levels at which the data fusion can be performed are detailed in Section 4.1. The performance of the data fusion approaches to be compared to the performance of the unimodal approaches on long-records of patient data are shown in Section 4.2. Finally, concluding considerations are presented in Section 4.3.

4.1 Schemes for fusion of biomedical data

In a biomedical framework the raw output of a monitoring device (referred to as a "sensor" in the rest of the Chapter) consists of a recording such as a biomedical time series (e.g. EEG or ECG) or imaging instance (e.g. functional magnetic resonance imaging (fMRI) or X-ray). In clinical practice clinicians extract relevant information ("features") from raw recordings to produce a decision ("diagnosis") according to a certain degree of belief in the occurrence of a condition or a phenomenon. The decision can be inferred through the observation of one or more modalities of information. The way to combine such modalities ("biomedical data fusion") relies on:

- the nature of the sources of information (e.g. biomedical time series, imaging instance),
- the characteristics of the sources of information (e.g. sampling rate, time resolution, spatial resolution),
- the level at which to combine modalities.

This Section is dedicated to the investigation of the different levels at which to perform the biomedical data fusion (from low- to high-level: sensors/observations, features, degrees of belief/probabilities, decisions and models). An analogy to clinical practice is drawn in order to show the equivalent of biomedical fusion methods in real-world practice.

4.1.1 Fusion at the level of observations

In the fusion-of-observations scheme at the sensor level all the raw information (no data reduction is performed) is transmitted up the fusion hierarchy to a common central fusion cell (Figure 4.1): the fusion is optimal with respect to information integrity but impractical due to the variability and redundancy of biomedical information. Hence each sensor provides its full observation vector (denoted as $\mathbf{x}_i(t), i = 1, \ldots, N$ in Figure 4.1) to a central forecaster whose output is a combined decision vector ("degree of belief") on the basis of which a decision maker decides a course of action.

From a medical perspective such a scheme is equivalent to the collection and interpretation of all raw data available for a particular patient by a unique multidisciplinary clinician who will issue a diagnosis.

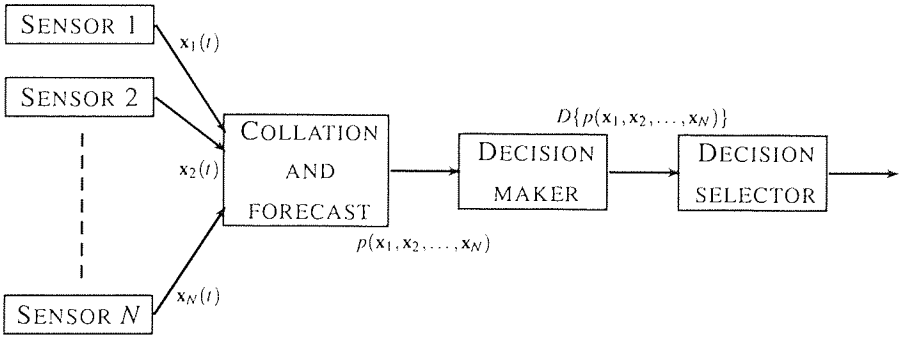

Figure 4.1: Fusion of observations scheme.

4.1.2 Fusion at the level of features

In the fusion-of-features scheme, data reduction is performed by extracting relevant features $\mathbf{F}(\mathbf{x}_i(t)), i = 1,\ldots,N$ from the state vectors $\mathbf{x}_i(t), i = 1,\ldots,N$ from sensors (Figure 4.2): the state vectors are reduced to feature vectors of lower data rate transmitted up the hierarchy. The redundancy of biomedical data is considerably reduced since the analysis is focused on the observation of markers of interest, making the approach more practical than the previous fusion scheme.

From a medical perspective such a scheme is equivalent to the collection, observation and interpretation of markers, features and tests for a particular patient by a unique multidisciplinary clinician who will issue a diagnosis.

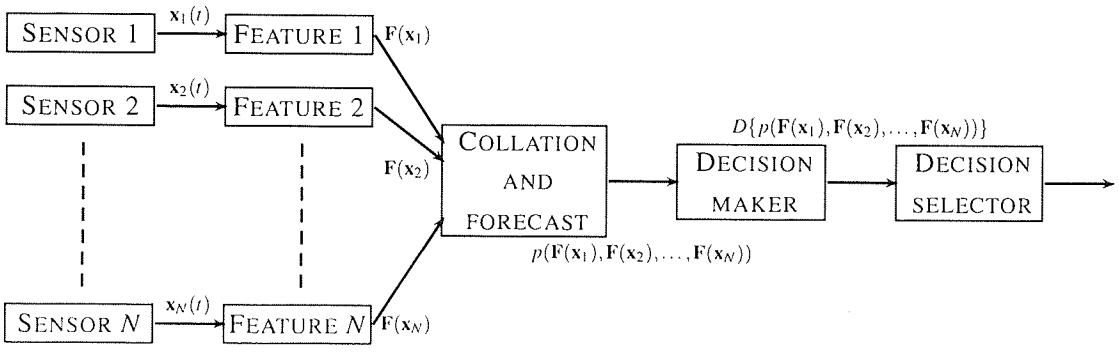

Figure 4.2: Fusion of features scheme, equivalent to an expert multidisciplinary clinician.

4.1.3 Fusion at the level of probabilities

In the fusion-of-probabilities scheme (Figure 4.3) the information is gradually reduced as it progresses up the hierarchy. The feature vectors $\mathbf{F}(\mathbf{x}_i(t)), i = 1,\ldots,N$ provided by each sensor are reduced to probability vectors of possibility $p(\mathbf{F}(\mathbf{x}_i(t))), i = 1,\ldots,N$ which are fused and transmitted to a central decision cell.

This scheme can be interpreted as a group of local experts providing a soft decision based on the raw data available to them, to a grand expert who has to decide the way to combine the evidence collected and to issue a diagnosis.

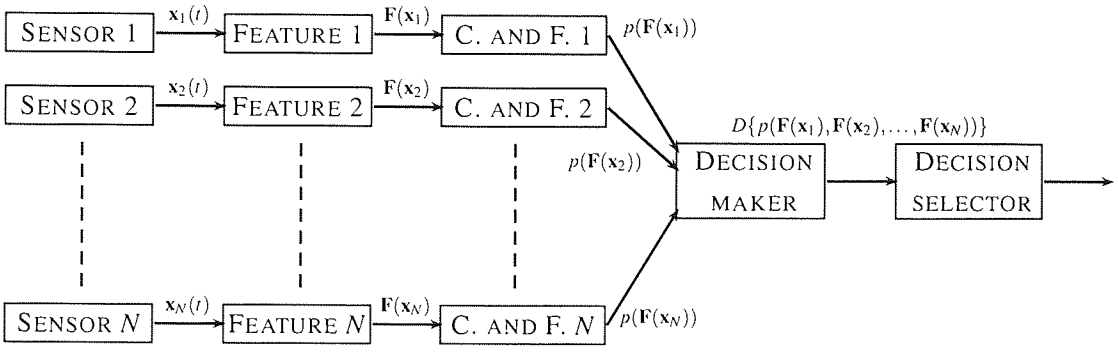

Figure 4.3: Fusion of probabilities scheme, equivalent to a set of local experts providing a soft decision based on the raw data available to them, to a grand expert who has to decide the way to combine the evidence collected to issue a diagnosis. C. AND F.: Collation and forecast.

4.1.4 Fusion at the level of decisions

In the fusion-of-decisions scheme (Figure 4.4) each sensor is dealt with independently: each observation vector is mapped to a probability vector $p(\mathbf{F}(\mathbf{x}_i(t))), i = 1,\ldots,N$ upon which a decision $D\{p(\mathbf{F}(\mathbf{x}_i(t))), i = 1,\ldots,N\}$ will be derived from an individual decision maker. The partial decisions are then combined by a global decision maker D. In this approach the data is reduced on a channel-by-channel basis: no recourse to global, cross-channel information is performed.

The medical interpretation of this scheme is that of local experts giving a hard, uncompromising decision to a Grand Clinician who will combine them to issue his final verdict.

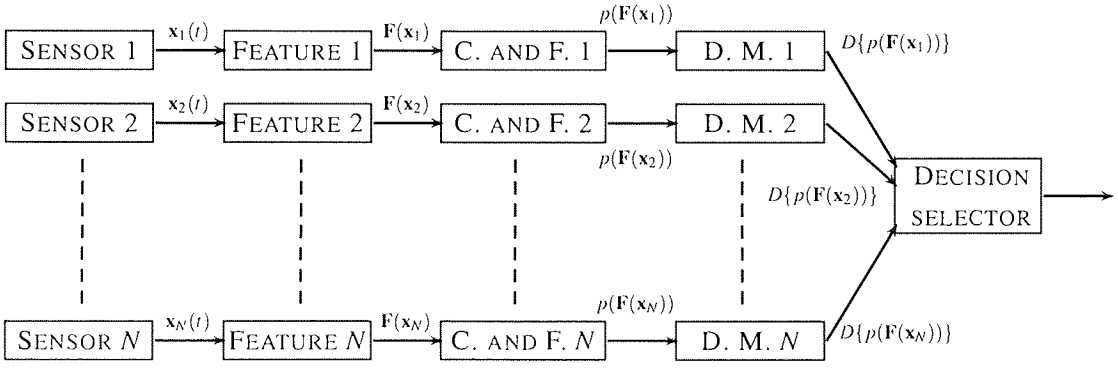

Figure 4.4: Fusion of decisions scheme, equivalent to local very confident clinicians passing their hard decisions to a Grand Clinician. C. AND F.: Collation and forecast; D. M.: Decision maker.

4.1.5 Fusion at the level of models

The fusion-of-models scheme is not a level of the data fusion architecture but can be performed at any level. Its aim is to reduce the estimation errors produced by models unable to perfectly fit the underlying "true" phenomenon by combining them. The fusion of models always guarantees to perform at least equally well as any single model on average over a representative data set: for a given input biomedical vector $\mathbf{x}$, let each one of the M possible models produce an estimate $y_i(\mathbf{x}), i = 1,\ldots,M$ of an underlying "true" (unknown) function $h(\mathbf{x})$. Each model prediction can be considered to be the true function plus an error, $y_i = h + \varepsilon_i$. The average sum of squares error for each model is thus $E_i = \mathrm{E}[\varepsilon_l]^2$ where $\mathrm{E}[\ldots]$ represents the expectation and corresponds to an average over the input space, $\mathbf{x}$. So, the average error made by the collection of models which operate individually is given by

$$E_{av} = \frac{1}{M}\sum_{i=1}^{M}\mathrm{E}\left[\varepsilon_i^2\right].$$

Now if we consider a simple committee in which we combine the predictions of each model or expert, so the predicted value of the underlying function is just

$$y_{committee} = \frac{1}{M}\sum_{i=1}^{M} y_i(\mathbf{x}), \tag{4.1}$$

the error about this committee prediction is just

$$\begin{aligned} E_{committee} &= \mathrm{E}\left[\left(\frac{1}{M}\sum_{i=1}^{M} y_i(\mathbf{x}) - h(\mathbf{x})\right)^2\right] \\ &= \mathrm{E}\left[\left(\frac{1}{M}\sum_{i=1}^{M}\varepsilon_i\right)^2\right]. \end{aligned} \tag{4.2}$$

In the case of correlated errors (Perrone, 1994), $\mathrm{E}\left[\varepsilon_i\varepsilon_j\right] \neq 0, (i \neq j)$, we find from the Cauchy inequality,

$$\left(\sum_{i=1}^{M}\varepsilon_i\nu_i\right)^2 \leq \left(\sum_{i=1}^{M}\varepsilon_i^2\right)\left(\sum_{i=1}^{M}\nu_i^2\right),$$

setting $\nu_i = 1, \forall i$,

$$\left(\sum_{i=1}^{M}\varepsilon_i\right)^2 \leq M\sum_{i=1}^{M}\varepsilon_i^2.$$

Averaging over the data gives

$$\begin{aligned} \frac{1}{M}\mathrm{E}\left[\left(\sum_{i=1}^{M}\varepsilon_i\right)^2\right] &\leq \frac{1}{M}\mathrm{E}\left[M\sum_{i=1}^{M}\varepsilon_i^2\right], \\ E_{committee} &\leq E_{av}. \end{aligned} \tag{4.3}$$

Designing a fusion scheme in which the committee members whose predictions are "better" would be assigned a heavier weight would always generate a regression error as low or lower than the committee error (Perrone & Cooper, 1994). Let $E_{w\ committee}$ be the average weighted committe error

$$\begin{aligned} E_{w\ committee} &= \mathrm{E}\left[\left(\sum_{i=1}^{M}\alpha_i y_i(\mathbf{x}) - h(\mathbf{x})\right)^2\right] \\ &= \mathrm{E}\left[\left(\sum_{i=1}^{M}\alpha_i \varepsilon_i\right)^2\right], \end{aligned}$$

under the constraint $\sum_{i=1}^{M}\alpha_i = 1$. It follows that minimising $E_{w\ committee}$ reduces to minimising $\sum_{i=1}^{M}\sum_{j=1}^{M}\alpha_i\alpha_j C_{ij}$ where $\mathbf{C}$ is the covariance matrix between the model errors: $C_{ij} = \mathrm{E}\left[\varepsilon_i\varepsilon_j\right]$. Using the Lagrange multipliers method to solve for α_i we find (Perrone & Cooper, 1994)

$$\alpha_i = \frac{\sum_{j=1}^{M} C_{ij}^{-1}}{\sum_{i=1}^{M}\sum_{j=1}^{M} C_{ij}^{-1}}. \tag{4.4}$$

Since this is potentially a major reduction in the error of a prediction, the fusion of models should always be undertaken when possible. The fusion-of-models scheme will be further described in Section 4.2.

4.2 Characterisation of epileptic events from real data

The schemes for biomedical data fusion have been introduced in the previous Section. We propose to compare their performances with respect to the performances of the unimodal models for epileptic seizure detection investigated in the previous chapter. The performance of the biomedical fusion schemes is evaluated on real patient data. We compare the performance of the different fusion schemes by plotting the receiver operating characteristics (ROC) graphs of the classifiers and by comparing their area under the ROC curve (AUC).

4.2.1 Characterisation of epileptic events from unimodal data

Epileptic events have been characterised using a variety of methods based on EEG analysis (Chapter 2). Recently, following the observation that epileptic seizures affected the heart through the central autonomic network, epileptic events detection has been performed using the ECG time series (Kerem & Geva, 2005). In the following paragraphs

we will present the results of epileptic seizure detection based on unimodal data and a measure of complexity of the EEG time series (Section 2.2.2) or a measure of the occurrence of a heart arrhythmia (Section 3.3.2).

EEG data

The detection of epileptic events based on the EEG time series only and the computation of the Kullback-Leibler divergence as a measure of complexity of the state of the brain is performed by applying to the information measure the threshold which will lead to a maximum sensitivity with a minimum number of false positives.

Figure 4.5 is a plot of the Kullback-Leibler divergence computed on real patient data. In Chapter 2 we demonstrated that the KL-divergence was sensitive to epileptic events and chewing artifacts: the information measure increases with respect to the baseline for such events. If the measure was to be thresholded to be sensitive to all epileptic events, alarms would be raised for non-epileptic events (e.g. chewing artifacts). The detection of epileptic events based on the EEG time series and the computation of the Kullback-Leibler divergence as a measure of the complexity of the state of the brain lead to detection of epileptic events but corrupted by artifactual false positives.

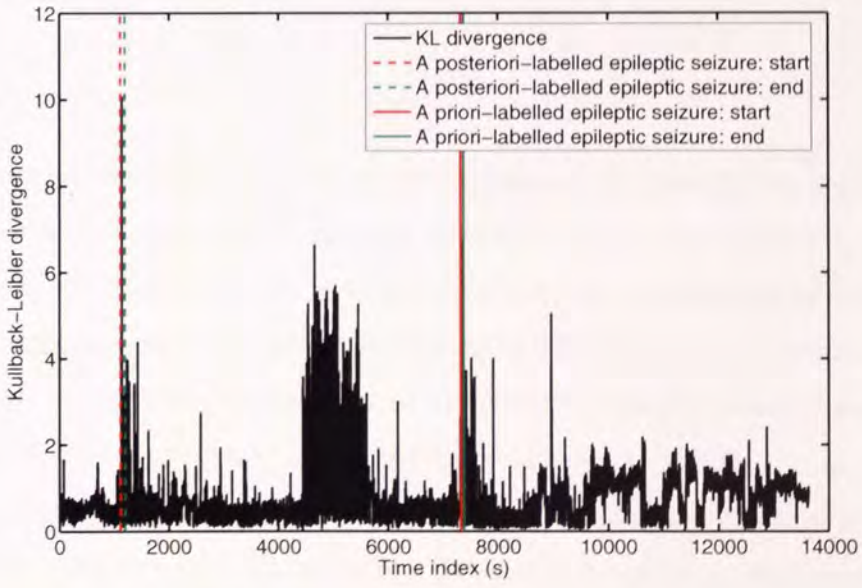

Figure 4.5: Kullback-Leibler divergence of a single channel of EEG (T3). The accurate detection of genuine epileptic events would induce many false positives (e.g. 4400-5600 seconds epoch).

Figure 4.6 is the ROC graph of the classifier based on the Kullback-Leibler divergence only. The performance of the classifier based on the measure of complexity only is reasonable: the area under the curve is 0.5638.

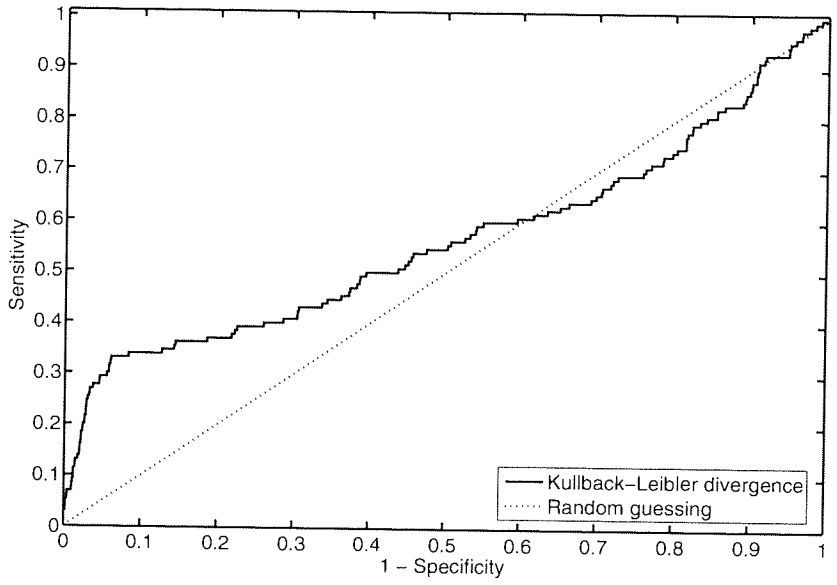

Figure 4.6: Receiver operating characteristic (ROC) curve of the Kullback-Leibler divergence-based epileptic events classifier. Its area under the curve (AUC) is 0.5638: the classifier performs slightly better than random guessing (AUC: 0.5).

ECG data

The biological mechanisms underlying the alteration of the heart rhythm during epileptic events have been identified but not fully described. Due to the uncertainty around the systematic observation of heart arrhythmias (tachycardia or bradycardia) the ECG time series cannot be used as the primary tool for epileptic seizure events detection.

Figure 3.13 gave the plot of the posterior probability of the tachycardia class-membership given the features extracted from the distribution of R-R intervals $\mathbf{F}_{\mathrm{ECG}} = (\mu, \sigma^2)$.

The choice of an appropriate threshold would lead to a sensitivity close to 100% and to a reduced number of false positives. The exemplar recording used to compute the occurrence of a tachycardia episode shown in Figure 3.13 seems to flag various episodes: the patient suffered tachycardia episodes not only due to epileptic events but also to non-epileptic factors. The unimodal approach towards epileptic events detection using the ECG raised undesirable false positives.

We suggest that the electrocardiogram should not be used as the primary tool for epileptic events detection but that the complementary information provided by the ECG time series should be combined with the probabilistic information content provided by the EEG time series in a fusion scheme towards an improved diagnosis model for epileptic event detection.

4.2.2 Characterisation of epileptic events from multimodal data

The methods for combining multimodal data at the different levels of the fusion hierarchy towards temporal lobe epileptic seizure detection will be described in the next paragraph. The results and discussion of the results will then be presented in the following paragraphs.

Methods

We propose to flag an epoch as an epileptic event based on the posterior probability of epileptic seizure given the information available (observations or features) at this epoch. The posterior probability was referred to as $p(\mathbf{x}_1, \mathbf{x}_2, \ldots, \mathbf{x}_N)$ or $p(\mathbf{F}(\mathbf{x}_1), \mathbf{F}(\mathbf{x}_2), \ldots, \mathbf{F}(\mathbf{x}_N))$ in the figures of Section 4.1. The estimation of the posterior probability of epileptic seizure given information available, common to all schemes of fusion (except the fusion-of-models scheme) presented in the previous Section, will be detailed in the reminder of this Section and referred to and augmented in the next paragraphs, focussing on each scheme of biomedical data fusion.

The goal of our work is to combine observations ($\mathbf{x}_i(t)$), features ($\mathbf{F}(\mathbf{x}_i(t))$), probabilities ($p(\mathbf{F}(\mathbf{x}_i(t)))$) or decisions ($D\{p(\mathbf{F}(\mathbf{x}_i(t)))\}$) towards temporal lobe epileptic seizure detection. We would like to combine the above-mentioned items towards the classification of the epoch they belong to into one of the two distinct classes: temporal lobe epileptic event and non-temporal lobe epileptic event. The goal of a classification problem is to model the posterior probabilities $P(C_k|\mathbf{x})$ of classes C_k.

In this work the posterior probabilities of class-membership are estimated through a machine learning approach: one radial basis function (RBF) network, whose inputs depend on the fusion scheme (fusion of observations, features, probabilities or decisions), is used to derive the posterior probabilities of class-membership given a new measurement (observations or features). The number of outputs of the networks is set to two: the two

exclusive classes *Epileptic seizure* (C_E) and *non-Epileptic seizure* ($\overline{C_E}$). If the targets of the RBF network are appropriately chosen (e.g. class 1: $[1,0]$; class 2: $[0,1]$) and an adequate optimisation scheme used, the optimum network outputs approximate conditional probabilities (Nabney, 2004). The number of hidden units of the RBF network to be chosen for the network to have the best performance on new data is estimated by a cross-validation approach (Bishop, 1995): a training set is divided into ten distinct segments; nine of them are used to train the network while the tenth is used to test its performance (by evaluating the error function). The process is repeated over the ten possible choices of test segments. The test errors are then averaged over the ten sets and the performance of models with different numbers of hidden units (the number of hidden units ranges from 2 to 25) compared. The network with the lowest average test error is retained as the "best" model.

To obtain the posterior probabilities for a given recording, the latter is kept aside for testing. An RBF network is trained on a balanced training set constructed from the concatenation of the same number of observations or features characteristic of epileptic events and of randomly chosen epochs characteristic of non-epileptic events of a selected training recording. The corresponding outputs are set to zero or one according to the class membership of the measurement. The separate recording used as an independent test set is forward-propagated to obtain the estimates of the posterior distributions given the observations or features.

Fusion of observations

In the fusion-of-observations scheme the raw unprocessed information is transmitted up the hierarchy: the inputs of the RBF network used to estimate the posterior probability of epileptic seizure given observations, $P(C_E|\mathrm{X})$ with $\mathrm{X} = \mathbf{x}_{\mathrm{ECG}} \oplus \mathbf{x}_{\mathrm{EEG}}$, are the ECG and EEG time series. Due to the high level of noise and the redundancy of biomedical time series the model is expected to perform poorly.

Fusion of features

In the fusion-of-features scheme the features extracted from the biomedical time series (the measure of class-membership to the tachycardia class for the ECG, $P(C_T|\mathbf{F}_{\mathrm{ECG}})$ with $\mathbf{F}_{\mathrm{ECG}} = (\mu, \sigma^2)$, and the Kullback-Leibler divergence for the EEG, D_{KL}) are combined

through an RBF network to estimate the posterior probability of epileptic seizure given multimodal data, $P(C_E|X)$ with $X = \mathbf{F}_{ECG} \oplus \mathbf{F}_{EEG}$ (Figure 4.7).

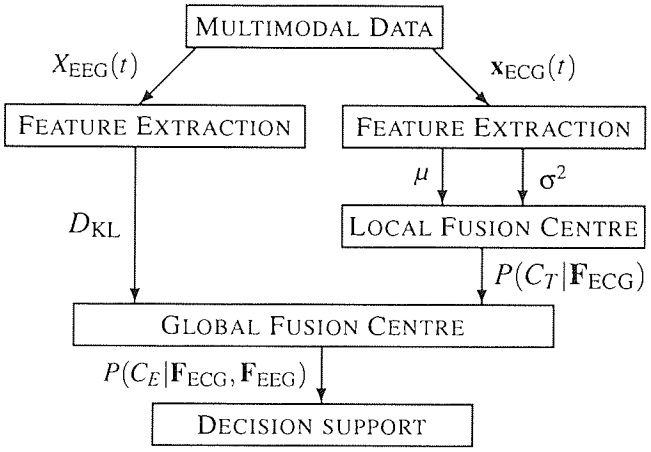

Figure 4.7: Fusion of features towards TLE seizure detection. D_{KL}: Kullback-Leibler divergence; $\mathbf{F}_{ECG} = D_{KL}$: vector of features extracted from the EEG time series; $\mathbf{F}_{ECG} = (\mu, \sigma^2)$: vector of features extracted from the ECG R-R intervals distribution.

The results of the approach on real patient data are presented in Figure 4.8: the two genuine (a priori- and a posteriori-labelled) epileptic events can possibly be flagged as epileptic events once an appropriate threshold has been chosen. A dramatically reduced number of false positives (with comparison to the number of those obtained in the fusion-of-observations scheme) would be flagged if a sensitivity of 100% was to be achieved.

Figure 4.9 is the ROC graph of the classifier obtained from the fusion-of-features scheme applied on a single model. The classifier performs exceedingly well: its AUC is 0.9659. The results for the committees of models will be discussed in a next Section.

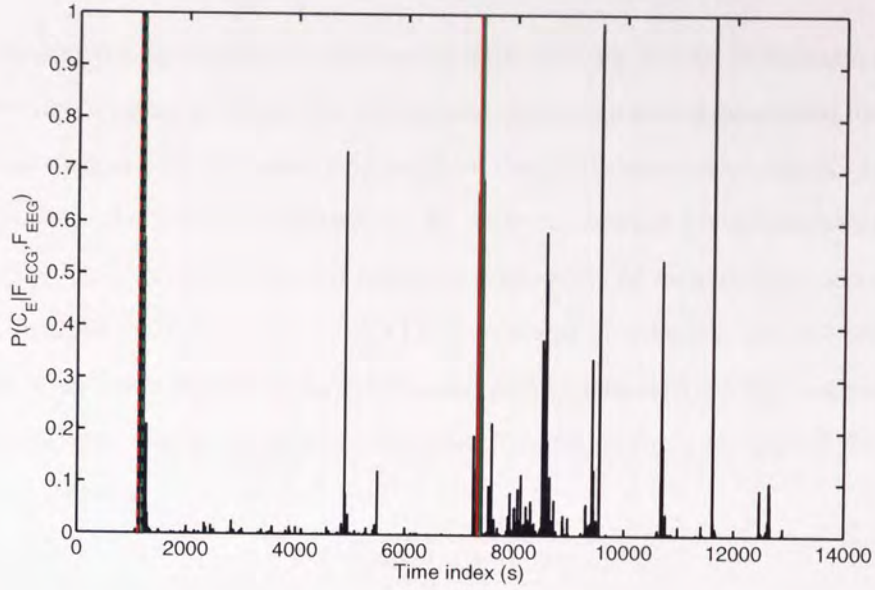

Figure 4.8: Posterior probability of epileptic seizure given features extracted from ECG and EEG times series, $P(C_E|\mathbf{F}_{\text{ECG}},\mathbf{F}_{\text{EEG}})$, obtained in a fusion-of-features scheme. The genuine epileptic seizures are accurately detected while few false positives are induced.

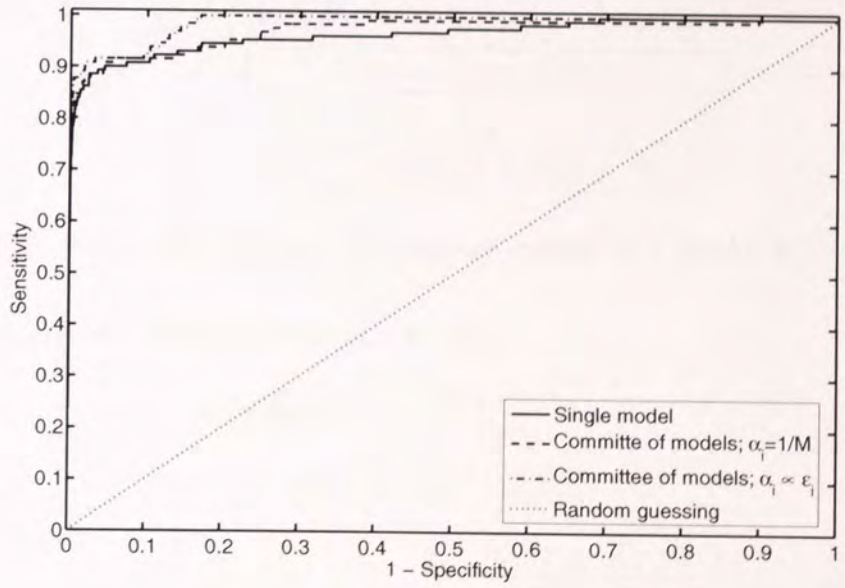

Figure 4.9: ROC curve of classifiers in a fusion-of-features scheme. The AUCs for a single model and a committee of models with equal weights and with weights inversely proportional to their fitting errors are 0.9659, 0.9732 and 0.9879 respectively: the classifiers provide excellent diagnostics. The classifiers based on committees of models outperform the classifier based on a single model.

Fusion of probabilities

For the fusion-of-probabilities scheme, an RBF network is used to estimate the posterior probability of epileptic seizure given unimodal EEG data which means that the input of the RBF network are the features extracted from the EEG times series (the Kullback-Leibler divergence); the posterior probability of epileptic seizure given unimodal ECG data, $P(C_E|\mathbf{F}_{\mathrm{ECG}})$, is derived from the posterior probability of tachycardia class-membership given features extracted from the ECG R-R intervals distribution; and the posterior probability of epileptic seizure given multimodal data is derived from the posterior probabilities of epileptic seizure given unimodal data: $P(C_{\mathrm{E}}|\mathrm{X}) = P(C_{\mathrm{E}}|\mathbf{F}_{\mathrm{ECG}}) \oplus P(C_{\mathrm{E}}|\mathbf{F}_{\mathrm{EEG}})$ with $\mathrm{X} = \mathbf{F}_{\mathrm{ECG}} \oplus \mathbf{F}_{\mathrm{EEG}}$.

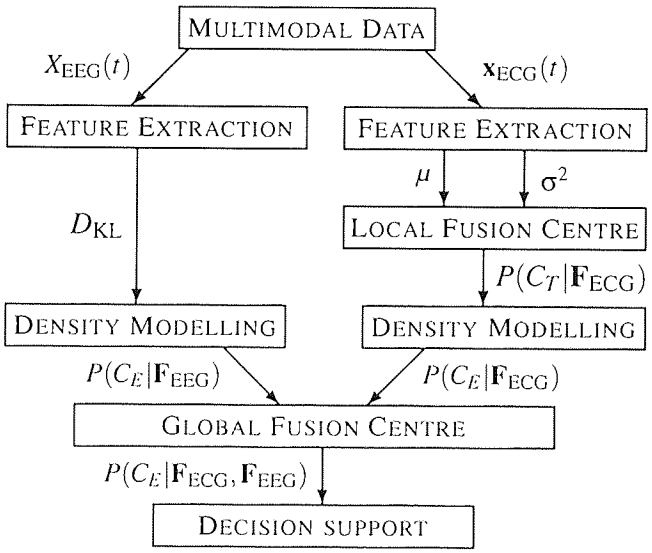

Figure 4.10: Fusion of probabilities towards TLE seizure detection.

$P(C_E|\mathbf{F}_{\mathrm{ECG}})$ is derived from $P(C_T|\mathbf{F}_{\mathrm{ECG}})$:

$$\begin{aligned} P(C_E|\mathbf{F}_{\mathrm{ECG}}) &= \frac{P(C_E, \mathbf{F}_{\mathrm{ECG}})}{P(\mathbf{F}_{\mathrm{ECG}})} \\ &= \frac{\sum_T P(C_E, \mathbf{F}_{\mathrm{ECG}}, C_T)}{P(\mathbf{F}_{\mathrm{ECG}})} \\ &= \frac{\sum_T P(C_E, \mathbf{F}_{\mathrm{ECG}}|C_T)P(C_T)}{P(\mathbf{F}_{\mathrm{ECG}})}. \end{aligned}$$

By conditional independence: $P(C_E, \mathbf{F}_{\mathrm{ECG}}|C_T) = P(C_E|C_T)P(\mathbf{F}_{\mathrm{ECG}}|C_T)$. Hence

$$P(C_E|\mathbf{F}_{\mathrm{ECG}}) = \frac{\sum_T P(C_E|C_T)P(\mathbf{F}_{\mathrm{ECG}}|C_T)P(C_T)}{P(\mathbf{F}_{\mathrm{ECG}})}.$$

Using Bayes' theorem

$$P(C_k|\mathbf{x}) = \frac{p(\mathbf{x}|C_k)P(C_k)}{p(\mathbf{x})}, \tag{4.5}$$

$$\begin{aligned} P(C_E|\mathbf{F}_{\mathrm{ECG}}) &= \sum_T P(C_E|C_T)P(C_T|\mathbf{F}_{\mathrm{ECG}}) \\ &= P(C_E|C_T)P(C_T|\mathbf{F}_{\mathrm{ECG}}) + P(C_E|\overline{C_T})P(\overline{C_T}|\mathbf{F}_{\mathrm{ECG}}) . \end{aligned} \quad (4.6)$$

Since the population studied suffers from temporal lobe epilepsy, tachycardia episodes are systematically expected to be observed during seizures. The converse is that if no tachycardia episode is observed, no temporal lobe epileptic seizures occurs: in (4.6) the term $P(C_E|\overline{C_T})$ is set to zero:

$$P(C_E|\mathbf{F}_{\mathrm{ECG}}) = P(C_E|C_T)P(C_T|\mathbf{F}_{\mathrm{ECG}}) .$$

The conditions of acquisition of the biomedical recordings discard tachycardia episodes caused by activity and exercise. Moreover the prevalence of tachycardia induced by a condition is low in the general population. Due to these two factors we set $P(C_E|C_T) = 1$ (i.e. the occurrence of a tachycardia episode is due to the occurrence of a temporal lobe epileptic seizure). Hence

$$P(C_E|\mathbf{F}_{\mathrm{ECG}}) = P(C_T|\mathbf{F}_{\mathrm{ECG}}) . \quad (4.7)$$

The posterior probability of epileptic seizure given multimodal data is obtained from the separate posterior probabilities of epileptic seizure given unimodal data. Using Bayes' theorem (4.5)

$$P(C_E|\mathbf{F}_{\mathrm{ECG}}, \mathbf{F}_{\mathrm{EEG}}) = \frac{P(\mathbf{F}_{\mathrm{ECG}}, \mathbf{F}_{\mathrm{EEG}}|C_E)P(C_E)}{P(\mathbf{F}_{\mathrm{ECG}}, \mathbf{F}_{\mathrm{EEG}})} .$$

Considering the influence of the epileptic activity on the complexity of the state of the brain conditionally independent from the influence of the epileptic activity on the heart rhythm, the posterior probability of epileptic seizure given a multimodal observation is written as:

$$\begin{aligned} P(C_E|\mathbf{F}_{\mathrm{ECG}}, \mathbf{F}_{\mathrm{EEG}}) &= \frac{P(\mathbf{F}_{\mathrm{ECG}}|C_E)P(\mathbf{F}_{\mathrm{EEG}}|C_E)P(C_E)}{P(\mathbf{F}_{\mathrm{ECG}}, \mathbf{F}_{\mathrm{EEG}})} \\ &= \frac{1}{P(C_E)} \frac{P(\mathbf{F}_{\mathrm{ECG}})P(\mathbf{F}_{\mathrm{EEG}})}{P(\mathbf{F}_{\mathrm{ECG}}, \mathbf{F}_{\mathrm{EEG}})} P(C_E|\mathbf{F}_{\mathrm{ECG}})P(C_E|\mathbf{F}_{\mathrm{EEG}}) . \end{aligned} \quad (4.8)$$

$$P(\mathbf{F}_{\mathrm{ECG}}, \mathbf{F}_{\mathrm{EEG}}) = P(\mathbf{F}_{\mathrm{ECG}}, \mathbf{F}_{\mathrm{EEG}}|C_E)P(C_E) + P(\mathbf{F}_{\mathrm{ECG}}, \mathbf{F}_{\mathrm{EEG}}|\overline{C_E})P(\overline{C_E}) .$$

By conditional independence

$$P(\mathbf{F}_{\mathrm{ECG}}, \mathbf{F}_{\mathrm{EEG}}|\overline{C_E}) = P(\mathbf{F}_{\mathrm{ECG}}|\overline{C_E})P(\mathbf{F}_{\mathrm{EEG}}|\overline{C_E}) ,$$

moreover

$$P(\mathbf{F}_{\mathrm{ECG}}|\overline{C_E}) = \frac{P(\overline{C_E}|\mathbf{F}_{\mathrm{ECG}})P(\mathbf{F}_{\mathrm{ECG}})}{P(\overline{C_E})}.$$

Hence

$$\frac{P(\mathbf{F}_{\mathrm{ECG}},\mathbf{F}_{\mathrm{EEG}})}{P(\mathbf{F}_{\mathrm{ECG}})P(\mathbf{F}_{\mathrm{EEG}})} = \frac{P(C_E|\mathbf{F}_{\mathrm{ECG}})P(C_E|\mathbf{F}_{\mathrm{EEG}}) + P(C_E)\left(1 - P(C_E|\mathbf{F}_{\mathrm{ECG}}) - P(C_E|\mathbf{F}_{\mathrm{EEG}})\right)}{P(C_E)P(\overline{C_E})}. \tag{4.9}$$

Finally using (4.9) in (4.8)

$$P(C_E|\mathbf{F}_{\mathrm{ECG}},\mathbf{F}_{\mathrm{EEG}}) = \frac{(1 - P(C_E))\,P(C_E|\mathbf{F}_{\mathrm{ECG}})P(C_E|\mathbf{F}_{\mathrm{EEG}})}{P(C_E|\mathbf{F}_{\mathrm{ECG}})P(C_E|\mathbf{F}_{\mathrm{EEG}}) + P(C_E)\left(1 - P(C_E|\mathbf{F}_{\mathrm{ECG}}) - P(C_E|\mathbf{F}_{\mathrm{EEG}})\right)}. \tag{4.10}$$

Note that $P(\overline{C_E}) = 1 - P(C_E)$.

The prior term, $P(C_E)$, appearing in the expression of the posterior probability of epileptic seizure given multimodal data, $P(C_E|\mathbf{F}_{\mathrm{ECG}},\mathbf{F}_{\mathrm{EEG}})$, should be interpreted carefully. $P(C_E)$ stands for the prevalence of the epileptic condition, ρ_E, in a sample of population: if the latter is the global population, $P(C_E)$ is set to a low value; if the sample is a group of epileptic patients the prevalence term should be taken to be a high value.

The results of the fusion-of-probabilities scheme on real patient data are presented in Figure 4.13 ($P(C_E) = \rho_E = 0.05$, low prevalence of epilepsy in the population studied) and Figure 4.14 ($\rho_E = 0.95$, high prevalence of epilepsy in the population studied). The data redundancy is reduced and all relevant information is encoded by probability vectors: the EEG biomarker through its posterior probability of TLE seizure (Figure 4.12) imposes its veto to the ECG biomarker when the latter is sensitive to non-TLE induced arrhythmia. Likewise the ECG biomarker imposes its veto through its posterior probability of epileptic seizure (Figure 4.11) to the EEG biomarker when the latter is sensitive to non-epileptic phenomena such as artifacts. The number of false positives is considerably reduced.

Figure 4.15 is the ROC graph for the classifier obtained from the fusion-of-probabilities scheme on a single model. The classifier perform well: its AUC is 0.9809. The results obtained for committees of models are discussed in a next Section.

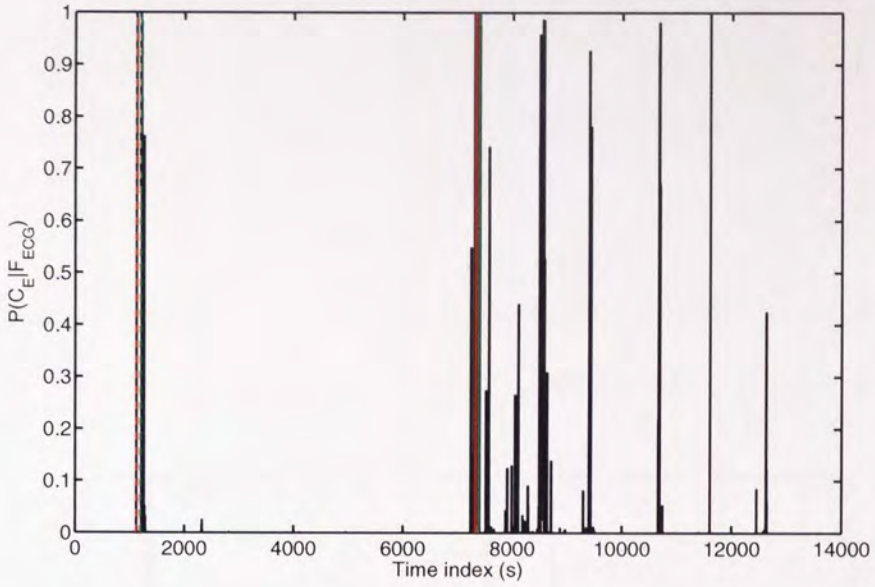

Figure 4.11: Posterior probability of epileptic seizure given the features extracted from the distribution of R-R intervals: $P(C_E|\mathbf{F}_{\text{ECG}})$. The plot is identical to Figure 3.13 following the result obtained in (4.7).

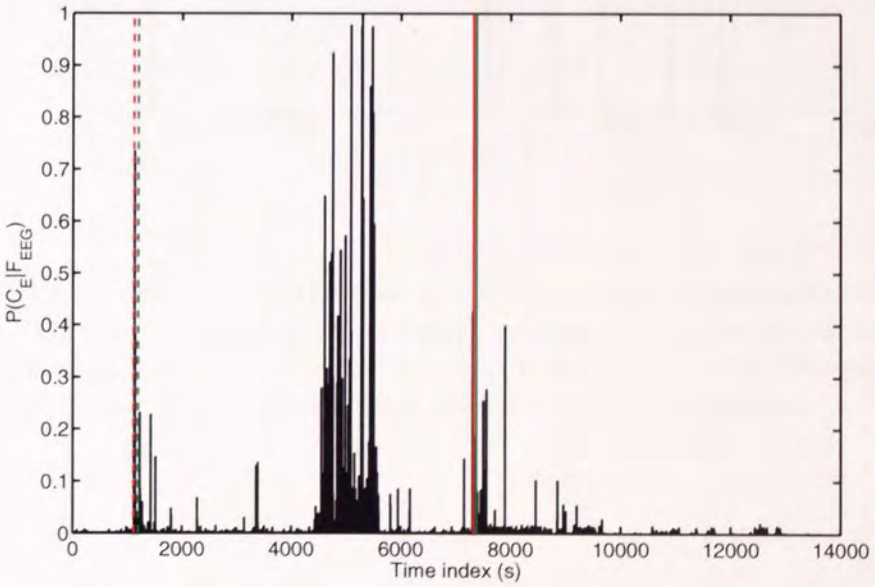

Figure 4.12: Posterior probability of epileptic seizure given the features extracted from the EEG time series: $P(C_E|\mathbf{F}_{\text{EEG}})$. The accurate detection of genuine epileptic events would induce false positives (e.g. 4400-5600 seconds epoch) but dramatically less than the number of false positives induced by the classifier based on the Kullback-Leibler divergence only (Figure 4.5).

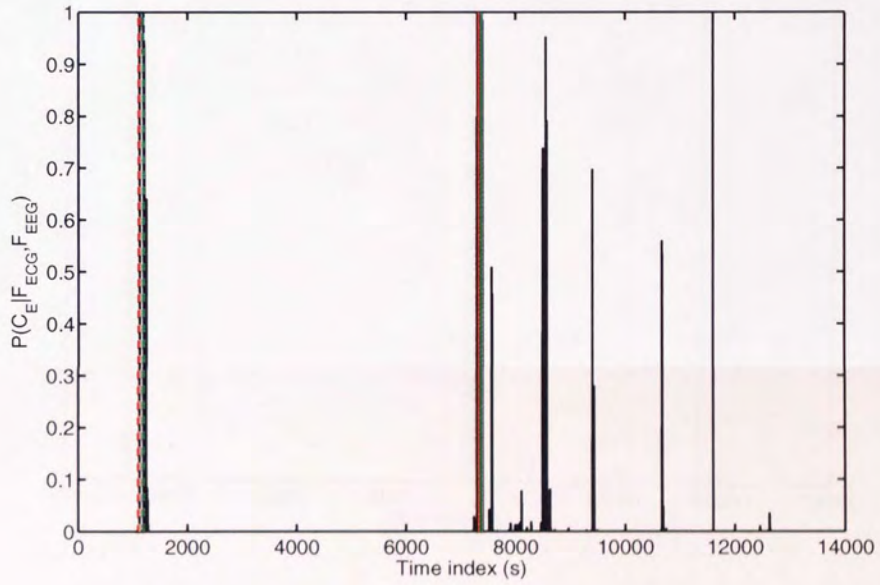

Figure 4.13: Posterior probability of epileptic seizure given features extracted from ECG and EEG times series, $P(C_E|\mathbf{F}_{\text{ECG}}, \mathbf{F}_{\text{EEG}})$, obtained in a fusion-of-probabilities scheme. The incidence of the condition in the population is $\rho_E = 0.05$. The genuine epileptic seizures are accurately detected while few false positives are induced.

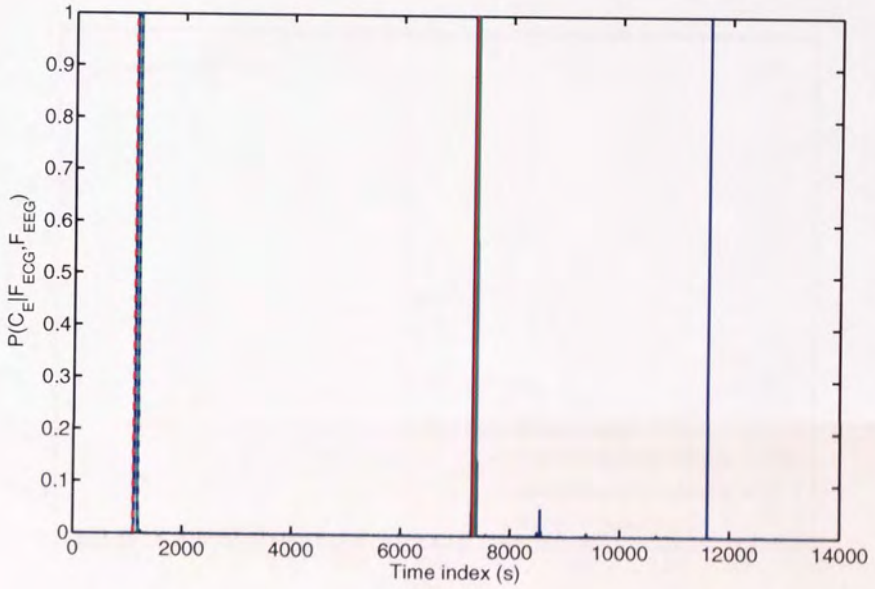

Figure 4.14: Posterior probability of epileptic seizure given features extracted from ECG and EEG times series, $P(C_E|\mathbf{F}_{\text{ECG}}, \mathbf{F}_{\text{EEG}})$, obtained in a fusion-of-probabilities scheme. The incidence of the condition in the population is $\rho_E = 0.95$. The genuine epileptic seizures are accurately detected while very few false positives are induced. The higher value of the prevalence of the epileptic condition in the population ($\rho_E = 0.95$) allows for the dramatic reduction of the number of false positives when compared with the classifier presented in Figure 4.13 ($\rho_E = 0.05$).

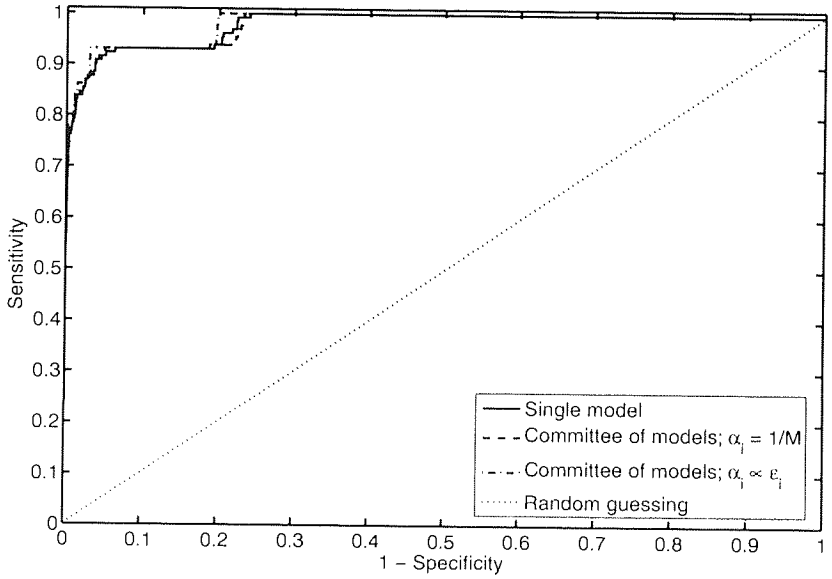

Figure 4.15: ROC curve of classifiers in a fusion-of-probabilities scheme with $\rho_E = 0.05$. The AUCs for a single model and a committee of models with equal weights and with weights inversely proportional to their prediction errors are 0.9809, 0.9806 and 0.9834 respectively: the classifiers provide excellent diagnostics. The classifiers in a fusion-of-probabilities scheme outperform the classifiers in a fusion-of-features scheme (Figure 4.9).

Fusion of decisions

In the fusion-of-decisions scheme independent models for estimating the posterior probabilities of epileptic seizure given unimodal data are built (in the same way as described in the previous paragraph) and binary decisions based on these posterior probabilities are inferred: $D(C_E|X) = D\{P(C_E|\mathbf{F}_{ECG})\} \oplus D\{P(C_E|\mathbf{F}_{EEG})\}$ with $X = \mathbf{F}_{ECG} \oplus \mathbf{F}_{EEG}$. The decisions are then combined by multiplication (Figure 4.16) using an assumption of independence of models.

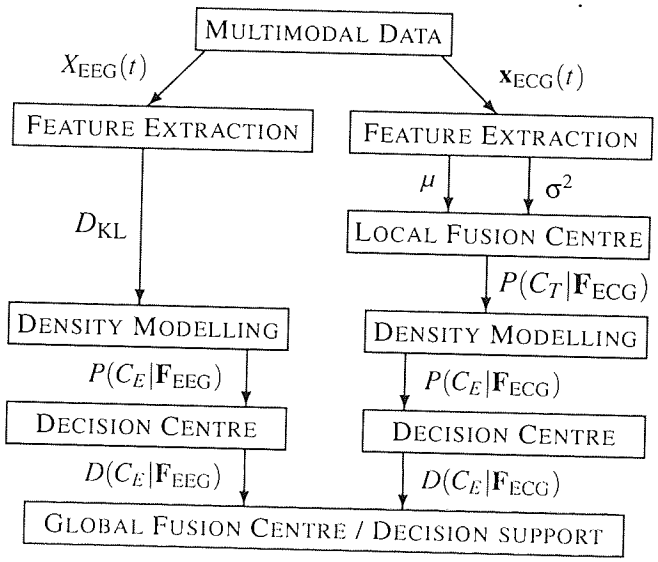

Figure 4.16: Fusion of decisions towards TLE seizure detection. D: Decision.

The results of the fusion-of-decisions scheme on real patient data are presented in Figure 4.19. To issue a positive diagnostic of TLE seizure the fusion-of-decisions scheme requires the binary decisions derived from both the ECG and EEG biomarkers to agree (Figure 4.17 and 4.18). The degree of belief of the occurrence of a temporal lobe epileptic seizure as derived from the EEG biomarker is lost when the binary partial decision is taken: the hard, uncompromising decisions passed up to the global fusion centre eliminate a lot of medically-relevant knowledge. Due to this fact, a sensitivity of 100% cannot be achieved: the genuine epileptic seizures are partially flagged.

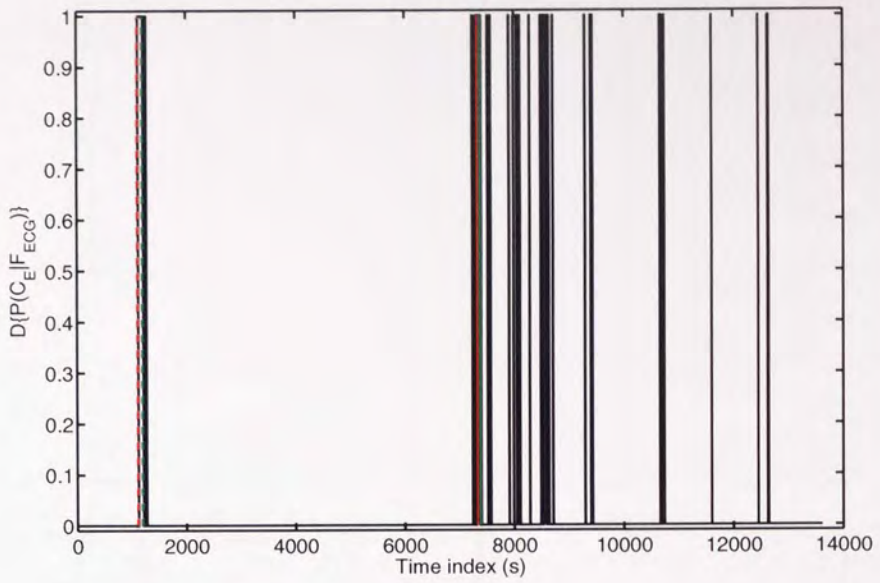

Figure 4.17: Decisions derived from the posterior probability of epileptic seizure given the features extracted from the distribution of R-R intervals: $P(C_E|\mathbf{F}_{\mathrm{ECG}})$. We note that many false positives are induced after the second genuine epileptic seizure.

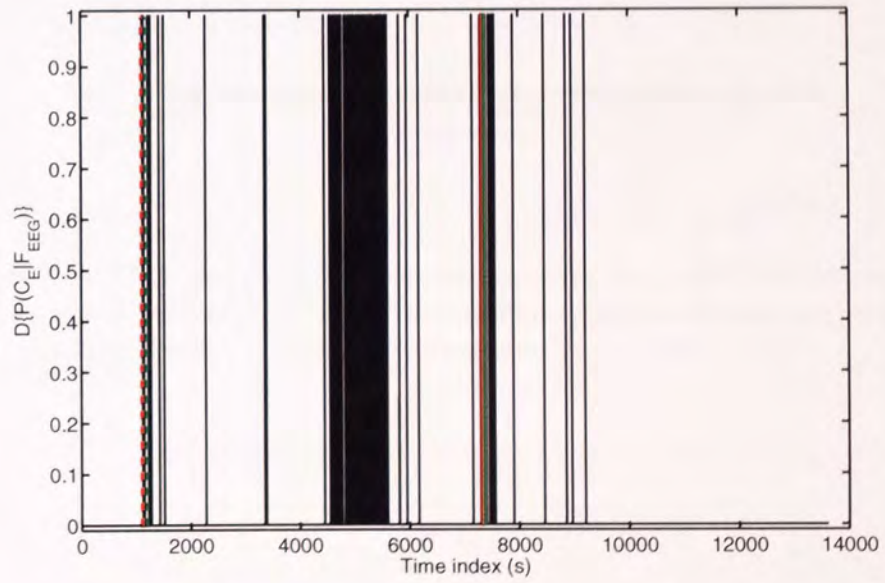

Figure 4.18: Decisions derived from the posterior probability of epileptic seizure given the features extracted from the EEG time series: $P(C_E|\mathbf{F}_{\mathrm{EEG}})$. Many false positives are induced in the epoch between the two genuine epileptic seizures (4400-5600 seconds epoch).

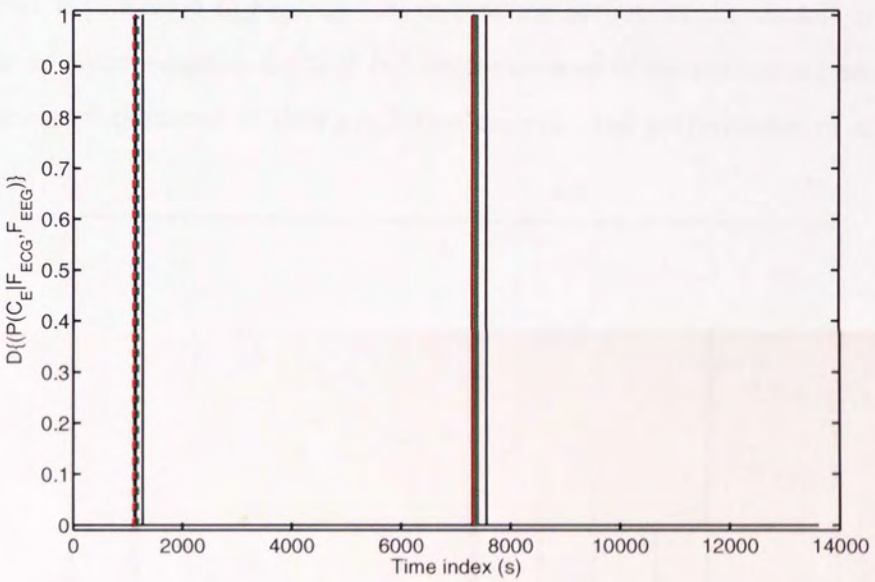

Figure 4.19: Decisions given features extracted from ECG and EEG times series obtained in a fusion-of-decisions scheme. The genuine epileptic seizures are partially flagged. Only one false positive is induced by the scheme at $t = 7600$s.

Fusion of models

The fusion-of-models scheme can be undertaken at various levels of the fusion hierarchy. The purpose of such a scheme is to improve the output of models by averaging them or by combining them by order of importance according to a criterion (Section 4.1.5): $P(C_{\mathrm{E}}|\mathrm{X}) = P_1(C_{\mathrm{E}}|\mathrm{X}) \oplus \ldots \oplus P_M(C_{\mathrm{E}}|\mathrm{X})$ with $\mathrm{X} = \mathbf{F}_{\mathrm{ECG}} \oplus \mathbf{F}_{\mathrm{EEG}}$. We demonstrated in the previous paragraphs that the fusion-of-features scheme and the fusion-of-probabilities scheme were the most interesting schemes of fusion of biomedical data due to their probabilistic output (or "degree of belief") on which a decision is taken.

The fusion-of-models (performed by combining five models) on fusion-of-features scheme is presented in Figures 4.20 (where the outputs of the models are averaged or assigned equal weights) and 4.21 (where the outputs of the models are assigned weights inversely proportional to their prediction errors). The performance of a committee of

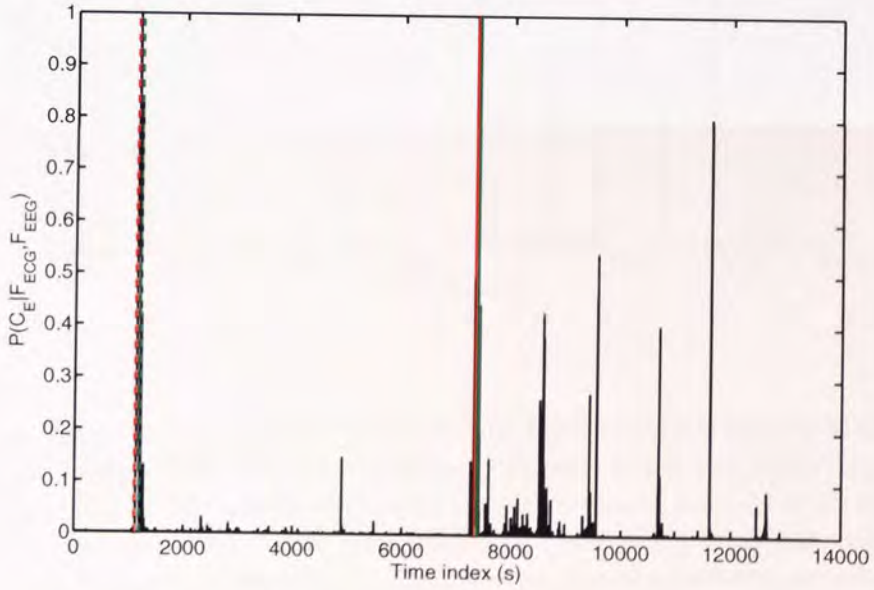

Figure 4.20: Posterior probability of epileptic seizure given features extracted from ECG and EEG times series, $P(C_E|\mathbf{F}_{\mathrm{ECG}}, \mathbf{F}_{\mathrm{EEG}})$, obtained in a fusion-of-models on fusion-of-features scheme. The committee members were assigned equal weights. The performance of a committee of models with equal weights is slightly better than the performance of the classifier based on a single model in a fusion-of-features scheme presented in Figure 4.8.

models combined with equal weights presented in Figure 4.20 is slightly better than the performance of the classifier based on a single model in a fusion-of-features scheme presented in Figure 4.8.

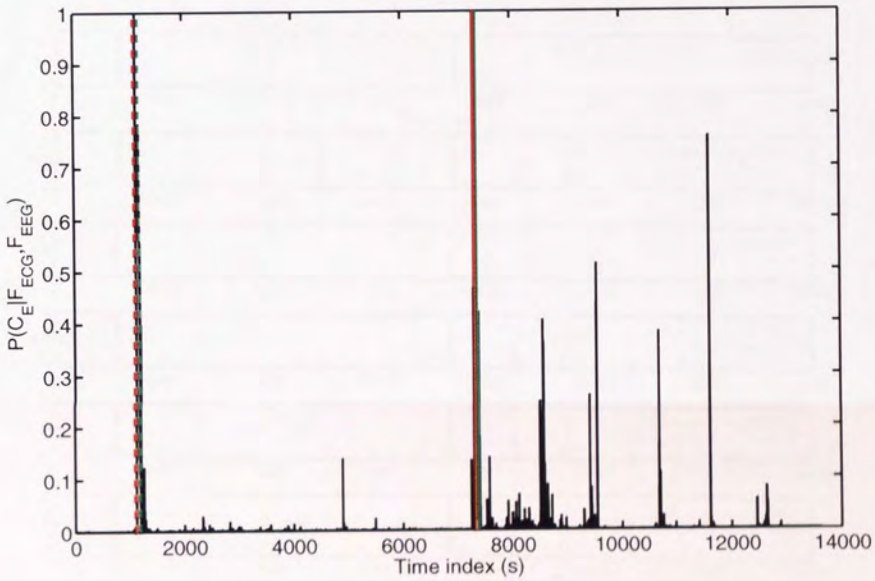

Figure 4.21: Posterior probability of epileptic seizure given features extracted from ECG and EEG times series, $P(C_E|\mathbf{F}_{\text{ECG}}, \mathbf{F}_{\text{EEG}})$, obtained in a fusion-of-models on fusion-of-features scheme. The committee members were assigned weights inversely proportional to their prediction errors. The performance of a committee of models with weights proportional to their performances is slightly better than the performance of a committee of models with equal weights in Figure 4.20.

The performance of a committee of models combined with weights inversely proportional to their prediction errors presented in Figure 4.21 is slightly better than the performance of the classifier based on a committee of models with equal weights presented in Figure 4.20. There are no dramatic difference between the outputs of the models making the committee (except for the output of the second model where no false positive is flagged): the weights assigned to the outputs of the models are hence close to 0.2 (equal weights) except for the second component whose contribution is significantly less (Figure 4.22).

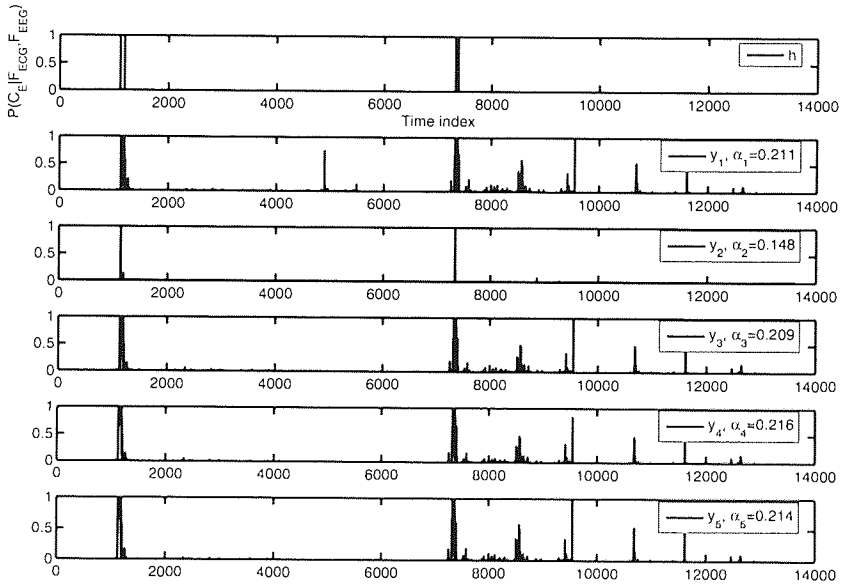

Figure 4.22: Posterior probability of epileptic seizure given features extracted from ECG and EEG times series, $P(C_E|\mathbf{F}_{\text{ECG}}, \mathbf{F}_{\text{EEG}})$, obtained in a fusion-of-features scheme from five models. The outputs of the models were combined in a committee with equal weights (Figure 4.20) or with weights inversely proportional to the prediction errors of the models ($\alpha_i, i = 1, \ldots, 5$; Figure 4.21). h is the underlying true output.

The fusion-of-models on fusion-of-probabilities scheme is presented in Figure 4.23 and 4.24 for two different values of $P(C_E)$: 0.05 (low prevalence of the condition in the population) and 0.95 (high prevalence of the condition in the population). The false positive rate is reduced with increasing values of $P(C_E)$.

The committees of classifiers combined with weights inversely proportional to their prediction errors outperform the classifier based on a single model as denoted by their respective AUCs (Table 4.1).

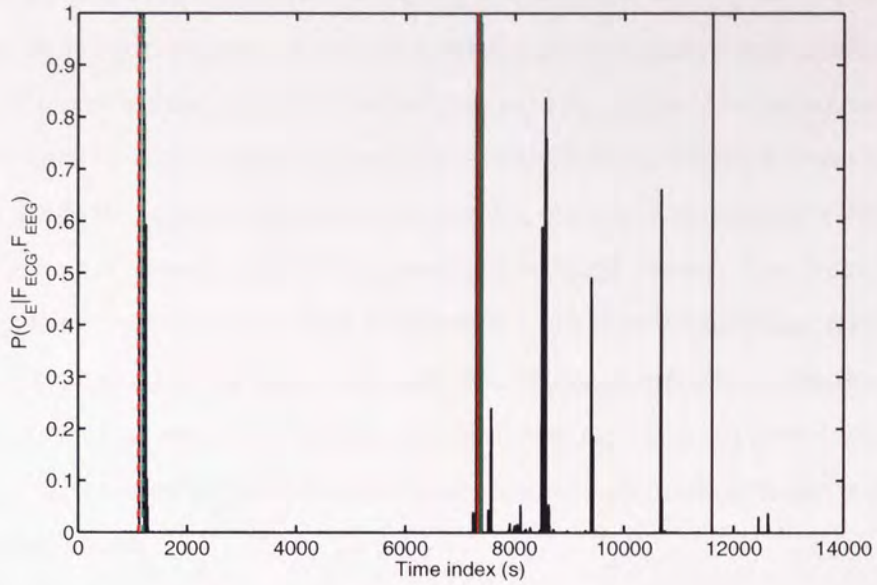

Figure 4.23: Posterior probability of epileptic seizure given features extracted from ECG and EEG times series, $P(C_E|\mathbf{F}_{\text{ECG}}, \mathbf{F}_{\text{EEG}})$, obtained in a fusion-of-models on fusion-of-probabilities scheme with $\rho_E = 0.05$. The committee members were assigned equivalent weights. The committee of classifiers does not outperform the classifier based on a single model as denoted by their respective AUCs (Table 4.1).

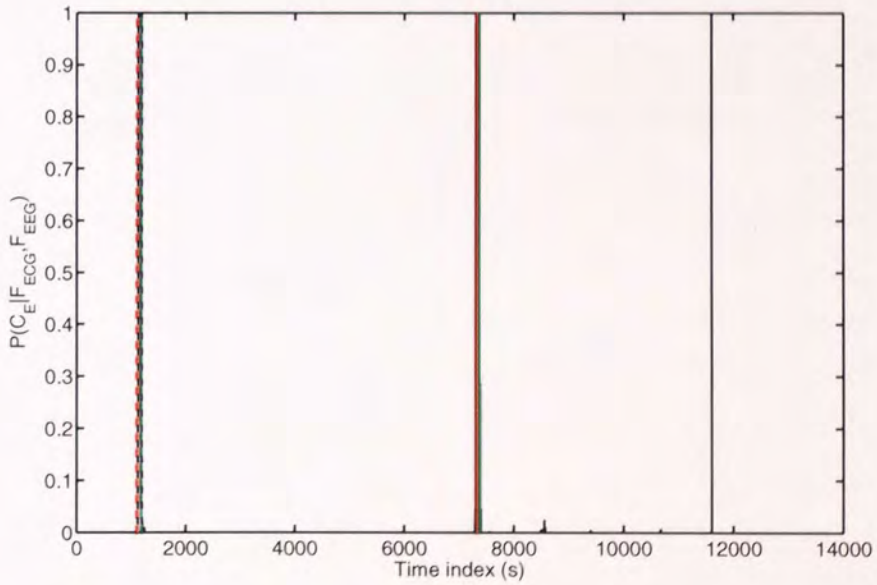

Figure 4.24: Posterior probability of epileptic seizure given features extracted from ECG and EEG times series, $P(C_E|\mathbf{F}_{\text{ECG}}, \mathbf{F}_{\text{EEG}})$, obtained in a fusion-of-models on fusion-of-probabilities scheme with $\rho_E = 0.95$. The committee members were assigned equivalent weights.

The fusion-of-models scheme consisting of combining the outputs of models by assigning them equal weights or weights inversely proportional to their prediction errors provided mixed results. The detection of temporal lobe epileptic seizures benefited from the combination of the outputs of the models obtained in a fusion-of-features framework. This is due to the fact that the performances of the outputs of the models combined differ from each other (meaning one of the classifiers performs "better" than the rest of them) whereas the outputs of the models obtained in a fusion-of-probabilities framework are similar. Contrarily to the result expected from the demonstration in Section 4.1.5 the combination of the outputs of models obtained from the fusion-of-probabilities scheme gave results not as good as, on average, those obtained from a single model on the dataset used in the Thesis.

4.2.3 Discussion

In this Section we investigated the detection of epileptic events from multimodal data and from features extracted from the latter (i.e. the EEG-derived Kullback-Leibler divergence as a measure of complexity of the state of the brain and the ECG-derived distribution of R-R intervals). Firstly we assessed the performance of classifiers based on one feature only. The classifier relying on the EEG feature accurately classified the genuine epileptic events but suffered from many false positives due to the sensitivity of the measure of complexity to artifacts. The classifier relying on the ECG feature accurately classified the genuine epileptic events and suffered from a few false positives only. However in this approach the detection of epileptic events relies on the observation of a side effect of temporal lobe epileptic seizures: tachycardia. The latter being induced by factors such as exercise, malformation or condition we concluded that the alterations of the heart rhythm could not possibly be used as the primary tool for the detection of temporal lobe epileptic events. We then combined the information provided by both modalities of data in a data fusion framework to exploit the complementarity of the two sources of information.

The performances of the classifiers derived from unimodal EEG data and from the combination of multimodal data at different levels of the hierarchy are summarised in Table 4.1 (the results obtained from the fusion-of-observations and the fusion-of-decisions schemes are not shown due to the poor performance of the former and the rigidity of the latter as explained in Section 4.2.2). The fusion approaches outperformed the classifier based on the EEG feature only and provided excellent results. The ROC curves for the classifier based on the EEG feature only and the best fusion-of-features and fusion-of-probabilities schemes are shown in Figure 4.25.

Fusion scheme			AUC
Kullback-Leibler divergence			0.5638
Fusion of features	Single model		0.9659
	Committee	$\alpha_i = \frac{1}{M}$	0.9732
		$\alpha_i \propto \varepsilon_i$	0.9879
Fusion of probabilities	Single model		0.9809
	Committee; $\rho_E = 0.05$	$\alpha_i = \frac{1}{M}$	0.9806
		$\alpha_i \propto \varepsilon_i$	0.9834
	Committee; $\rho_E = 0.95$	$\alpha_i = \frac{1}{M}$	0.9807
		$\alpha_i \propto \varepsilon_i$	0.9834

Table 4.1: Areas under the curve for models based on the Kullbak-Leibler divergence only, fusions schemes and committees of models. The classifier based on the Kullback-Leibler divergence only is dramatically outperformed by the performances of the classifiers based on the fusion schemes and on the committees of models.

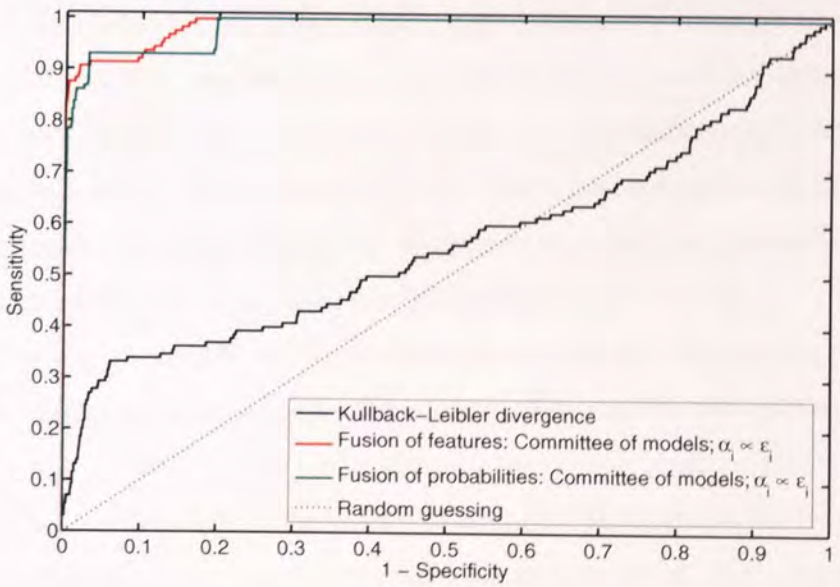

Figure 4.25: ROC curves for the classifiers based on the Kullback-Leibler divergence only, on committees of models with weights inversely proportional to their predictions errors on a fusion-of-features and a fusion-of probabilities schemes. The performance of the classifier based on the Kullback-Leibler divergence only is dramatically outperformed by the performances of the committees of models based on fusion schemes.

4.3 Conclusion

In Chapter 1 a biomedical case for the coupling of the Brain and Heart systems through the activation of the central autonomic network during temporal lobe epileptic seizures was introduced. Such a coupling motivated us to design a framework for the combination of disparate biomedical information towards the improvement of epileptic seizures detection. In this Chapter we introduced the data fusion architecture for the characterisation of epileptic events through the inclusion of cardiac fluctuations. We critically analysed the different levels at which to combine biomedical information from low- to high levels of abstraction (i.e. from sensors to decisions).

The organisation of the different levels of fusion, in a hierarchy, evokes the concession to be made between the optimal conservation of information (low levels of fusion) and the practical exploitation of such information by redundancy reduction (high levels of fusion). At low levels of fusion (fusion-of-observation scheme) the information integrity is optimal but the exploitation of information is impractical due to its highly redundant content. At high levels of fusion (fusion-of-decisions scheme) the information rate of the data is condensed to the point that valuable information extracted from one modality of data is discarded for not being supported by information extracted from the second modality of data. The intermediary levels of data fusion (fusion-of-features and fusion-of-probabilities schemes) provide an optimal balance between information condensation and information integrity. Such schemes for information fusion were proven to dramatically improve the detection of temporal lobe epileptic events when compared with the detection obtained from the measure of complexity of the state of the brain only.

The results obtained from the integration of multimodal data towards temporal lobe epileptic seizure detection on real patient data confirm that the intermediary levels of fusion schemes provide the most relevant results: the genuine epileptic events were flagged whereas the number of false positives was minimal. Furthermore the two schemes associate each alarm with a degree of belief in the occurrence of a temporal lobe epileptic event as a practitioner would.

5 Conclusions and directions for future research

CONTENTS

The aim of the Thesis was given in the Introduction as "the first attempt to the automated false positives-free detection of epileptic events by the fusion of information extracted from simultaneously recorded electroencephalographic- and electrocardiographic time-series". Methods for the automated detection of epileptic events deal with the concepts of sensitivity and specificity (and the related concept of false-positive rate) in a serial manner: a method is designed to achieve the highest sensitivity possible and is then tuned to achieve the lowest false-positive rate. The method proposed in the Thesis integrates a low false-positive rate (tending to zero) as a constraint in the design of the automated detection of epileptic events method, effectively dealing with the concepts of high sensitivity and low false-positive rates in a parallel manner.

5.1 Summary of the Thesis

To achieve the false-positive free automated detection of temporal lobe epileptic events, the main contribution of the Thesis included the introduction of a biomedical case for the coupling of the Brain and Heart systems during temporal lobe epileptic seizures. The biomedical case is partially reported in the clinical literature (partially due to the fact that the nature of the brain arrhythmias, bradycardia or tachycardia, systematically triggered by temporal lobe epileptic events is unknown). This Thesis is, to the author's best knowledge, the first reported use of the biomedical case for the coupling of the Brain and Heart systems for the false-positive free automated detection of temporal lobe epileptic events.

The investigation of measures for the characterisation of ictal events from the EEG time series towards their integration in a fusion-of-knowledge framework was the second step of the analysis. The basic mechanisms of human epilepsy, with a focus at the ictal onset, motivates complexity as a measure of characterisation of the state of the brain. The changes in the complexity of the state of the brain with regards to ictal events are monitored by a nonlinear measure, the correlation dimension, and by information theory measures, the Shannon entropy and the Kullback-Leibler divergence. The correlation dimension was demonstrated to be impractical in a clinical context due to its time-intensive computation and the need for its subjective interpretation. The Kullback-Leibler divergence between the distribution of the amplitudes of the EEG time-series on one-second windows and a reference Gaussian distribution was demonstrated to be sensitive to ictal events and to artifacts: the measure was suitable to the characterisation of ictal events but

needed to be completed in a fusion-of-information framework by a measure not sensitive to artifacts.

To achieve this goal a method for the probabilistic description of arrhythmias observed during temporal lobe epileptic events was designed in the Thesis. The probabilistic description of heart arrhythmias led to the accurate detection of epileptic events and to the discovery of previously unlabelled temporal lobe epileptic seizures. The patients studied systematically suffered from tachycardia during temporal lobe epileptic seizures. The information extracted from the ECG time-series was demonstrated to be suitable, but not by itself, to the detection of temporal lobe epileptic events.

Once appropriate measures for the extraction of information from the EEG and ECG time-series were chosen, the final stage of the analysis consisted in investigating the different levels of the fusion-of-information architecture at which to perform the combination of information extracted from unimodal biomedical time-series in order to "gain" information with regards to the detection of temporal lobe epileptic events. The schemes that provided the best results in terms of the detection of temporal lobe epileptic events were intermediate schemes, particularly the fusion-of-probabilities scheme, for which the degrees of belief in the occurrence of ictal events, extracted from unimodal biomedical time-series, are combined in a Bayesian framework. The approach is similar to clinical practice.

The performance of the method designed in the Thesis for the false-positive free automated detection of epileptic events was assessed by receiver operating characteristic (ROC) curves. The area under the curve (AUC) for the exemplar recording was in the best case of the order of 0.98; the false-positive rates was reduced to zero. The method performed well on the dataset of long-term recordings used in the Thesis.

5.2 Directions for future research

The aim of the directions for future research proposed in the Thesis is to validate the approach introduced in the Thesis and to generalise the approach by:

- **Testing the approach on an extended dataset of temporal lobe epileptic patients:** The dataset of long-term recordings of temporal lobe epileptic patients used in the Thesis is a relatively modest dataset (in terms of recordings, not in terms of samples) and the approach would benefit from being tested on a wider dataset.

- **Extending the fusion of information approach to non-Bayesian frameworks:** In the Thesis the fusion of information was performed in a Bayesian framework since the concepts of "probability" and of "degree of belief" used in clinical practice are related. The fusion of information could be extended to a framework, such as the Dempster-Shafer's framework, for which the concept of probability is replaced by the concepts of probability intervals and uncertainty intervals to determine the likelihood of hypotheses based on multiple evidence (Hall & McMullen, 2004).

- **Constructing probabilistic and machine-learning frameworks for integration of non-cortical biosignals, along with brain-state recordings for improving automated epilepsy characterisation:** Neurovegetative manifestations triggered by activation of the central autonomic network that could be tracked and monitored during ictal events would have to be identified and studied. Fusion models would have to be constructed to integrate the information provided by the neurovegetative manifestations triggered by the ictal events towards the characterisation and diagnosis of epileptic seizures. The overall aim of the proposed research is to integrate information provided from different modalities of biomedical data to reinforce the diagnosis obtained from EEG recordings only. The outcome of the research would be assessed against the ability to establish identifiable relationships between epileptic seizures and the activation of the central autonomic network; and the ability to exploit these relationships in a biomedical data fusion framework to improve the epileptic seizures diagnosis.

- **Integrating the measures of the complexity of the state of the brain and the probabilistic description of heart arrhythmias to a patient's bioprofile:** The measures investigated and the measure resulting from the fusion of the latter could be integrated to a patient's bioprofile as biopatterns for the diagnosis of temporal lobe epilepsy.

- **Evaluating the incidence of a range of artifacts on the method automated for the false-positive free detection of epileptic events:** The main artifacts corrupting the EEG signal were mentioned in Section 2.1.3: eye blinks and bursts of muscle activity. The real patient data used in the Thesis was corrupted by typical muscle artifacts, sometimes induced by epileptic activity: chewing artifacts. The measure of

complexity used in the Thesis was sensitive to chewing artifacts leading to numerous false positives (Section 2.2.2). The method proposed in the Thesis discarded the false positives induced by chewing artifact by augmenting the measure of complexity computed from the EEG signal by a measure derived from the ECG signal, not affected by such artifacts. It is likely that the EEG was further corrupted by bursts of muscle activity or by eye blinks but their effects on the measure of complexity or on the method proposed were not investigated.

References

Applegate, C. D., Kapp, B. S., Underwood, M. D., & McNall, C. L. (1983). Autonomic and somatomotor effects of amygdala central N. stimulation in awake rabbits. *Physiology & Behavior*, *31*, 353–360.

Azuaje, F., Dubitzky, W., Black, N., & Adamson, K. (1999). Improving clinical decision support through case-based data fusion. *IEEE Transactions on Biomedical Engineering*, *46*(10), 1181–1185.

Babiloni, F., Mattia, D., Babiloni, C., Astolfi, L., Salinari, S., Basilisco, A., Rossini, P. M., Marciani, M. G., & Cincotti, F. (2004). Multimodal integration of EEG, MEG and fMRI data for the solution of the neuroimage puzzle. *Magnetic Resonance Imaging*, *22*, 1471–1476.

Baumgartner, C., Lurger, S., & Leutmezer, F. (2001). Autonomic symptoms during epileptic seizures. *Epileptic Disorders*, *3*(3), 103–116.

Bergey, G. K. & Franaszczuk, P. J. (2001). Epileptic seizures are characterized by changing signal complexity. *Clinical Neurophysiology*, *112*, 241–249.

Bishop, C. M. (1995). *Neural networks for pattern recognition*. Oxford university press.

Blumhardt, L. D., Smith, P. E. M., & Owen, L. (1986). Electrocardiographic accompaniments of temporal lobe epileptic seizures. *The Lancet*, *327*, 1051–1056.

Broglin, D. & Bancaud, J. (1991). Manifestations neurovégétatives au cours des crises partielles du lobe temporal. In *Crises épileptiques et épilepsies du lobe temporal*. Rennes: Ligue Française Contre l'Épilepsie, vol. 1 of *Cours de perfectionnement en épileptologie*, 69–96.

Connors, B. W. (1997). Neocortical anatomy and physiology. In J. Engel Jr & T. A. Pedley (Eds.), *Epilepsy: A comprehensive textbook*, Lippincott-Raven Publishers, vol. One, chap. 27. 307–321.

Constantin, L., Martins, J. B., Finchan, R. W., & Dagli, R. D. (1990). Bradycardia and syncope as manifestations of partial epilepsy. *Journal of the American College of Cardiology*, *15*(4), 900–905.

Coulter, D. A. (1997). Thalamocortical anatomy and physiology. In J. Engel Jr & T. A. Pedley (Eds.), *Epilepsy: A comprehensive textbook*, Lippincott-Raven Publishers, vol. One, chap. 29. 341–351.

Cover, T. M. & Thomas, J. A. (2005). *Elements of Information Theory*. John Wiley & Sons.

Daunizeau, J., Grova, C., Marrelec, G., Mattout, J., Jbabdi, S., Pélégrini-Issac, M., Lina, J.-M., & Benali, H. (2007). Symmetrical event-related EEG/fMRI information fusion in a variational bayesian framework. *NeuroImage*, *36*, 69–87.

Daunizeau, J., Grova, C., Mattout, J., Marrelec, G., Clonda, D., Goulard, B., Pélégrini-Issac, M., Lina, J.-M., & Benali, H. (2005). Assessing the relevance of fMRI-based prior in the EEG inverse problem: a bayesian model comparison approach. *IEEE Transactions on Signal Processing*, *53*(9), 3461–3472.

De Clercq, W., Vergult, A., Vanrumste, B., Van Paesschen, W., & Van Huffel, S. (2006). Canonical correlation analysis applied to remove muscle artifacts from the electroencephalogram. *IEEE Transactions on Biomedical Engineering*, *53*, 2583–2587.

Devinsky, O. (2004). Effects of seizures on autonomic and cardiovascular function. *Epilepsy Currents*, *4*(2), 43–46.

Devinsky, O., Price, B. H., & Cohen, S. I. (1986). Cardiac manifestations of complex partial seizures. *The American Journal of Medicine*, *80*, 195–202.

Dichter, M. A. (1997). Overview: The neurobiology of epilepsy. In J. Engel Jr & T. A. Pedley (Eds.), *Epilepsy: A comprehensive textbook*, Lippincott-Raven Publishers, vol. One, chap. 21. 233–235.

Ditcher, M. A. & Wilcox, K. S. (1997). Excitatory synaptic transmission. In J. Engel Jr & T. A. Pedley (Eds.), *Epilepsy: A comprehensive textbook*, Lippincott-Raven Publishers, vol. One, chap. 23. 251–263.

Elger, C. E., Widman, G., Andrzejak, R., Arnhold, J., David, P., & Lehnertz, K. (2000a). Nonlinear EEG analysis and its potential role in epileptology. *Epilepsia*, *41*(s3), S34–S38.

Elger, C. E., Widman, G., Andrzejak, R., Dumpelmann, M., Arnhold, J., Grassberger, P., & Lehnertz, K. (2000b). Value of nonlinear time series analysis of the EEG in neocortical epilepsies. *Advances in Neurology*, *84*, 317–330.

Engel Jr, J., Dichter, M., & Schwartzkroin, P. A. (1997). Basic mechanisms of human epilepsy. In J. Engel Jr & T. A. Pedley (Eds.), *Epilepsy: A comprehensive textbook*, Lippincott-Raven Publishers, vol. One, chap. 42. 499–512.

Galimberti, C. A., Marchioni, E., Barzizza, F., Manni, R., Sartori, I., & Tartara, A. (1996). Partial epileptic seizures of different origin variably affect cardiac rhythm. *Epilepsia*, *37*(8), 742–747.

Gelsema, A. J., Copeland, N. E., Drolet, G., & Bachelard, H. (1993). Cardiovascular effects of neuronal activation of the extended amygdala in rats. *Brain Research*, *626*, 156–166.

Goh, C., Hamadicharef, B., Henderson, G. T., & Ifeachor, E. C. (2005). Comparison of fractal dimension algorithms for the computation of EEG biomarkers for dementia. In *Proceedings of the 2nd international conference on computational intelligence in medicine and healthcare*. 464–471.

Gotman, J. (1982). Automatic recognition of epileptic seizures in the EEG. *Electroencephalography and Clinical Neurophysiology*, *54*, 530–540.

Gotman, J., Flanagan, D., Rosenblatt, B., Bye, A., & Mizrahi, E. M. (1997a). Evaluation of an automatic seizure detection method for the newborn EEG. *Electroencephalography and Clinical Neurophysiology*, *103*, 363–369.

Gotman, J., Flanagan, D., Zhang, J., & Rosenblatt, B. (1997b). Automatic seizure detection in the newborn: methods and initial evaluation. *Electroencephalography and Clinical Neurophysiology, 103*.

Gotman, J., Kobayashi, E., Bagshaw, A. P., Bénar, C.-G., & Dubeau, F. (2006). Combining EEG and fMRI: A multimodal tool for epilepsy research. *Journal of Magnetic Resonance Imaging, 23*, 906–920.

Grassberger, P. & Procaccia, I. (1983a). estimation of the kolmogorov entropy from a chaotic signal. *Physical Review A, 28*, 2591–2593.

Grassberger, P. & Procaccia, I. (1983b). Measuring the strangeness of strange attractors. *Physica D, 9*, 189–208.

Greene, B. R., Boylan, G. B., Reilly, R. B., de Chazal, P., & Connolly, S. (2007a). Combination of EEG and ECG for improved automatic neonatal seizure detection. *Clinical neurophysiology, 118*, 1348–1359.

Greene, B. R., de Chazal, P., Boylan, G., Reilly, R. B., O'Brien, C., & Connolly, S. (2006). Heart and respiration rate changes in the neonate during electroencephalographic seizure. *Medical and Biological Engineering and Computing, 44*, 27–34.

Greene, B. R., de Chazal, P., Boylan, G. B., Connolly, S., & Reilly, R. B. (2007b). Electrocardiogram based neonatal seizure detection. *IEEE Transactions on Biomedical Engineering, 54*(4), 673–682.

Hall, D. L. & Llinas, J. (2001). Multisensor data fusion. In D. L. Hall & J. Llinas (Eds.), *Handbook of multisensor data fusion*, CRC Press, chap. 1. 1–1–1–10.

Hall, D. L. & McMullen, S. A. H. (2004). *Mathematical techniques in multisensor data fusion*. Artech House, second ed.

Hallez, H., Vanrumste, B., Grech, R., Muscat, J., De Clercq, W., Vergult, A., D'Asseler, Y., Camilleri, K. P., Fabri, S. G., Van Huffel, S., & Lemahieu, I. (2007). Review on solving the forward problem in EEG source analysis. *Journal of neuroengineering and rehabilitation, 4*(46).

Hegger, R., Kantz, H., & Schreiber, T. (1999). Practical implementation of nonlinear time series methods: The TISEAN package. *Chaos: An Interdisciplinary Journal of Nonlinear Science*, *9*(2), 413–435.

Heinemann, U. & Eder, C. (1997). Control of neuronal excitability. In J. Engel Jr & T. A. Pedley (Eds.), *Epilepsy: A comprehensive textbook*, Lippincott-Raven Publishers, vol. One, chap. 22. 237–250.

Hernández, A. I., Carrault, G., Mora, F., Thoraval, L., Passariello, G., & Schleich, J. M. (1999). Multisensor fusion for atrial and ventricular activity detection in coronary care monitoring. *IEEE Transactions on Biomedical Engineering*, *46*(10), 1186–1190.

Hyvärinen, A. & Oja, E. (2000). Independent component analysis: Algorithms and applications. *Neural networks*, *13*, 411–430.

Iasemidis, L. D. & Sackellares, J. C. (1996). Chaos theory and epilepsy. *The Neuroscientist*, *2*, 118–126.

James, C. J. & Gibson, O. J. (2003). Temporally constrained ica: an application to artifact rejection in electromagnetic brain signal analysis. *IEEE Transactions on Biomedical Engineering*, *50*, 1108–1116.

Jasper, H. H., Pertuiset, B., & Flanigin, H. (1951). EEG and cortical electrograms in patients with temporal lobe seizures. *American Medical Association archives of neurology and psychiatry*, *65*, 272–290.

Kantz, H. & Schreiber, T. (2002). *Nonlinear time series analysis*. Cambridge University Press, second ed.

Kerem, D. H. & Geva, A. B. (2005). Forecasting epilepsy from the heart rate signal. *Medical and Biological Engineering and Computing*, *43*, 230–239.

Kirchner, A., Pauli, E., Hilz, M. J., Neundörfer, B., & Stefan, H. (2002). Sex differences and lateral asymmetry in heart rate modulation in patients with temporal lobe epilepsy. *Journal of Neurology Neurosurgery and Psychiatry*, *73*, 73–75.

Kounelakis, M. G., Zervakis, M. E., & Kotsiakis, X. N. (2005). Brain cancer classification using microarray technology. In A. Taktak (Ed.), *Perspectives in outcome prediction in cancer*, Elsevier Publishing Company.

Lehnertz, K. & Elger, C. (1995). Spatio-temporal dynamics of the primary epileptogenic area in temporal lobe epilepsy characterized by neuronal complexity loss. *Electroencephalography and clinical Neurophysiology*, *95*, 108–117.

Litt, B. & Echauz, J. (2002). Prediction of epileptic seizures. *The Lancet Neurology*, *1*, 22–30.

Locatelli, E. R., Varghese, J. P., Shuaib, A., & Potolicchio, S. J. (1999). Cardiac asystole and bradycardia as a manifestation of left temporal lobe complex partial seizure. *Annals of Internal Medicine*, *130*(7), 581–583.

Lopes da Silva, F. (1993). EEG analysis: Theory and practice. In E. Niedermeyer & F. Lopes da Silva (Eds.), *Electroencephalography: Basic principles, clinical applications, and related fields*, Williams & Wilkins, chap. 61. third ed., 1097–1123.

Lopes da Silva, F. H., Dijk, A., & Smits, H. (1975). Detection of nonstationarities in EEGs using the autoregressive model. an application to EEGs of epileptics. In G. Dolce & H. Künkel (Eds.), *CEAN - Computerized* EEG *analysis*, Fischer. 180–199.

Macdonald, R. L. (1997). Inhibitory synaptic transmission. In J. Engel Jr & T. A. Pedley (Eds.), *Epilepsy: A comprehensive textbook*, Lippincott-Raven Publishers, vol. One, chap. 24. 265–275.

Machin, D., Campbell, M. J., & Walters, S. J. (2007). *Medical statistics: A textbook for the health sciences*. Willey-Interscience, fourth ed.

Nabney, I. T. (2004). Efficient training of RBF networks for classification. *International journal of neural systems*, *14*(3), 201–208.

Nakamura, W., Anami, K., Mori, T., Saitoh, O., Cichocki, A., & Amari, S.-I. (2006). Removal of ballistocardiogram artifacts from simultaneously recorded EEG and fmri data using independent component analysis. *IEEE Transactions on Biomedical Engineering*, *53*(7), 1294–1308.

Niedermeyer, E. (1993). Abnormal EEG patterns: epileptic and paroxysmal. In E. Niedermeyer & F. Lopes da Silva (Eds.), *Electroencephalography: Basic principles, clinical applications, and related fields*, Williams & Wilkins, chap. 14. third ed., 217–240.

Nunez, P. L. & Srinivasan, R. (2006). *Electric fields of the brain*. Oxford University press, second ed.

Nuwer, M. R., Comi, G., Emmerson, R., Fuglsang-Frederiksen, A., Guerit, J. M., Hinrichs, H., Ideka, A., Luccas, F. J., & Rappelsburger, P. (1998). IFCN standards for digital recording of clinical EEG. *Electroencephalography and clinical neurophysiology*, *106*, 259–261.

Oppenheimer, S. M., Gelb, A., Girvin, J. P., & Hachinski, V. C. (1992). Cardiovascular effects of human insular cortex stimulation. *Neurology*, *42*, 1727–1732.

Perrone, M. P. (1994). General averaging results for convex optimization. In M. Mozer, P. Smolensky, D. Touretzky, J. Elman, & A. Weigend (Eds.), *Proceedings 1993 Connectionist Models Summer School*, Lawrence Erlbaum Associates. 364–371.

Perrone, M. P. & Cooper, L. N. (1994). When networks disagree: ensemble methods for hybrid neural networks. In R. J. Mammone (Ed.), *Artificial Neural Networks for Speech and Vision*, Chapman & Hall. 126–142.

Proctor, M. & Gale, K. (1997). Basal ganglia and brain stem anatomy and physiology. In J. Engel Jr & T. A. Pedley (Eds.), *Epilepsy: A comprehensive textbook*, Lippincott-Raven Publishers, vol. One, chap. 30. 353–368.

Quian Quiroga, R., Arnhold, J., Lehnertz, K., & Grassberger, P. (2000). Kullback-leibler and renormalized entropies: Applications to electroencephalograms of epilepsy patients. *Physical Review E*, *62*(6), 8330–8336.

Reeves, A. L. (1997). Autonomic activity in epilepsy: Diagnostic considerations and implications. *Journal of Epilepsy*, *10*, 111–116.

Reeves, A. L., Nollet, K. E., Klass, D. W., Sharbrough, F. W., & So, E. L. (1996). The ictal bradycardia syndrome. *Epilepsia*, *37*(10), 983–987.

Rezek, I. A. & Roberts, S. J. (1998). Stochastic complexity measures for physiological signal analysis. Tech. rep., Imperial College of Science, Technology and Medicine.

Rogova, G. L. & Stomper, P. C. (2002). Information fusion approach to microcalcification characterization. *Information fusion*, (3), 91–102.

Saab, M. E. & Gotman, J. (2005). A system to detect the onset of epileptic seizures in scalp EEG. *Clinical Neurophysiology*, *116*, 427–452.

Schwartzkroin, P. A. & McIntyre, D. C. (1997). Limbic anatomy and physiology. In J. Engel Jr & T. A. Pedley (Eds.), *Epilepsy: A comprehensive textbook*, Lippincott-Raven Publishers, vol. One, chap. 28. 323–340.

Shannon, C. E. (1948). A mathematical theory of communication. *The Bell System Technical Journal*, *29*, 379–423, 623–656.

Sharon, D., Hämäläinen, M. S., Tootell, R. B. H., Halgren, E., & Belliveau, J. W. (2007). The advantage of combining MEG and EEG: Comparison to fMRI in focally stimulated visual cortex. *NeuroImage*, *36*, 1225–1235.

Smith, D., Defalla, B. A., & Chadwick, D. W. (1998). The misdiagnosis of epilepsy and the management of refractory epilepsy in a specialist clinic. *QJ Med*, *92*, 15–23.

Solaiman, B., Debon, R., Pipelier, F., Cauvin, J.-M., & Roux, C. (1999). Information fusion: Application to data and model fusion for ultrasound image segmentation. *IEEE Transactions on Biomedical Engineering*, *46*(10), 1171–1175.

Stam, C. J. (2005). Nonlinear dynamical analysis of EEG and MEG: Review of an emerging field. *Clinical neurophysiology*, *116*, 2266–2301.

Steinberg, A. N. & Bowman, C. L. (2001). Revisions of the JDL data fusion model. In D. L. Hall & J. Llinas (Eds.), *Handbook of multisensor data fusion*, CRC Press, chap. 2. 2.

Takens, F. (1981). Detecting strange attractors in turbulence. In D. A. Rand & L. S. Young (Eds.), *Dynamical systems and turbulence*. vol. 898 of *Lecture Notes in Mathematics*, 366.

Taleb-Ahmed, A. & Gautier, L. (2002). On information fusion to improve segmentation of MRI sequences. *Information fusion*, (3), 103–117.

Vergult, A., De Clercq, W., Palmini, A., Vanrumste, B., Dupont, P., Van Huffel, S., & Van Paesschen, W. (2007). Improving the interpretation of ictal scalp EEG: BSS-CCA algorithm for muscle artifact removal. *Epilepsia*, *48*(5), 950–958.

Wasterlain, C. G. & Mazarati, A. D. (1997). Neuromodulators and second messengers. In J. Engel Jr & T. A. Pedley (Eds.), *Epilepsy: A comprehensive textbook*, Lippincott-Raven Publishers, vol. One, chap. 25. 277–289.

Whitney, H. (1936). Differentiable manifolds. *The Annals of Mathematics*, *37*(3), 645–680.

Zhao, P., Van-Eevelt, P., Goh, C., Hudson, N., Wimalaratna, S., & Ifeachor, E. C. (2007). Characterization of EEGs in alzheimer's disease using information theoretic methods. In *Proceedings of the 29th* IEEE EMBS *annual international conference*.

A Dataset

A.1 Dataset of Medial Temporal Lobe Epilepsy patients for Biopattern

Collaborators from the BIOMED[1] team and from the department of Clinical and Experimental Neurology[2], both at Katholieke Universiteit Leuven (KUL)[3] have given access to Biopattern partners to a dataset of long-term EEG recordings from patients suffering from Mesial Temporal Lobe Epilepsy (De Clercq *et al.*, 2006; Vergult *et al.*, 2007).

The video-EEGs were recorded on 21-channel OSG EEG recorders (Rumst, Belgium). Electrodes were placed according to the International 10-20 System (Nuwer *et al.*, 1998) with additional sphenoidal electrodes. Sampling frequency was 250Hz. An average reference montage was used: the raw EEG was referenced with respect to G19, the Goldman reference, which is the average of all electrodes of the International 10-20 System except for Fp1, Fp2, A1 and A2 (channels that capture artifacts). The EEG was digitally filtered by a band pass filter (0.3-35Hz). A notch filter was applied to suppress the 50Hz power-line interference.

The ECG for each patient was simultaneously acquired and is available on channel 22

[1] http://homes.esat.kuleuven.be/~biomed
[2] http://www.neurology-kuleuven.be
[3] http://www.kuleuven.be

of each recording.

Figure A.1 is a plot of a long-term EEG recording (twenty one EEG channels) and simultaneously recorded ECG (one ECG channel) from the dataset of Medial Temporal Lobe Epilepsy patients for Biopattern.

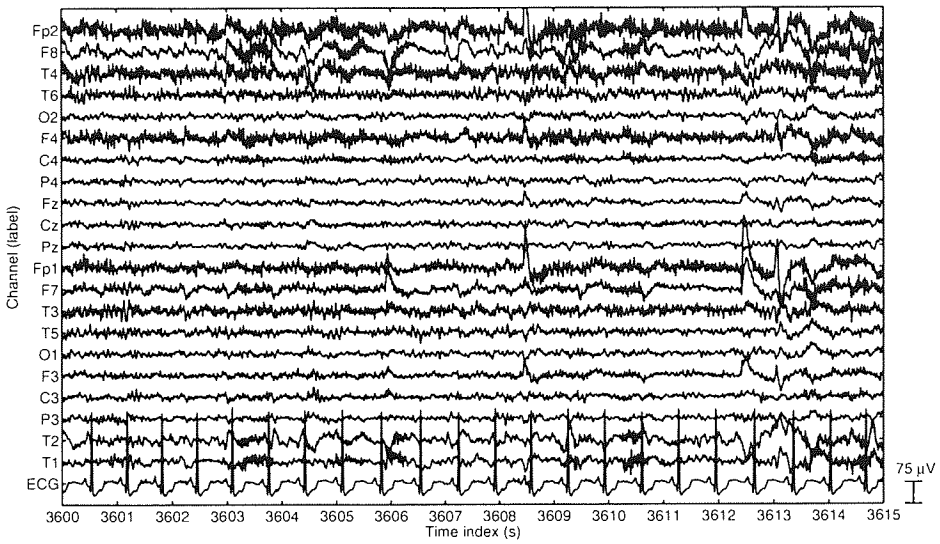

Figure A.1: Long-term EEG recording and simultaneously recorded ECG from the dataset of Medial Temporal Lobe Epilepsy patients for Biopattern. Note that the ECG has been scaled by a factor of 0.1 for plotting purposes.

B Performance evaluation

B.1 Sensitivity and specificity

The concepts of sensitivity and specificity are defined as:

$$\text{sensitivity} = \frac{\text{number of True Positives}}{\text{number of True Positives} + \text{number of False Negatives}} \quad \text{(B.1)}$$

$$\text{specificity} = \frac{\text{number of True Negatives}}{\text{number of True Negatives} + \text{number of False Positives}}, \quad \text{(B.2)}$$

where a false-negative or "Type II error" is the error of failing to reject an hypothesis (such as "A patient is free of a disease") when it is actually not true (i.e. unhealthy people wrongly identified as healthy); a false-positive or "Type I error" is the error of rejecting a null hypothesis when it is actually true (i.e. healthy people wrongly identified as unhealthy). In medicine false-negatives and false-positives have dramatic consequences:

- in the case of medical screening, which consists in testing, with non-invasive tests, large populations of whom none manifest any clinical indication of disease, negatives are not investigated further whereas positives are investigated by more precise tests to confirm if a positive patient is a true-positive. The false-positives are likely to be discovered at the stage of the medical testing
- in the case of medical testing, which consist in testing population who manifest clinical indication of disease, false-positives may lead to patients undertaking un-

necessary treatment with consequences depending on the invasiveness of the treatment; false-negatives may lead clinicians to thinking that a patient is disease-free whereas the patient is not with consequences depending on a combination of factors such as the invasiveness of the disease or the effectiveness of the delayed treatment on the disease

A sensitivity of 100% means that the test recognises all unhealthy people as such; a specificity of 100% means that the test recognises all healthy people as such. In medical screening and testing a tradeoff between sensitivity and specificity, usually in favour of the sensitivity, has to be achieved. The tradeoff to be conceded between specificity and sensitivity is evaluated with regards to the consequences of a misdiagnosis: is it preferable to recognise all unhealthy people as such (i.e. usually the consequences of not diagnosing the disease are far more dramatic on the patient health than administrating unnecessary treatment) or is it preferable to recognise all healthy patients (i.e. the administration of the unnecessary treatment to a healthy patient has far more dramatic consequences on the patient health than not administrating the treatment to an unhealthy patient)? In automated seizure detection applications the former solution is privileged as false-positives (i.e. detecting an epileptic event when none actually occurs) are easily discarded by visual inspection by trained clinicians whereas false-negatives prevent access to crucial information such as epileptic foci, type of epilepsy and frequency of seizures. However in recent years much work has been done in order to achieve a high sensitivity while achieving a high specificity too (in order to reduce the number of false-positives that can dramatically slow down the analysis of long-term recordings). The same objective has been pursued in the Thesis: the false-positive free automated detection of epileptic events from long-term recordings. For more information on the consequences of the misdiagnosis of epilepsy, refer to (Smith *et al.*, 1998).

In this Thesis the detection accuracy of the methods investigated was evaluated on a sample basis (e.g. a sample algorithm detection matching a sample expert detection is a true-positive; a sample algorithm detection matching a sample expert non-detection is a false-positive) as opposed to on an event basis for which an algorithm that overlaps any part of an event expert detection is a match; otherwise the algorithm detection is a false-positive, accounted only once per event expert detection (Gotman, 1982).

The detection accuracy of the method was evaluated by plotting receiver operating characteristic (ROC) curves (Machin *et al.*, 2007), which is a plot of the sensitivity versus (1 - specificity), for the classification of samples in epileptic or non-epileptic classes as a discriminant threshold on the probability of epileptic seizure given the observations, features, probabilities or decisions was varied. The best possible classification would lead to a sensitivity of 100% and to a specificity of 100% which corresponds to the upper left corner of the ROC space of coordinates (0,1): the point of perfect classification. The ROC curve of an effective classification method would rapidly tend towards the point of perfect classification. A way to compare the classification accuracy of different methods is to quantify how rapidly they tend towards the point of perfect classification by comparing their areas under the ROC curve (AUC) as the bigger the AUC, the closer the ROC to the point of perfect classification.